



**HAL**  
open science

# Environmental electron microscopy and multiscale tomography

Lucian Roiban

► **To cite this version:**

Lucian Roiban. Environmental electron microscopy and multiscale tomography. Physics [physics]. Insa-Lyon, Université Lyon1, 2021. tel-03543777

**HAL Id: tel-03543777**

**<https://hal.science/tel-03543777v1>**

Submitted on 26 Jan 2022

**HAL** is a multi-disciplinary open access archive for the deposit and dissemination of scientific research documents, whether they are published or not. The documents may come from teaching and research institutions in France or abroad, or from public or private research centers.

L'archive ouverte pluridisciplinaire **HAL**, est destinée au dépôt et à la diffusion de documents scientifiques de niveau recherche, publiés ou non, émanant des établissements d'enseignement et de recherche français ou étrangers, des laboratoires publics ou privés.

## HABILITATION A DIRIGER DES RECHERCHES

présentée devant / defended in front of

l'Institut National des Sciences Appliquées de Lyon

et l'Université Claude Bernard LYON I

### Microscopie électronique en mode environnemental et tomographie multi-échelle

### Environmental electron microscopy and multiscale tomography

SPECIALITE : Microscopie électronique, Science de matériaux

EXPERTISE: Electron microscopy, Materials science

par /by

Roiban Lucian

Devant être soutenue le/ date : 08/11/2021

devant la Commission d'examen / in front of the jury

Bals Sara	Professor, University of Antwerp	Rapporteur/Reviewer
Brioude Arnaud	Professor, Université Claude Bernard Lyon 1	Examineur/Examiner
Chevalier Jérôme	Professor, INSA-Lyon	Examineur/Examiner
Ersen Ovidiu	Professor, Université de Strasbourg	Examineur/Examiner
Marco Sergio	Research Director, Institut Curie/ Sanofi	Rapporteur/Reviewer
Willinger Marc	Professor, ETH Zurich	Rapporteur/Reviewer

MATÉRIAUX : INGÉNIERIE ET SCIENCE (MateIS)



To my family.



## i. Curriculum Vitae -Lucian Roiban

MateIS Laboratory  
Blaise Pascal Building  
Institut National des Sciences Appliquées de  
Lyon  
7 avenue Jean Capelle  
69621 VILLEURBANNE Cedex  
Phone : 0033 472436131  
e-mail : [lucian.roiban@INSA-Lyon.fr](mailto:lucian.roiban@INSA-Lyon.fr)

Nationality: Franco-Romanian  
Spoken languages: English (C2), French  
(C2-C1), Romanian (native)  
[ORCID](#), [Google Scholar](#), [Scopus](#), [Hal](#)

### Education

2007-2010 Ph.D. in Physics of Materials Science, University of Strasbourg, France

“*Analytical tomography: development of 3D chemical mapping at nanometer scale applied to heterogeneous catalysts*” <http://scd-theses.u-strasbg.fr/1988/>

2005-2007 Master in Physics, *Solid states physics*, “**Babeş – Bolyai**” University of Cluj-Napoca, Romania.

2001–2005 Bachelor in Physics, Faculty of Physics, “**Babeş – Bolyai**” University of Cluj-Napoca, Romania

### Positions held

2012 – onwards Associate Professor/Maître de conférences (permanent position) at Matériaux Ingénierie et Science (MateIS), FIMI department, INSA-Lyon, Lyon University, France.

2011 – 2012 Postdoctoral position: *Fundamental studies on the synthesis of carbon supported noble metal catalysts using electron tomography*. Inorganic Chemistry and Catalysis, Utrecht University, the Netherlands

2010 – 2011 Postdoctoral position: *Synthesis and characterization by electron tomography of hybrid materials: semiconductor, polymer, inorganic nanoparticles, used in photovoltaic applications*. IPCMS, University of Strasbourg, France

### Teaching duty and responsibilities

2016 – onwards In charge of the pedagogical team for optics in the 1<sup>st</sup> year of bachelor. In the curriculum, there are 4 different practicals, each one being followed by around 875 students/year.

2017– onwards In charge of the training of the new teachers for the practical on diffraction.

2014 – 2017 On charge of the practical on diffraction for the second year of bachelor. This includes experiment preparation and teachers training.

### Commissions of trust

2012 – onwards Member of the Microscope Team of Lyon Microscopy Center (CLYM), INSA-Lyon, France.

- 2018- onwards            Elected member of the scientific board of INSA-Lyon, France
- 2016 – 2020            Elected member of the advisory board of the MATEIS laboratory, INSA-Lyon, France
- 2019                    Member of a PhD jury, INSA, Lyon University, France
- Bruno Chal, [Vieillissement thermohygrique de silices nanostructurées, vers une compréhension des mécanismes](#), 08/11/2019.
- 2018                    Member of a PhD jury, Université Claude Bernard Lyon1, France
- Nelly Couzon, [Synthèse et propriétés photoélectrochimiques denanoparticules d'argent intégrées dans des films d'oxydes mésoporeux](#), 25/09/2018.
- 2017                    Examiner of a PhD jury, INSA, Lyon University, France
- Siddardha Koneti, [In situ and 3D Environmental Transmission Electron Microscopy of Pd-Al<sub>2</sub>O<sub>3</sub>Nano catalysts: fast tomography with applications to other catalytic systems in operando conditions and to electron beam sensitive nanomaterials](#)
- 2017                    Member of 2 PhD jurys, INSA, Lyon University, France
- Juan Xiao, [Development of electron tomography on liquid suspensions using Environmental Scanning Electron Microscopy](#), 13/06/2017.
- Daniel Paul Odum Thomas, [Réalisation de transistors à un électron par encapsulation d'îlots nanométriques de platine dans une matrice diélectrique en utilisant un procédé ALD](#), 15/12/2017
- 2015                    Examiner, Ecole Polytechnique, Paris University, France
- Leandro Nicolás Sacco, [Synthesis of carbon nanotubes within porous anodic alumina templates for electronic applications](#), 15 /12/ 2015

### *Research activity*

My research is centered on the development of electron tomography techniques and their application to the characterization of nanomaterials in environmental conditions at multi scale. I have published 49 articles in peer-reviewed journals (for 10 of them I am the first author), and three book chapters. I delivered 3 invited lectures. My *h* index according to [Scopus is 15](#). I partially supervised 2 PhD students during my post-doc fellowship at University of Strasbourg and Utrecht University respectively. At INSA-Lyon, I have supervised the research work of 7 Master students and 5 PhD students. I am currently, co-supervising 3 PhD students.

**Award of the Strasbourg University** presented by “Amis des Universités de l’Académie de Strasbourg” in 2011 for my PhD work.

**Award of the International Federation of Societies for Microscopy (IFSM)**, Rio de Janeiro, Brazil 2010 for research during my PhD. This consisted of a scholarship to attend the “IFSM Pre-Congress Advanced Microscopy School” where I presented: “Analytical electron tomography: a powerful tool for determining the chemical composition of 3D nanostructures at the nanoscale.”

## ii. Teaching activities

Since the end of my master, I have taught general physics. I started as a high school teacher in Cluj-Napoca, during a semester. Then, during my PhD preparation I had the opportunity to be teaching assistant at Strasbourg University at Physics and Natural Science Faculties. Since 2012, I have been an Associate Professor at INSA-Lyon. In all those positions I have had the opportunity to gain pedagogical experience by teaching optics, measurements and electricity for bachelor students, and electron microscopy and electron tomography for PhD students and researchers in the framework of [CNRS training schools](#).

In my current position I have mainly taught practical and tutorials in the Classics and Scan programs (in the Scan program the courses are taught in English). While teaching, I like to be close to students. I have the ability to develop discussions during which they are challenged to ask questions, to doubt, to check, to re-do, to comprehend and to impregnate themselves with the information, not to learn it by heart. By doing so, the teacher is not anymore in charge, he exposes himself to an unexpected and uncontrolled exchange with the students. However, I strongly believe that it gives students the opportunity to express themselves, to enhance the ability to communicate their ideas, their feelings and give them the ability to assimilate faster and correlate new information from different topics but, more important, to be independent and to be able to work together in teams. I believe that encouraging the students to exchange and to communicate and most important to reformulate, helps the students to develop themselves and to grow. The students who have not very well understood will understand better and those who have already managed the information do improve themselves. They improve not only scientifically but also humanly. The students that are actively participating do express themselves in a better oral way as well as in a written way, and they have good scholar results.

From the administrative point of view, in the Classic teaching program, I am in charge of the geometrical optics practical consisting in 4 practical sessions for the first year. I gave some lectures as an introduction course in optics for the first-year students in the SCAN program, also I gave some lectures in the framework of the [CNRS training schools](#).



### iii. Foreword

The breaking point for a scientific career was made during my Erasmus mobility at the University Louis Pasteur in Strasbourg, that became afterwards University of Strasbourg. After that, I had a short internship at French Institute of Petroleum and New Energies (IFPEN) that led to my PhD position at University of Strasbourg. Since then my research activity has mainly been dedicated to the development of imaging techniques used to the 3D analysis of nanomaterials, more precisely, to the development of different imaging modes that are available in electron tomography. In the course of my young career I can mainly identify three levels or steps of my scientific experience.

The first level concerns the development of Analytic Electron Tomography (AET) that was made during my thesis in cooperation with my colleagues from IPCMS and IFPEN. Electron tomography consists in the volume reconstruction of the sample using a series of tilted projections of the object. A very short and general introduction of the principles of electron tomography is given in section (1). For AET, the projections are formed using the Energy Filtered Imaging (EFTEM) mode. The electrons that have interacted with a unique chemical element are filtered and used to form projections named filtered images. The chemical maps can be computed using three elemental filtered images that are recorded: two filtered images before the ionization edge of the chemical element are used to estimate the background. A third filtered image is recorded after the ionization edge of the chemical element and the chemical map is the difference between the third filtered image and the estimated background. AET was used to quantify the chemical distribution of industrial supports of catalysts such as silica-alumina<sup>1,2</sup> and titania-alumina<sup>3</sup>. Later on, it was employed in the study of Mn oxidation states distribution in a channel-like mesoporous zirconium oxide<sup>4</sup>. It is worth noticing that the developments made during my PhD signed the birth of “*Analytical tomography*” at nanometer scale<sup>5</sup>. For the sake of clarity, these achievements are not exposed in this document.

The second level of research activity, that is essentially described in this document, was made in cooperation with my colleagues from MateIS but also from other research institutions. The research was dedicated to the development of so-called “Fast Electron Tomography” in bright field mode. Here “fast” should not be taken *ad litteram*, as it refers only to fast image recording and not to the whole process. The development of fast electron tomography opened the way towards 3D analysis of beam-sensitive materials and to materials that are submitted to environmental conditions, *i.e.* under gas, in liquid or at high temperature. To successfully analyze a beam-sensitive sample in 3D it is important that the sample does not suffer from

morphological changes under the electron beam. Similarly, in *operando* conditions the electron beam can have an influence on the dynamics of the studied reactions or it can induce phenomena that do not occur in normal conditions. Therefore, it is important to record tilted images really fast in order to limit at minimum the influence of the electron beam on the 3D investigation. The different developments made in the context of different cooperations are exposed in this document.

The third level consists in the development and the application of multiscale electron tomography in environmental conditions. More precisely, in close cooperation with colleagues from the MateIS lab, we are developing STEM electron tomography of materials suspended in liquid (water) by using an Environmental Scanning Electron Microscope (ESEM). The goal of the project is to perform multiscale complementary analysis (ETEM – ESEM) of materials suspended in liquid. This is possible because around 2° C and 7 mbar of water vapor, the liquid-vapor equilibrium can be ensured and the sample will be maintained in liquid without encapsulation in an environmental closed cell. This project will be expose later in the document.

As a pictorial description of my scientific evolution, Figure 1 shows an infographic representation of the different projects dedicated to the development of imaging modes in electron tomography. In this image I illustrate the synergy between the projects and the tendency towards multi-scale 3D analysis in *operando* conditions.

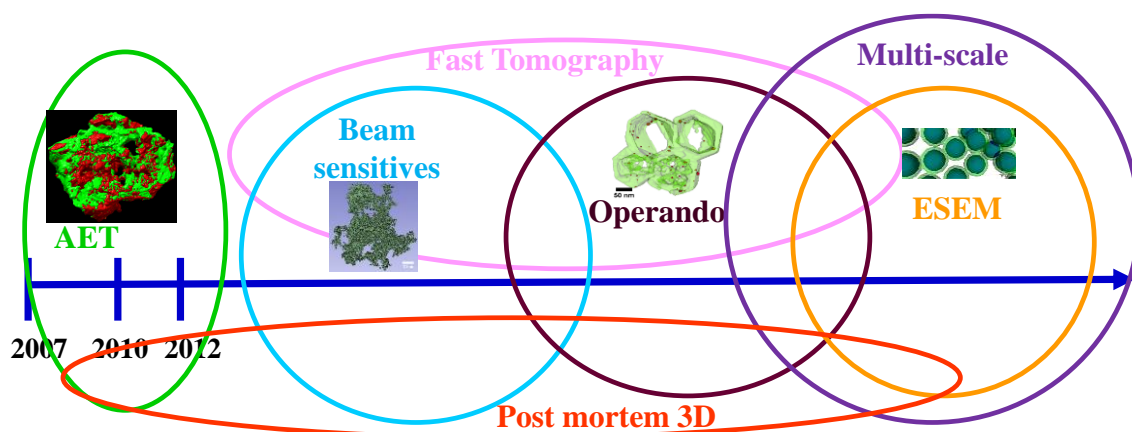


Figure 1: Schematic representation of the research projects dedicated to the development of 3D imaging techniques in which I have been involved. The time line as well as the areas marked for the different projects are intuitive. The goal of the representation is to mark the synergy between projects. However, it can be seen that 3D techniques such as FIB or X-rays are, for now, missing from my activity.

# Electron tomography of evolving materials

## Outline

General introduction.....	12
1 Seeing objects in 3D at the nanoscale .....	13
1.1 Electron tomography, a brief introduction .....	13
1.2 Electron tomography applied in study of materials.....	14
1.2.1 Electron microscopy used in the development of electronic devices.....	15
1.2.2 Electroactive area from porous oxide films loaded with Ag nanoparticles .....	17
2 Beam sensitive materials in 3D - the need to record images faster.....	22
2.1 Technical methods to record low electron dose images .....	22
2.1.1 Low dose in “conventional” BF electron tomography.....	22
2.1.2 Fast image recording for electron tomography .....	23
2.1.3 SIRT-FISTA-TV reconstruction algorithm applied to fast electron tomography	29
2.2 Electron tomography applied to the study of beam-sensitive materials.....	31
2.2.1 Nanoporous silica in 3D at low electron dose.....	32
2.2.2 Aging process of nano silica for building insulation.....	33
2.2.3 LDH dispersed in latex nanocomposite.....	35
3 <i>Operando</i> electron tomography .....	36
3.1 Materials in controlled environment in 3D.....	36
3.1.1 Soot combustion supported by YSZ in 3D <i>operando</i> .....	37
3.1.2 3D calcination of Ag nanoparticles enclosed in hollow silicalite – 1 .....	41
3.1.3 3D sintering resistant Pd @SiO <sub>2</sub> core-shell nanoparticles .....	44
3.2 <i>Operando</i> electron microscopy combined with <i>post-mortem</i> electron tomography .	46
3.2.1 2D <i>in situ</i> growth of metal nanoparticles on the surface of a perovskite .....	47
3.2.2 Genesis of Pd nanoparticles supported by $\delta$ and $\alpha$ - Al <sub>2</sub> O <sub>3</sub> .....	50
3.2.3 Migration and growth of Ag nanoparticles supported by ZSM-5.....	54

4	Multiscale electron tomography .....	58
4.1	Environmental Scanning Electron Tomography in an ESEM.....	58
4.1.1	3D analysis of grafted CNT dispersion within polyurethane.....	59
4.1.2	Latex particles suspended in water.....	62
4.1.3	Towards 3D analysis of whole biological cells in native state?.....	65
5	Perspectives .....	67
5.1	Multi scale tomography .....	67
5.1.1	X-ray tomography applications in the study of some pathologies of the internal ear	67
5.1.2	E-SEM applied to the study of the interactions between a cell and a biomaterial	69
5.2	Multi-scale environmental electron microscopy .....	71
5.2.1	Ni metal nanoparticle growth.....	72
5.2.2	Adjuvants in liquid phase .....	72
5.3	TEM applied to the study of materials under both HV and <i>operando</i> conditions.....	73
5.3.1	Environmental HRTEM of bimetallic particles AuAg and AgAl.....	73
5.3.2	Environmental electron microscopy of functional materials .....	73
5.3.3	Liquid phase in ETEM .....	74
5.4	Pushing the limits of electron microscopy .....	75
5.4.1	AI in electron microscopy? .....	75
5.4.2	Further in time: faster and faster image recording for ET.....	76
5.4.3	Even further in time: Adaptive environmental corrector for environmental electron microscopy .....	76
6	Ending word .....	78
	Abbreviations .....	79
	Bibliography.....	81

## General introduction

In this document I will expose some of my research activities that I have had the honor to lead or to be involved as a partner. The document is divided in two main parts. The first part is dedicated to the development of fast electron tomography and its application in high vacuum studies and the second part to the development and its application in *operando* studies. Therefore, the document starts by very briefly reminding the principles of electron tomography, the microscopy technique that is the core of my scientific activity (section 1).

The first section of the first part (section 2) is dedicated to low-dose electron tomography. The need for the development of fast image recording for electron tomography in bright field mode is explained. The developments made are shown, with some technical details and a discussion on some experimental conditions that could help to its implementation. Then, examples of experimental studies are given. First, beam-sensitive materials are studied under high vacuum. Here are showed the studies of the aging of nano-silica for building insulation and the study of the dispersion of LDH in latex.

The presentation of the *operando* electron tomography studies starts in the second part of the document ( section 3). Soot combustion supported by YSZ, calcination of Ag nanoparticles enclosed in hollow silica, and the sintering resistance of Pd nanoparticles enclosed in SiO<sub>2</sub> are studied. All those experiments were performed using fast electron tomography in *operando* conditions. In my research, I always like to combine *operando* studies with *post-mortem* ones. Such combination is presented for the study of the growth of metallic particles at the surface of perovskite, the genesis of Pd particles supported by alumina and the deactivation process of Ag nanoparticles supported by zeolite.

I genuinely believe that multi-scale investigation in electron microscopy can provide a full understanding of a material in given conditions. During several years, I have involved myself in the development of electron tomography in transmission in an environmental scanning electron microscope. In the section 4 some of the developments made are showed, as well as some of the applications.

The document continues with the presentation of perspectives proposed for the near future, and ideas on which I would like to reflect at a longer period of time. In the near future, I expose my research interests in the multiscale approach, from atomic to micrometer resolution in environmental mode both in liquid phase and under gas pressure.

# 1 Seeing objects in 3D at the nanoscale

In materials science, the bi-dimensional characterization of samples having complex morphologies or chemistries at nanoscale cannot provide reliable answers to questions such as: “what is the real position of a supported active phase?” or “how is the porous network of a support?” or “do those nanoparticles adopt a core-shell structure?” etc. To answer such questions, the use of electron tomography is required.

## 1.1 Electron tomography, a brief introduction

Electron tomography (ET) consists in the volume reconstruction of a three-dimensional (3D) object using a tilted projections series. Even if the word “tomography”, born in antic Greece means “writing or showing or describing” “slices”, the mathematical description was first performed by Radon in 1917<sup>6-8</sup>. The Radon theory says that it is possible to reconstruct the volume of an object by knowing all its possible angular projections. In 1959, Bracewell<sup>9</sup> demonstrated that a volume can be reconstructed using a limited numbers of projections. He reconstructed 2D areas called “strip integration” using radio waves of “celestial sources”. The best-known application of the Radon theory appeared in the development of computer assisted tomography using X-rays projections that made possible a density reconstruction of a volume. That development was awarded the Nobel Prize in Physiology or Medicine in 1979 for Cormack and Hounsfield.

In electron microscopy, the first developments were performed in the field of biology. ET was used in the pioneering work of de Rosier and Klung<sup>10</sup>, that set the basis of transmission electron tomography for “all kinds of objects”. Even if ET had a wide use in biology<sup>11</sup>, in materials science its use started only 20 years later when “the location of metal particles in a metal-zeolite crystal”<sup>12</sup> was established. Since that time, ET has spread wide and fast, and has been developed and improved by many research groups. At the beginning, it was used only as a density map obtained by using the bright-field mode (BF) of a transmission electron microscope (TEM), but rapidly other imaging modes were employed and chemical distributions could be obtained using High Angle Annular Dark Field mode in Scanning Transmission Electron Microscopy (STEM-HAADF), Energy Filtered Transmission Electron Microscopy (EFTEM) and X-rays<sup>13-17</sup>. Its spatial resolution has continuously been improved, reaching the atomic resolution<sup>18,19</sup> in 3D, only a few years after it was considered as “a dream”<sup>20</sup>.

ET consists in the reconstruction of a volume from a series of projected images acquired at various tilt angles of the sample, named tilt images series. Its principle, with the different steps, is schematically represented in Figure 2. The electron microscope must be able to tilt the sample with the largest possible range, ideally  $\pm 90^\circ$ . Such a tilting range is achievable using a needle-like sample prepared, for instance, using Focused Ion Beam (FIB)<sup>21,22</sup>. Today, dedicated software can tilt and track the samples during the tilting process and automatically record an image at every tilt angle. Once recorded, the tilted images series are aligned in a unique system of coordinates, and the volume can be reconstructed. Afterwards, the volume can be visualized and segmented. Accordingly, a 3D model of the object can be obtained and, for a better visualization, different colors can be assigned to each component. Once the segmentation is performed and the 3D model computed, it is possible to perform a quantitative analysis of 3D parameters that cannot be achieved by any other techniques at the nanometer resolution. Such parameters can be, among others, a particle size distribution<sup>23</sup>, a pore connectivity<sup>24</sup> or a chemical distribution within the volume or at the surface of a catalyst<sup>2</sup>.

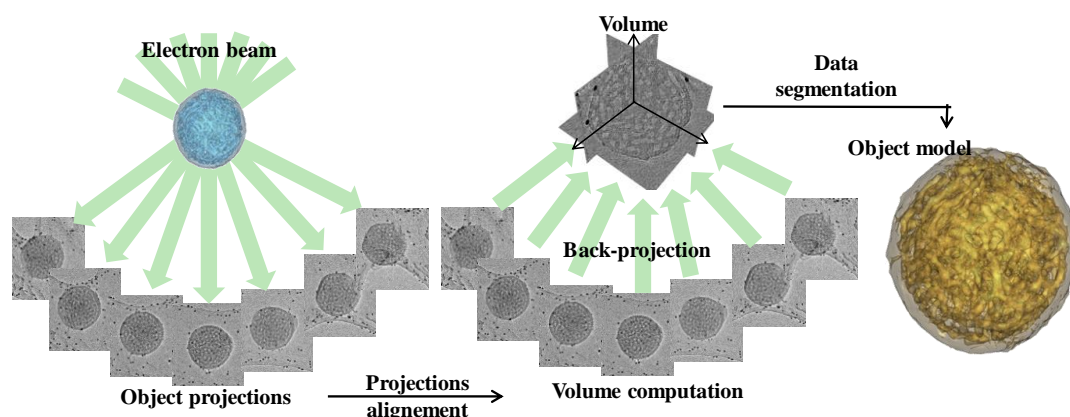


Figure 2: Scheme representing the principle of transmission electron tomography. 2D images, called projections, are first acquired at different angles. Then the projections are aligned and using back projections algorithms the volume is reconstructed. The segmentation process consists in assigning the gray levels to a component. The last step is the modeling of the object by attributing fake colors and quantifying its morphological and chemical parameters. Image modified from <sup>25</sup>, where ET is applied on a  $\text{SiO}_2\text{-ZrO}_2$  object.

## 1.2 Electron tomography applied in study of materials

As examples of applications, before showing studies of materials in *operando* conditions or materials that are beam-sensitive, I will present two electron tomography studies for which the images recording was performed in the so-called “conventional way”. In these cases, the object is tilted, re-positioned, focused and the image is recorded. The studies were performed in the

framework of cooperations, as PhD co-supervisor, on which I brought my expertise in electron microscopy.

The experiments were performed by employing the ETEM-TITAN (80-300 keV) of the CLYM. The tilt series were recorded using the TIA tomography plugin, and the recording time was set between 45' to 90' depending on the dwell time and the stability of the sample. The tilt series were aligned employing IMOD<sup>26</sup>, the volumes reconstructed using Tomoj<sup>27</sup> and the modeling was performed using Imagej<sup>28</sup> and 3D Slicer<sup>29</sup>.

More examples of electron tomography performed in vacuum in both BF-TEM and HAADF-STEM modes can be provided, if necessary, as an Appendix.

### 1.2.1 Electron microscopy used in the development of electronic devices

In cooperation with Dr. Etienne Puyoo from INL, INSA-Lyon, we co-supervised the thesis of Dr. Daniel Thomas directed by Dr. Martine Le Berre and Dr. Liviu Militaru. The thesis was supported by the French Ministry of Research and Higher Education, by INSA-Lyon through the BQR program, and by the Labex iMUST of Lyon University. It was dedicated to the development of Single Electron Transistors (SET) using Pt nanoparticles deposited by Atomic Layer Deposition (ALD). I will not describe in detail the fabrication process, the electrical characteristics and tests of the device, that are available in [Daniel's thesis](#)<sup>i</sup>, I will focus only on the contribution of electron microscopy. In this project, I worked in close cooperation with Dr. Annie Malchère. We used multiscale analysis from SEM to HR-TEM and STEM.

The goal was to follow and to characterize the genesis of a SET using the electron microscopy tools. A SET is a nano-device firstly developed at MIT in 1989 that is formed by a multi-gate structure enabling the control of a 1D electron gas flow. At low temperature, such type of device produces reproducible oscillations due to a Coulomb blockade. To build the device, a metal-insulator-metal planar structure was made by alternating amorphous Al<sub>2</sub>O<sub>3</sub> as insulator and Pt layers that form nanoparticles under heat. The size of the nanoparticles is controlled by the deposition cycles that are made. On the obtained planar structure, a first Pd electrode is deposited by lithography and evaporation at 0°. Then the structure is tilted such that the first

---

<sup>i</sup> Daniel Paul Odum Thomas, Réalisation de transistors à un électron par encapsulation d'îlots nanométriques de platine dans une matrice diélectrique en utilisant un procédé ALD, INSA Lyon, Ecole Doctorale N° ED160 Électronique, Électrotechnique, Automatique, 15/12/2017.



electrode makes a shadow. Then the second electrode is evaporated. By doing so, the thickness of the gap depends on the thickness of the first electrode and the value of the tilted angle.

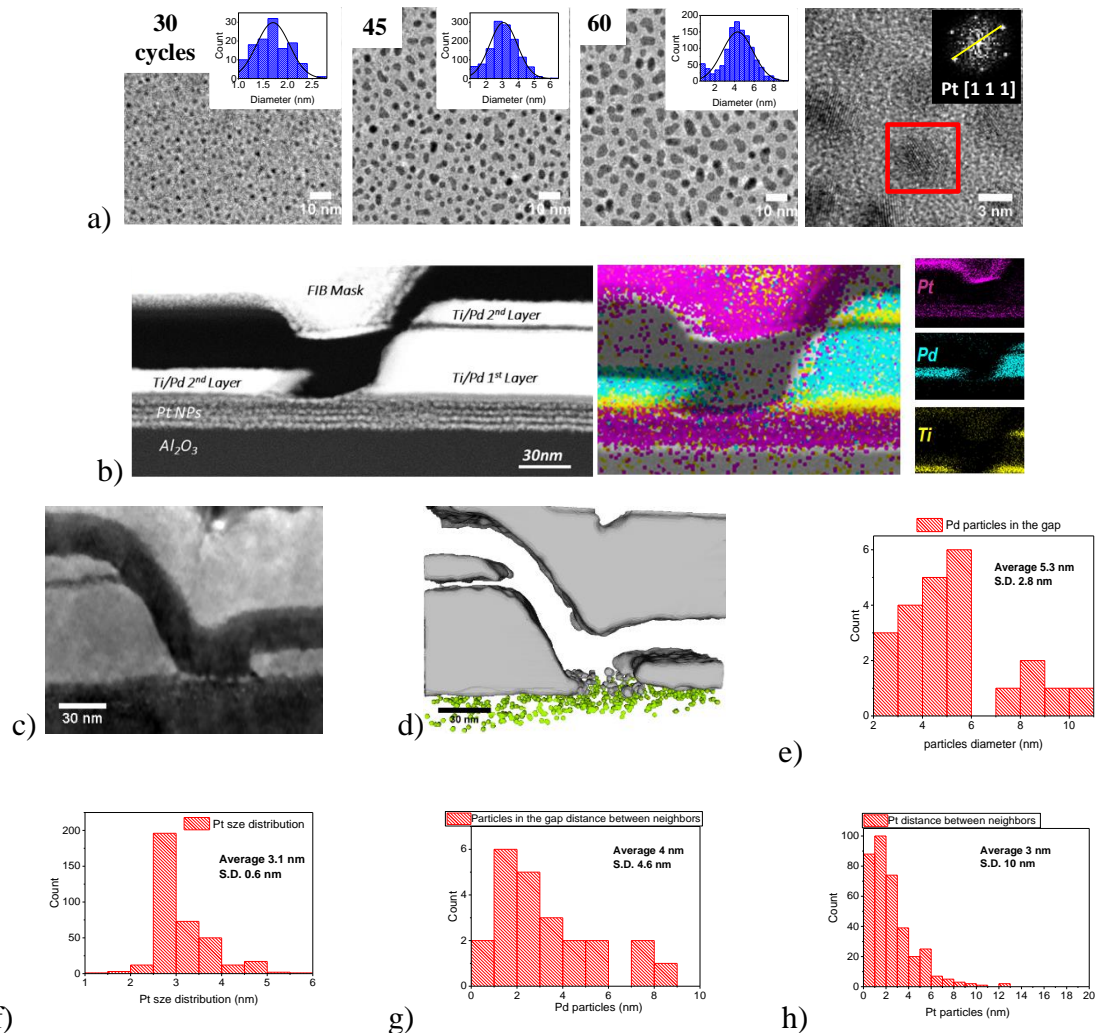


Figure 3: a) Pt particles deposited by ALD on an amorphous  $\text{Al}_2\text{O}_3$  substrate, the size and density depend on the number of deposition cycles. After 30 cycles the average size of Pt nanoparticles is 1.7 nm, after 45 cycles is 3.1 nm and after 60 cycles is 4.3 nm. b) STEM image and its EDX map of a SET prepared by FIB showing the support of  $\text{Al}_2\text{O}_3$ , the Pt particles layer the two Pd electrodes and the W deposited for the FIB preparation. The SET was obtained by tilting the support at  $60^\circ$  during the lithography of the second electrode c) Oriented slice through the volume of a sample prepared at  $45^\circ$  tilt. It can be seen that some particles are in the gap that is slightly smaller than the gap obtained at a tilt of  $60^\circ$ . The gray level and the EDX analysis shown that particles in the gap are formed by Pd. d) The 3D model of the sample shown in c), in green are the Pt particles, in gray are the Pd electrodes and the Pd particles inside the gap. e) and f) Pd particles inside the gap and Pt particles size distribution. g) and h) Distances between the first order neighbors of the particles in the gap and the Pt particles. Image modified from <sup>30</sup>.

The BF-TEM mode was used to assess the Pt particle size and distribution on the amorphous  $\text{Al}_2\text{O}_3$  layer. For that purpose,  $\text{SiO}_2$  electron microscopy grids were used as a support on which

the Al<sub>2</sub>O<sub>3</sub> layer and the Pt particles were deposited (Figure 3 a)) simultaneously with those prepared on the silicon wafer. Once the Pt particles size was determined, the entire device was made using different thicknesses and tilt angles of the first electrode in order to control the thickness of the gap between the electrodes. Because the “vertical” thickness of a SET is too large to be electron-transparent, the devices were made on a Si wafer on which an Al<sub>2</sub>O<sub>3</sub> amorphous layer was deposited. Then, by using FIB, thin lamellas were prepared for TEM analysis and STEM tomography. Some of the results are shown in Figure 3 b). The combination with SEM imaging, that is not shown here, has proven that the gap of the SET device can indeed be controlled by varying the height of the first electrode and the tilt during the lithography of the second one. STEM 2D imaging of the FIB thin lamellas, as well as the chemical mapping performed by EDX evidence the insulator-metal-insulator layers, formed by Pt nanoparticles and Al<sub>2</sub>O<sub>3</sub>, and the Pd electrodes that are insulated by a TiO<sub>2</sub> layer.

An alarming aspect was the presence of Pd nanoparticles in the gap. Here I must mention that the electrical measurements were not typical of a short circuit, but the device had typical characteristics of a vertical metal-insulator-metal structure. Therefore, STEM electron tomography was employed to elucidate the presence of Pd particles in the gap (Figure 3 c)-f)). The reconstructed volume as well as the computed model showed that the Pd particles were not in contact with each other. They could be formed during the lithography of the second electrode due to an unperfected shadowing<sup>30</sup>. However, this is only an assumption and this should be proven in future experiments for which TEM analysis should be performed after each step of the synthesis method, *i.e.* after the evaporation of each Pd electrode.

Coming back to the Pt particles shown in Figure 3 a), my colleague Dr. Etienne Puyoo deposited the metal-insulator-metal layer on a polyamide substrate or kapton by developing a pressure gauge having a high sensitivity<sup>31</sup>. One of the applications of such a pressure gauge will be described in the perspectives of this document (section 5.1.1).

## 1.2.2 Electroactive area from porous oxide films loaded with Ag nanoparticles

The study of Ag nanoparticles dispersed in mesoporous TiO<sub>2</sub> films was made in the frame of [Nelly Couzon's PhD<sup>ii</sup>](#), dedicated to the synthesis and characterization of the photo-electrochemical proprieties of Ag nanoparticles dispersed in mesoporous films, under the supervision of Prof. Arnaud Brioude, Dr. Mathieu Maillard and Dr. Laurence Bois from LMI laboratory and supported by the French Ministry of Research and the Labex iMUST of Lyon University.

Ag nanoparticles interact with the surrounding environment having a photochromatic behavior when they are dispersed into a mesoporous TiO<sub>2</sub> thin film. This is of interest for electrocatalytic applications. However, during the electrocatalytic process, their photocatalytic capabilities decrease with time due to the fact that Ag particles increase in size and migrate within the film. The evolution of Ag nanoparticles was in general studied as a function of time and environment. But, the effect of their position into the support on their electrochemical response was rarely considered.

In this study the electrochemical activity of Ag nanoparticles was assessed considering their position in the TiO<sub>2</sub> mesoporous film as a function of the irradiation conditions. Two different mesoporous films of TiO<sub>2</sub> and Fe<sub>2</sub>O<sub>3</sub> supporting Ag nanoparticles were synthesized by Evaporation Induced Self Assembly (EISA) and deposited on Fluorine – doped Thin Oxide (FTO). The synthesis details and the electrochemical characterization are detailed in Nelly's thesis and in the references<sup>32,33</sup> and will not be described in this document. I will focus only on the electron tomography investigations.

STEM ET was used to investigate the Ag nanoparticle positions within the TiO<sub>2</sub> film. The goal was to compare Ag particle positions in the reference sample obtained after the synthesis with those in two other samples, submitted to 50 cycles of cyclic voltammetry (CV) under a monochromatic radiation of 360 nm and under white light. For the both irradiated samples, the CV cycles revealed the disappearance of the redox peaks despite the presence of the Ag nanoparticles within the film.

---

<sup>ii</sup> Nelly Couzon, Synthèse et propriétés photo-électrochimiques de nanoparticules d'argent intégrées dans des films d'oxydes mésoporeux, l'Université Claude Bernard Lyon 1, Ecole Doctorale 206, Ecole Doctorale de Chimie de Lyon, 25/09/2018.

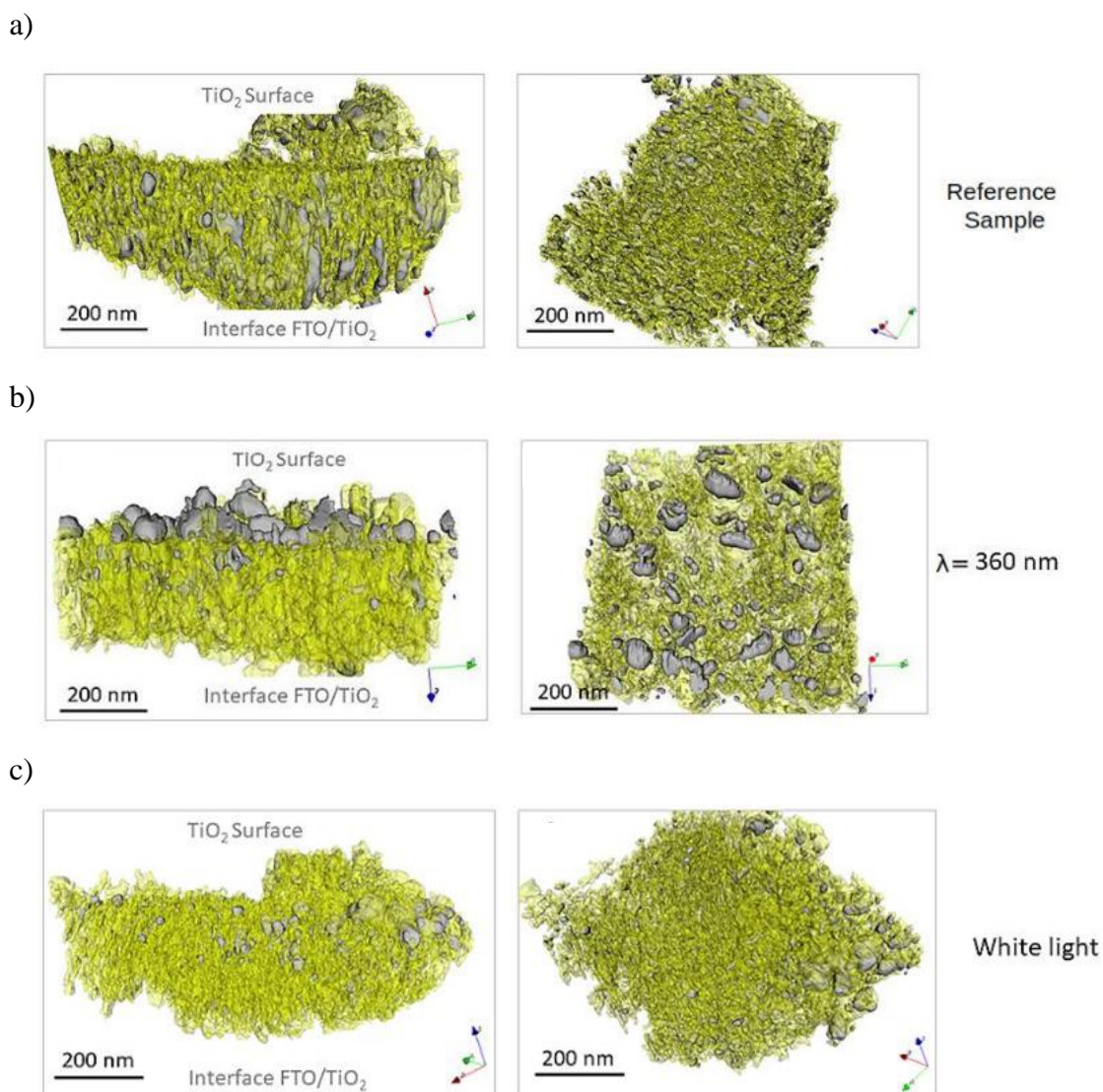


Figure 4: 3D models (side views on the left and top views on the right) of Ag nanoparticles (in gray) dispersed in TiO<sub>2</sub> thin films (in yellow). a) reference sample in which Ag nanoparticles have a homogeneous distribution within the TiO<sub>2</sub> mesoporous matrix, b) after 50 CV cycles under UV and c) under white light. It can be seen that the Ag particles do agglomerate at the surface of the TiO<sub>2</sub> film, leaving the interface with the FTO support. Image modified from<sup>34</sup>.

Figure 4 shows the 3D models of the studied samples. It can be seen that in the initial sample, the Ag particles, represented in gray, were homogeneously distributed within the thickness of the TiO<sub>2</sub>. Their average size was measured equal to 13 nm. Once they were submitted to a photo-electrochemical activity, the Ag particles started to agglomerate and migrate towards the surface of the thin film, forming bigger particles at the surface. The fact that the Ag nanoparticles did migrate from the interface with the FTO support explained the decrease, even

the disappearance, of the redox peak corresponding to Ag.

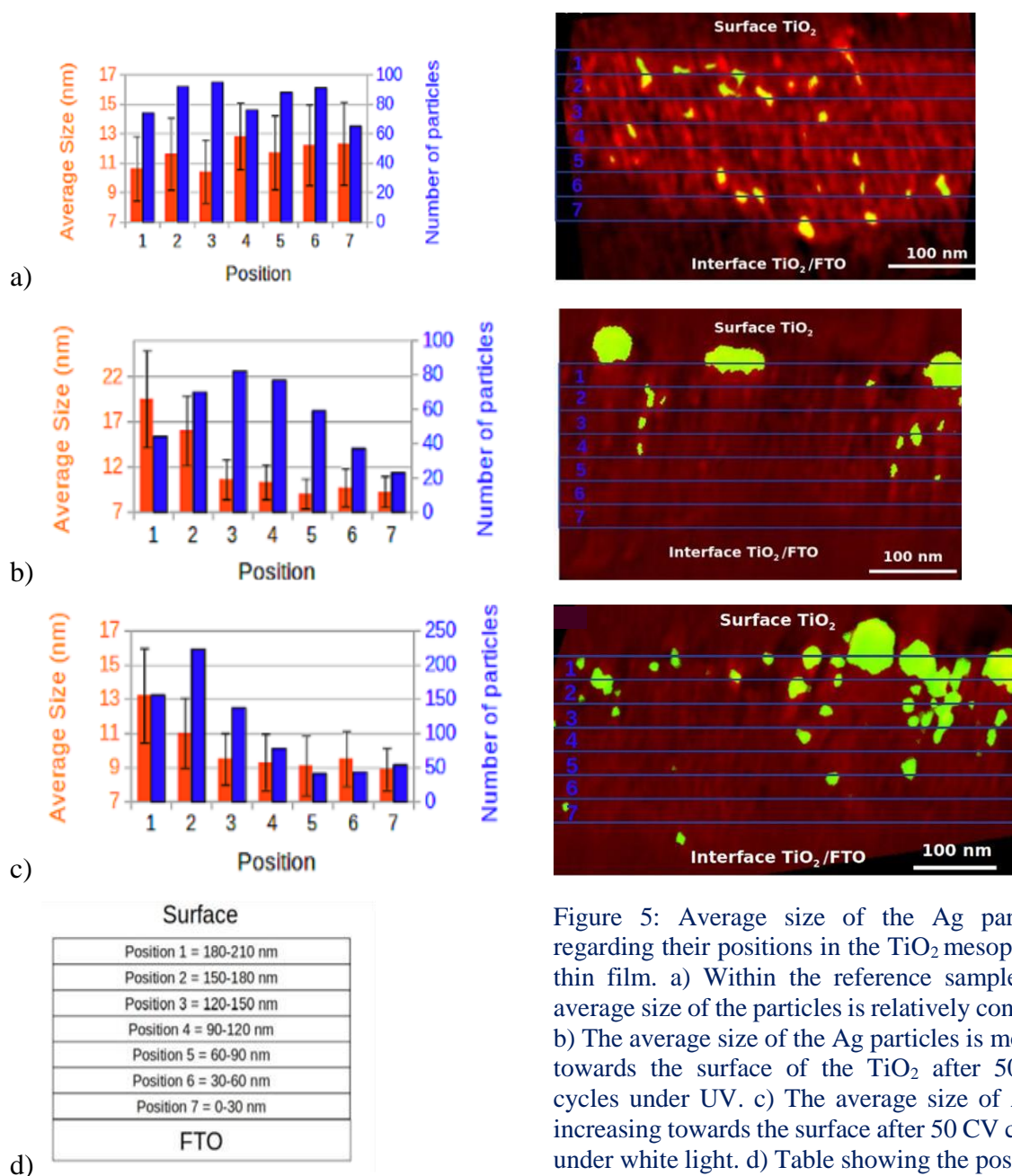


Figure 5: Average size of the Ag particles regarding their positions in the TiO<sub>2</sub> mesoporous thin film. a) Within the reference sample, the average size of the particles is relatively constant. b) The average size of the Ag particles is moving towards the surface of the TiO<sub>2</sub> after 50 CV cycles under UV. c) The average size of Ag is increasing towards the surface after 50 CV cycles under white light. d) Table showing the positions of the measurements. The average size was calculated from the surface of the TiO<sub>2</sub> considered as “Position 1” towards the FTO support considered “Position 7” with a step of 30 nm. Image modified from<sup>34</sup>. Credits to Dr. Nelly Couzon.

To accurately quantify the migration of the Ag nanoparticles, the volumes of analyzed films were oriented and slices of 30 nm thickness were virtually cut. The thickness of the virtual slices was chosen as a function of the thickness of the TiO<sub>2</sub> film and was set to around twice as big as the average size of the Ag particles in the initial sample. The average sizes of the Ag particles are shown in Figure 5 as a function of their positions. As expected in the reference

sample, the average size, in red, and the number of nanoparticles, in blue, were relatively constant, which characterized a uniform distribution.

On the contrary, while the samples are submitted to a photo-electrochemical activity, the average sizes and the number of Ag nanoparticles confirmed that Ag did migrate from the interface between TiO<sub>2</sub> and the support towards the surface. Due to the fact that the pores were relatively small and the Ag relatively big, the migration was most probably made by Ostwald ripening.

To sum up, STEM ET has allowed a better understanding of the redox deactivation while the Ag nanoparticles were still visible at the surface of the film. Thanks to these crucial information, my colleagues found a way to reactivate the catalyst by adding, between two voltammetry cycles, a chronoamperometry sequence under irradiation that has restored the redox peak of Ag together with the expected electrochemical properties of the samples<sup>34</sup>.

## 2 Beam sensitive materials in 3D - the need to record images faster

Electron beam-sensitive materials, such as silica, polymers or zeolites, etc. are the subject of many studies in electron microscopy due to their numerous fields of use. However, their analysis in TEM is not an easy task, as the electron beam causes undesirable damage to their structure and morphology during observation. Figure 6 shows an example of nanostructured silica. A 2 min irradiation test with an electron dose rate of  $700 \text{ e}^-/\text{nm}^2\text{s}$  was performed. The first image (in red) and the last one (in green) were aligned and superposed. It can be seen that a perfect alignment was not possible due to the fact that the global shape of the object changed due to the electron beam irradiation.

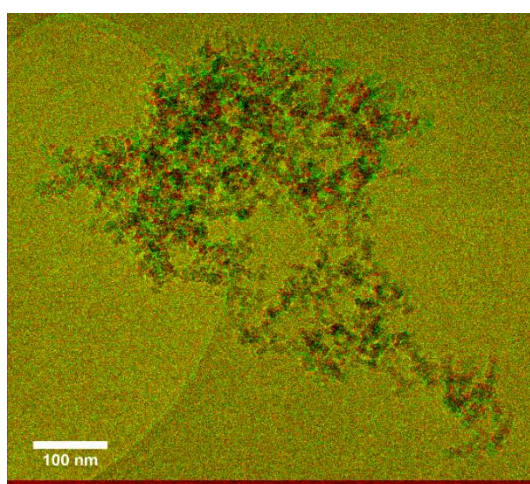


Figure 6: Irradiation test of a silica aerogel. The electron dose rate was  $700 \text{ e}^-/\text{nm}^2\text{s}$  and an image was recorded every 5 s during 2 minutes. The first image (in red) and the last image (in green) are superposed. Their perfect alignment is not possible due to irradiation damage. (Thesis of Bruno Chal, section 2.2.2.).

### 2.1 Technical methods to record low electron dose images

In order to avoid irradiating too much the sample, the first action that a user will take is to reduce the electron flux and eventually to reduce the total time that the sample is exposed to the electron beam. At this point I would like to discuss two possibilities that could be employed in electron tomography and were successfully applied in my research.

#### 2.1.1 Low dose in “conventional” BF electron tomography

It was mentioned above (section 1.1) that software are available to track regions of interest and record images of the sample at given angles. To be more precise, for each tilt value before recording an image, the region of interest is tracked using algorithms such as cross-correlation, and the focus is determined by recording successive images at different defocusing values. In general, those steps are made on the same object, that is suffering a long total exposure time to

the electron beam and risks to suffer from beam damage. The “advanced electron tomography” routine is a Digital Micrograph plugin developed by [Gatan®](#)<sup>iii</sup> that allows to record tilt series in BF mode at a very low electron dose. It performs the tracking and the focus outside the region of interest, preventing the analyzed object to be continuously exposed to the electron beam and therefore to suffer too much from beam damage. An example of its application is provided later in section 2.2.1. It must be mentioned that this technique allows the acquisition of tilt series for which the sample has received a very low electron dose, but the total recording time of a tilt series is very long, in the order of tenths of minutes. Such a long time could be employed in the study of materials – such as polymers or zeolites - but only under high vacuum, being not applicable in *operando* investigations.

### 2.1.2 Fast image recording for electron tomography

Even if the advanced electron tomography plugin from Gatan allows the 3D analysis of beam sensitive materials, the acquisition may remain too long. It is not well-suited to the study of a sample submitted to different physical parameters, such as gas or liquid pressure, temperature or physical stress. It is worth mentioning here that the recording duration of a tilt series depends on the imaging mode. Actually, the BF mode is the mode that allows the fastest image recording. However, even in this imaging mode, the acquisition can take several tens of minutes. In the STEM mode, the acquisition duration can reach 90 minutes depending of the image size and the scan speed. The longest recording times, that can exceed 2 h, are reached in analytical modes, such as in energy-filtered TEM or in EDS.

Algorithms such as cross-correlation can be used to track and to set the focus on the sample when tilt images are recorded at different angles. If those operations are automatically made by a software, around 45 s to 60 s are needed at each tilt angle. A first solution to reduce the total recording time of a tilt series is to perform the tracking and the focus manually, by an experienced user. In such conditions, the acquisition time of a full tilt series can be reduced to 1 to 4 minutes, depending on the camera used and the tilting speed.

The development and applications of fast imaging recording techniques for electron tomography have been the core of my research activity since September 2012. The [thesis of](#)

---

<sup>iii</sup> <https://www.gatan.com/>



[Siddardha Koneti](#)<sup>iv</sup> was funded by the French Minister of Research and Higher Education, IFPEN represented by Dr. Anne-Sophie Gay, and by Labex IMUST of Lyon University. Siddarda Koneti worked under the direction of Dr. Thierry Épicier. He showed that the total recording time of tilt series could be reduced down to several seconds<sup>35</sup>, keeping/preserving an acceptable spatial resolution.

Two methods were proposed to reduce the acquisition time of a tilt series in BF mode. The first one is the so-called “**optimized step-by-step**” acquisition. The sample is rapidly tilted to a given tilt angle and the user tracks and adjusts the focus, then an image is recorded. If we consider that the time needed to adjust the settings within the field of view of the camera is 1 s, the acquisition of a tilt series between +70° and -70° with a tilt step of 2° can be performed in 70 s - 90 s, when considering the recording speed of the camera. Such fast acquisitions have been made possible using a homemade Digital Micrograph plugin developed by Dr. Thierry Épicier and Dr. Cyril Langlois. This plugin tilts the sample at a controlled speed and records images at a given exposure time. As a remark, the maximum tilt speed of a goniometer using the current technology is around 28 °/s.

The second method developed during Siddarda’s thesis is the **continuous rotation and images recording** (CRRET). Of course, this method would be the fastest way to record a tilt series. However, it must be considered that images may be blurred because the object is moving during image acquisition. If the exposure time of the camera is short enough with respect to the object speed, the motion blur is negligible and many images remain sharp. As a consequence, while continuously tilting the sample, images must be recorded using appropriate exposure times *i.e.* shortest as possible.

At this point it must also be mentioned that the motion blur in the image can have different sources. Motion blur can be caused by goniometer high frequency vibrations while rotating at high speed, or/and random shifts of the sample that can be caused by mechanical imperfections during sample rotation or caused by the user. Of course, the aim of the research work was not to understand the different types of blur that could occur during a fast rotation of the sample. However, some simulations were performed to understand the influence of the rotation speed in the recorded motion blur in an image as a function of the exposure time of the camera.

---

<sup>iv</sup> Siddadha Koneti, In situ and 3D Environmental Transmission Electron Microscopy of Pd-Al<sub>2</sub>O<sub>3</sub>Nano catalysts: fast tomography with applications to other catalytic systems in operando conditions and to electron beam sensitive nanomaterials, École doctorale Matériaux de Lyon, INSA-Lyon, 5/12/2017.

A typical 2D projection of a silicalite-1 cage that encloses Ag nanoparticles<sup>36,37</sup> (later in the section 3.1.2 more details are provided about the sample) is shown in Figure 7 a). It was used as a rotated phantom that was projected along the blue arrow representing the electron beam. Each rotation was performed with an increment of  $1^\circ$  to  $10^\circ$  representing the angular coverage of the sample during a single exposure time of the camera. In other words, the object was rotating with  $1^\circ$  to  $10^\circ$  during the recording of a single image. At the bottom of Figure 7 a), the corresponding 1D projections are shown with a thickness of 3 pixels (to be observable).

The profile intensities of the 1D projections are shown in Figure 7 b). Starting from the bottom of the profiles, it can be seen that the reference profile marked “blur  $0^\circ$ ”, representing the 1D projection of a stable image, had many variations of the intensity. The blur represented the movement of the object that was recorded in the 1D projections while the phantom was rotated. If the rotation increment increased from  $1^\circ$  to  $10^\circ$ , more rotation blur was recorded in the projection. Therefore, while the rotation of the object was faster, or, in other words, a wider angular amplitude was traveled during a single exposure of the camera, more rotational blur was recorded in the image. Therefore, the information was lost, as evidenced by the fact that the intensity profiles were becoming smoother. Of course, the question is how much rotation blur can be accepted in a recorded projection? To answer to that question, we compared the original image/phantom and an “ideal” weighted back projection (WBP) reconstruction made by tilting the phantom from  $+90^\circ$  to  $-90^\circ$  with an incremental step of  $0.1^\circ$  (meaning 1,800 projections) with those made by using projections recorded at different incremental angles. The “ideal” reconstructed image was compared with other images reconstructed by WBP but for which the 1D projections were selected every  $1^\circ$  to  $5^\circ$  (Figure 7 c)) similarly to the step-by-step tilt series used in experimental ET. A second set of WBP reconstruction was obtained using 1D projections simulating the continuous rotation of the sample (Figure 7 d)). The reconstructions were performed using 1D projection on which motion blur of  $1^\circ$  to  $5^\circ$  was recorded. Here, it must be mentioned that the motion blur was simulated by summing within the given angular interval ( $1^\circ$  to  $5^\circ$ ) images rotated with a step of  $0.1^\circ$ . Therefore, to simulate a rotation blur of  $1^\circ$ , 10 images rotated with a step of  $0.1^\circ$  were summed, and to simulate a rotation blur of  $5^\circ$ , 50 images were summed.

Of course, in the “ideal” 2D reconstruction all the Ag nanoparticles were observed as well as the top and the bottom edges of the silica cage as in the “original” phantom. For the reconstructions made using the incremental tilt 1D projections (Figure 7 c)) while increasing the angular step, similarly to “conventional” tomography, (the angular step is marked in black) some of the details were lost. Indeed, the silica cages were less visible as well as some particles

situated away from the rotation center, that was in the center of the image. Accordingly, while more rotation blur was recorded in the 1D projections, the obtained reconstruction was less perfect: the edges of the silica cages were lost, and decentered particles were not visible anymore (Figure 7 d)).

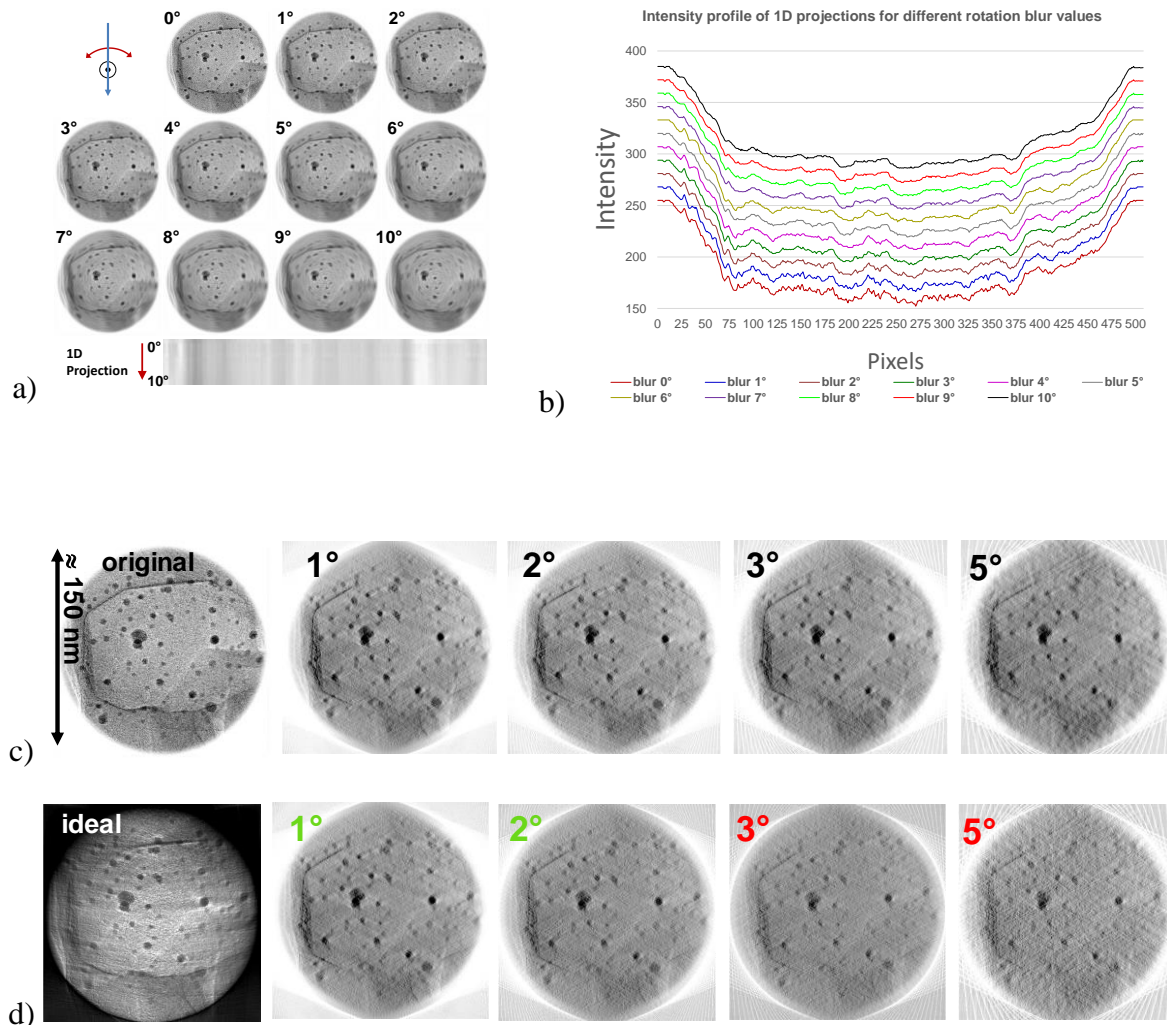


Figure 7: a) Images used as an object that is rotated around its center with an increment of  $0^\circ$  to  $10^\circ$ . On the bottom of the image are shown the 1D projections of the rotated images projected along the blue arrow that represents the electron beam. The dot in the center of the image is the rotation center. b) Intensity profiles of the 1D projections, showing that if more rotation blur is recorded in the projection, more the information is lost. When the 2D projection is recorded while the sample is static (blur  $0^\circ$ ), many intensity variations are visible in the profile. If the phantom is rotating, the profiles are smoothed, meaning that information is lost. c) Original image and images reconstructions using classical step-by-step tilt made with projections recorded with an increment of  $1^\circ$  to  $5^\circ$ . d) “Ideal” WBP reconstruction using 1,800 projections tilted over  $\pm 90^\circ$  with an increment of  $0.1^\circ$  and reconstructions made by using projections having a rotation blur recorded of  $1^\circ$  to  $5^\circ$ . Image modified from reference <sup>35</sup>. Credits to Dr. Thierry Épicier.

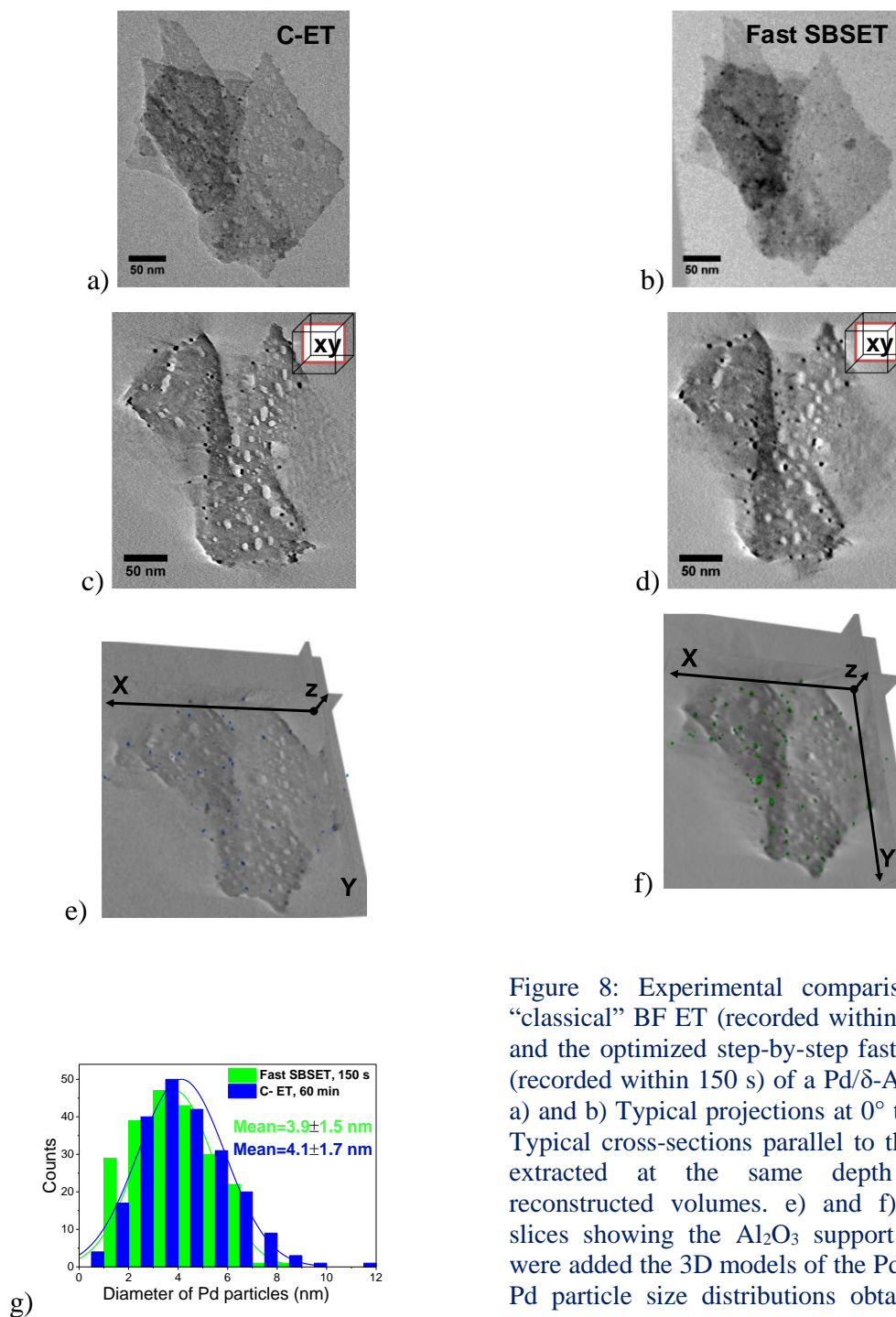
From the observational point of view of the experimentalist, it was considered that a rotation blur of  $1^\circ$  and  $2^\circ$  could be accepted (Table 1 marked on green), because the degradation of the

images having 2° rotation blur is similar to those obtained using 1D projections selected every 2°. Table 1 shows calculated values of rotation blur that could be recorded in a projection in function of the tilting speed and exposure time of the camera, parameters that could be used experimentally. The blur values were obtained by multiplying the rotation speed of the sample (in °/s) with the exposure time of the camera (in s/frame). The color code indicated, on green and yellow, the blur that could be accepted, and on red the values that were not appropriate and could jeopardize the reconstructed volume. However, it must be mentioned that electron tomography is a compromise between the experimental parameters, the electron flux and the information that is searched, therefore those values are not absolute ones but are more a personal point of view based on personal experience. At low rotation speed, the rotation blur was very low but the total recording time of a tilt series was too long, therefore it was considered as non-acceptable. Overall, Table 1 shows that even using normal recording cameras, the recording of a full tilt series could be performed in several minutes.

Table 1: Integrated blur calculated in function of the rotation speed (on brown) and the exposure time of the camera (on orange). The exposure times of usual cameras were considered as well as those of fast recording cameras. The values of the rotation blur that could be accepted are shown on green and those that could be considered as inappropriate are shown on red.

Tilting speed (°/s)			0.1	1	2	3	4	5	10	20	28
Time for covering 140° (s)			1400	140	70	46.6	35	28	14	7	5
Exposure time (s/frame)	0.2	Recorded rotation blur (°/frame)	0.02	0.2	0.4	0.6	0.8	1	2	4	5.6
	0.1		0.01	0.1	0.2	0.3	0.4	0.5	1	2	2.8
	0.04		0.004	0.04	0.08	0.12	0.16	0.2	0.4	0.8	1.12
Acceptance color code:			Yes								No

To prove that fast recording of tilted series is reliable, both recording methods (optimized step-by-step acquisition and continuous recording and rotation) were compared with the classical recording method. A sample of Pd nanoparticles supported by  $\delta$ -Al<sub>2</sub>O<sub>3</sub> is shown in Figure 8. The optimized step-by-step (SBSET) method allowed the full recording of a tilt series from -71° to 66° in 150 s (2 min 30 s). The classical method was performed using the FEI tomography software in 60 min. The Pd nanoparticles of the same sample were followed using the BF imaging mode. Both methods provided comparable results: we found 212 particles using fast tomography and 218 using the classical method, with an average size of 4 nm.



To test the continuous rotation and recording (CRRET) method, we used a sample of Pd nanoparticles supported by  $\alpha$ -Al<sub>2</sub>O<sub>3</sub> that is highly crystalline. Classical ET was performed in STEM. As expected in BF mode, some of the smallest Pd particles were lost due to diffraction contrast. However, for samples compatible with the BF mode, the results provided by the fast recording methods were reliable<sup>35</sup>. Here it must be mentioned that fast recording solutions in

STEM mode made possible a full tilt series recording in around 5 minutes<sup>38</sup>, time that is short enough to be used in some *operando* experiments.

### 2.1.3 SIRT-FISTA-TV reconstruction algorithm applied to fast electron tomography

In all my studies related to ET, the volumes were calculated using 16 iterations of the Algebraic Reconstruction Technique (ART)<sup>39</sup> or Ordered Subsets ART (OSART) implemented in the ImageJ plugin TomoJ<sup>27</sup> developed at Institute Curie by Dr. Cédric Messaoudi and Dr. Sergio Marco. Then, the 3D models were segmented and quantified using ImageJ, 3D Slicer<sup>29</sup> and/or Chimera<sup>40</sup>. As a short comment, in literature for the volume reconstruction is in general used the algorithm SIRT (Simultaneous Iterations Reconstruction Technique) but I observed that to obtain a good contrast in the volumes ART needs around 15-16 iterations when SIRT needs 30 or more iterations. Therefore, ART is faster, even it is considered “divergent at high number of iterations”. Moreover, the Tomoj plugin provides at the end of the volume reconstruction the converges tendency that was convergent, for a such low number of iterations.

In *operando* conditions, as mentioned in the previous section, a compromise is made between the experimental setup and the electron flux in order to record an exploitable signal-to-noise ratio in the tilt series, *i.e.* to have contrast in the reconstructed volume that allows the segmentation and the quantification of the 3D parameters. Moreover, the analyzed samples could have a very reduced contrast. Consequently, the calculated volumes could be very noisy and the information hidden in the noise. In the literature, several reconstruction algorithms have been developed, such as Compressed Sensing (CS)<sup>41</sup>, Total Variation (TV) regularization<sup>42,43</sup> and Discret Algebraic Reconstruction Technique (DART)<sup>44</sup>. Those algorithms are efficient in reducing the artifacts due to the missing wedge, created by the limited tilt of the sample. In addition, by using prior knowledge of the object, they combine the reconstruction with the *in situ* data segmentation of the volume.

In the framework of the ANR project [3D-Clean](#)<sup>v</sup> coordinated by Dr. Thierry Épicier, our colleagues Dr. Hussein Banjak (post-doc fellow), Dr. Thomas Grenier and Dr. Voichița Maxim from CREATIS laboratory developed a reconstruction algorithm called SIRT – FISTA – TV (Simultaneous Iterative Reconstruction Technique –Fast Iterative Shrinkage Thresholding

---

<sup>v</sup> 3D CataLytic Environmental IAb at the Nanoscale, ANR project n°15-CE09-0009-01 (2015-2019), Challenge 3 "Industrial Renewal".

Algorithm – Total Variation). This algorithm is dedicated to environmental electron microscopy, where the images recorded are systematically affected by blur and noise. SIRT<sup>45</sup> is a widely used reconstruction algorithm in electron tomography that is considered to be more stable compared with ART when using noisy projections and a high number of iterations. FISTA is an acceleration method that helps to speed up the convergence of the reconstruction algorithm and TV is a regularization method that preserves the edge of the object while removing the noise. In the current document, I will not enter into the mathematical description of the algorithm that can be found in the references<sup>46,47</sup>. I only show its schematic description in Figure 9.

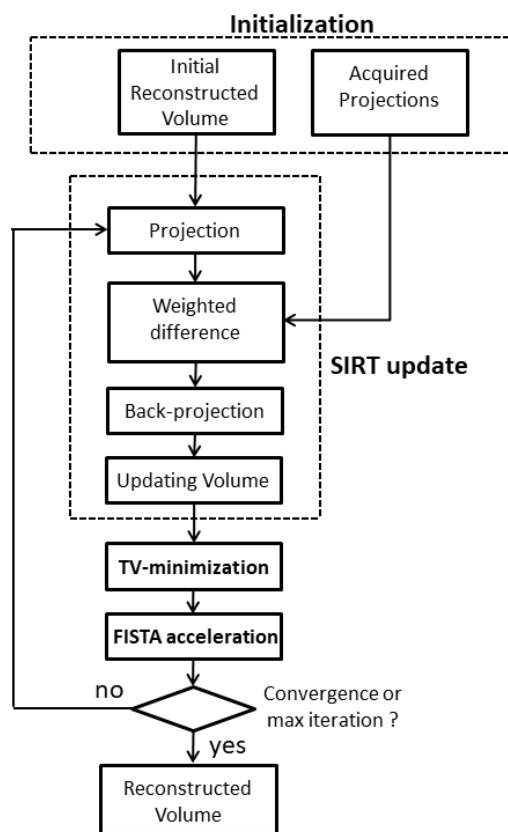


Figure 9: Schematic description of the SIRT-FISTA-TV algorithm. Credits to Hussein Banjak. Image from <sup>46</sup>.

To test the robustness of the SIRT-FISTA-TV algorithm, a phantom object of a random morphology was projected within  $\pm 70^\circ$ . The projections were affected by noise that simulated the real images recorded in electron microscopy. Then the projections were used for the reconstruction of the original phantom using SIRT-FISTA-TV. The obtained volume was compared with volumes computed with SIRT, SIRT with median filter, SIRT with Gaussian filter and SIRT with anisotropic filter (Figure 10). The results of the comparison clearly showed that the SIRT-FISTA-TV algorithm is more robust than SIRT when the projections used are noisy. To go further in the conviction that SIRT-FISTA-TV is reliable in ET performed in environmental conditions, the algorithm was tested by using projections affected by

translational as well as rotational blurred projections that are not shown here. However, some examples of its application in experimental electron tomography in *operando* conditions are given in the sections 3.1.1 and 3.1.3.

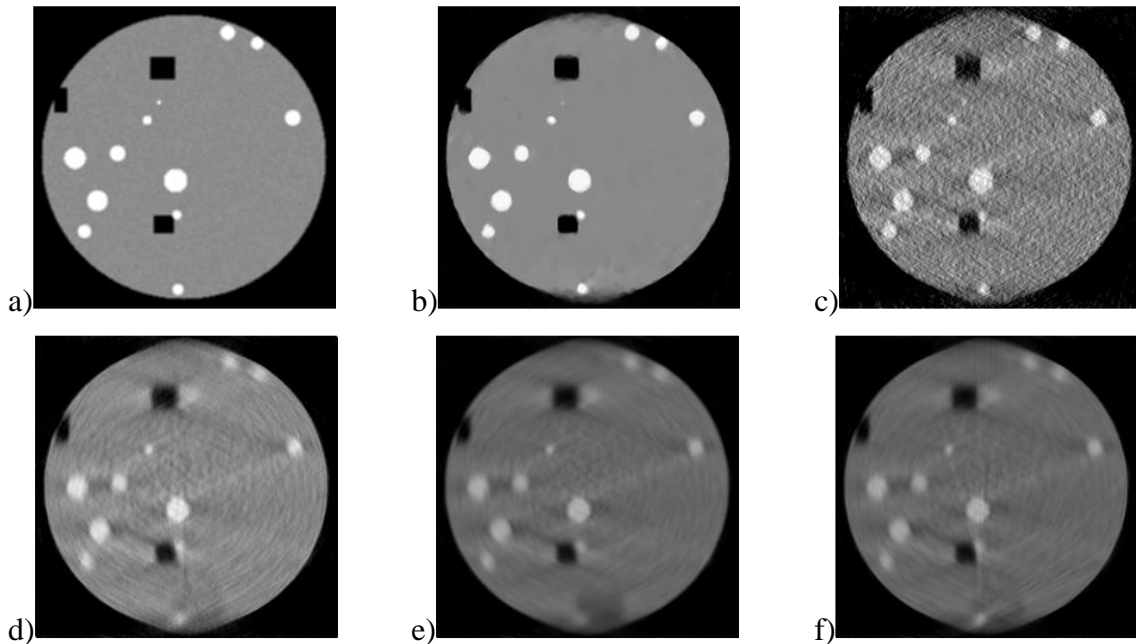


Figure 10: Cross-sections through a reconstructed 3D phantom projected within  $\pm 70^\circ$  with a step of  $2^\circ$ . a) Original phantom. b) Reconstruction using SIRT-FISTA-TV, c) SIRT, d) SIRT with median filter, e) SIRT with Gaussian filter f) SIRT with anisotropic filter. Credits to Dr. Hussein Banjak. Image modified from <sup>46</sup>.

## 2.2 Electron tomography applied to the study of beam-sensitive materials

As mentioned earlier, it is important to reduce at maximum the electron dose received by the sample to prevent sample degradation during image recording. To do so, a compromise must be found between the intensity of the electron beam, *i.e.* the electron flux, and the total exposure time. The compromise must be found by considering the contrast in the recorded images as well as its undesirable possible modifications of the sample morphology and chemistry. From the experimental point of view, it is advised to test the beam resistance of the sample. Of course, it can be argued that a beam-sensitive sample degrades as soon as it is under the electron beam. At this point, it can be answered that the compromise is pushed a bit further away. By testing the beam resistance of the sample, an electron dose can be determined under which the changes in the sample are as small as possible, actually not observable at the magnification at which the experiment is performed.



In this section I show some examples of beam-sensitive samples studied by electron tomography.

### 2.2.1 Nanoporous silica in 3D at low electron dose

I had the opportunity to study beam-sensitive materials developed in the MateIS lab for building insulation applications. One of the biggest challenges that humanity faces (after the economic crisis due to the Covid-19 pandemic) is the global warming. One of the many causes that implies the atmospheric temperature increase is due to the energy consumption of residential houses that represents 40% of the total energy consumption at the European level and at 45 % in France. Therefore, building insulation is one of the major aspects in the fight against climate change.

First studies in electron tomography concerning beam-sensitive materials were performed on nanostructured silica in the frame of [Anouk Perret's PhD<sup>vi</sup>](#), supervised by Dr. Geneviève Foray and Dr. Éric Maire in the framework of the MateIS-EDF joint laboratory. In this study, to reach the third dimension of such materials with complex morphologies, we used advanced electron tomography. This method allows a low-dose image recording, as explained in section 2.1.1. The goal was to study and to quantify the pore size distribution of three different types of silica

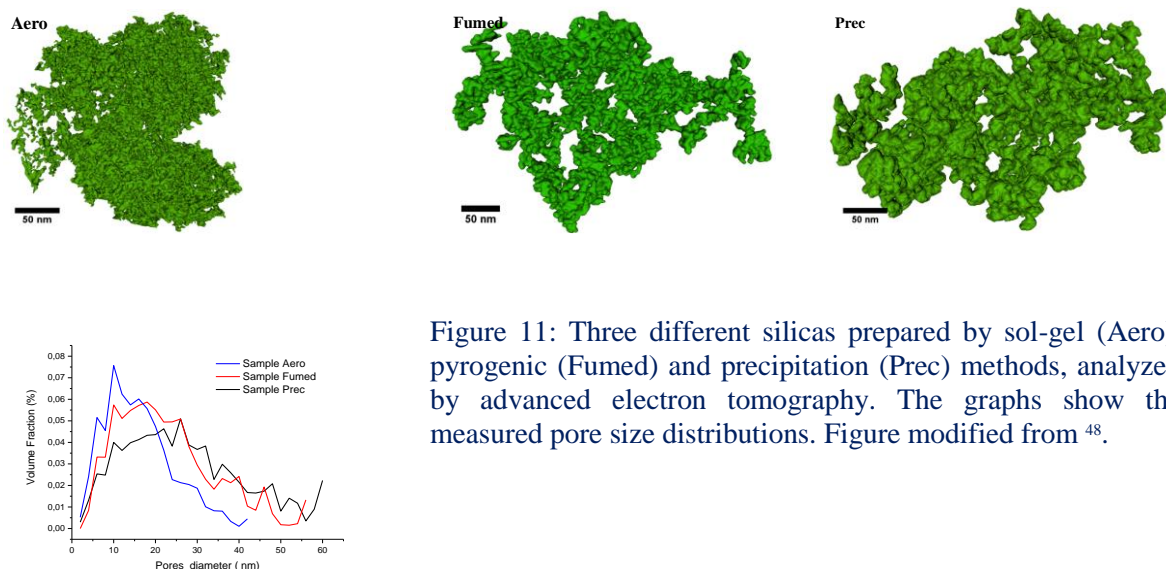


Figure 11: Three different silicas prepared by sol-gel (Aero), pyrogenic (Fumed) and precipitation (Prec) methods, analyzed by advanced electron tomography. The graphs show the measured pore size distributions. Figure modified from <sup>48</sup>.

structures that were prepared through different routes (sol-gel method (Aero), pyrogenic

---

<sup>vi</sup> Anouk Perret, Méthodologie de caractérisation microstructurale 3D de matériaux poreux structurés pour la thermique, Ecole doctorale : Matériaux de Lyon, INSA-Lyon, 13/04/2015.

method (Fumed) and precipitation method (Prec.)). The study was funded by METSA and conducted at IPCMS in Strasbourg.

We showed that the pores size distribution measured by ET depends on the preparation method. Actually, the size of the primary silica grains depends on the preparation method. The pores are formed by the assembly of the silica grains into aggregates and then into agglomerates. It is worth mentioning that the fresh silica grains are not spherical. Their shape is an ellipsoid and they are assembled in chain-like structures among which are formed the pores. While the silica grains become bigger (from aerogels to precipitated silica), the pores sizes increase. Indeed, the sol-gel method provides samples having the smallest silica grains with lengths around 5 nm and widths around 3 nm. The pores have an average of 10 nm, the pore sizes between 3 nm and 30 nm represent 50 % of the total volume of the sample. The pyrogenic method provides the intermediate grain and pore size. The silica grains are around 20 nm long and 10 nm wide, and the pores represent 63 % of the volume of the sample with an average size of 20 nm (sizes between 7 nm and 45 nm). The bigger silica grains (33 nm long and 15 nm wide) are provided by the precipitation method. The pores of the precipitated sample represent 66 % of the total volume of the sample. They have an average size of 25 nm with sizes ranging between 10 nm and 60 nm<sup>48</sup>. Those findings were complementary with other consecrated techniques, such as BET, Hg porosimetry, and helped to improve the fabrication of such super-insulating materials.

### 2.2.2 Aging process of nano silica for building insulation

An irradiation test made in the framework of [Bruno Chal's PhD](#)<sup>vii</sup> is shown in Figure 6. Bruno's PhD was supported by the French Environmental Transition Agency (ADEME) and supervised by Dr. Geneviève Foray, Prof. Jean-Marc Chenal and Prof. Karine Masenelli-Varlot. The aim of the PhD was to study the physio-chemical phenomena occurring during the aging of materials used for thermal building insulation. Bruno, in his thesis, assembled many different characterization techniques such as N<sub>2</sub> sorption/desorption, Hg porosimetry, Fourier Transform Infrared (FTIR) and Small Angle X-ray Scattering to understand the aging of insulation materials such as precipitated and pyrogenic silica as well as silica aerogels<sup>49-52</sup>. Electron microscopy played an important part in the visualization of samples. The aging process was performed in controlled atmosphere at 70°C and 90% relative humidity during several days.

---

<sup>vii</sup> Bruno Chal, Vieillissement thermohyrique de silices nanostructurées, vers une compréhension des mécanismes, Ecole doctorale Matériaux de Lyon, INSA-Lyon, 08/11/2019.

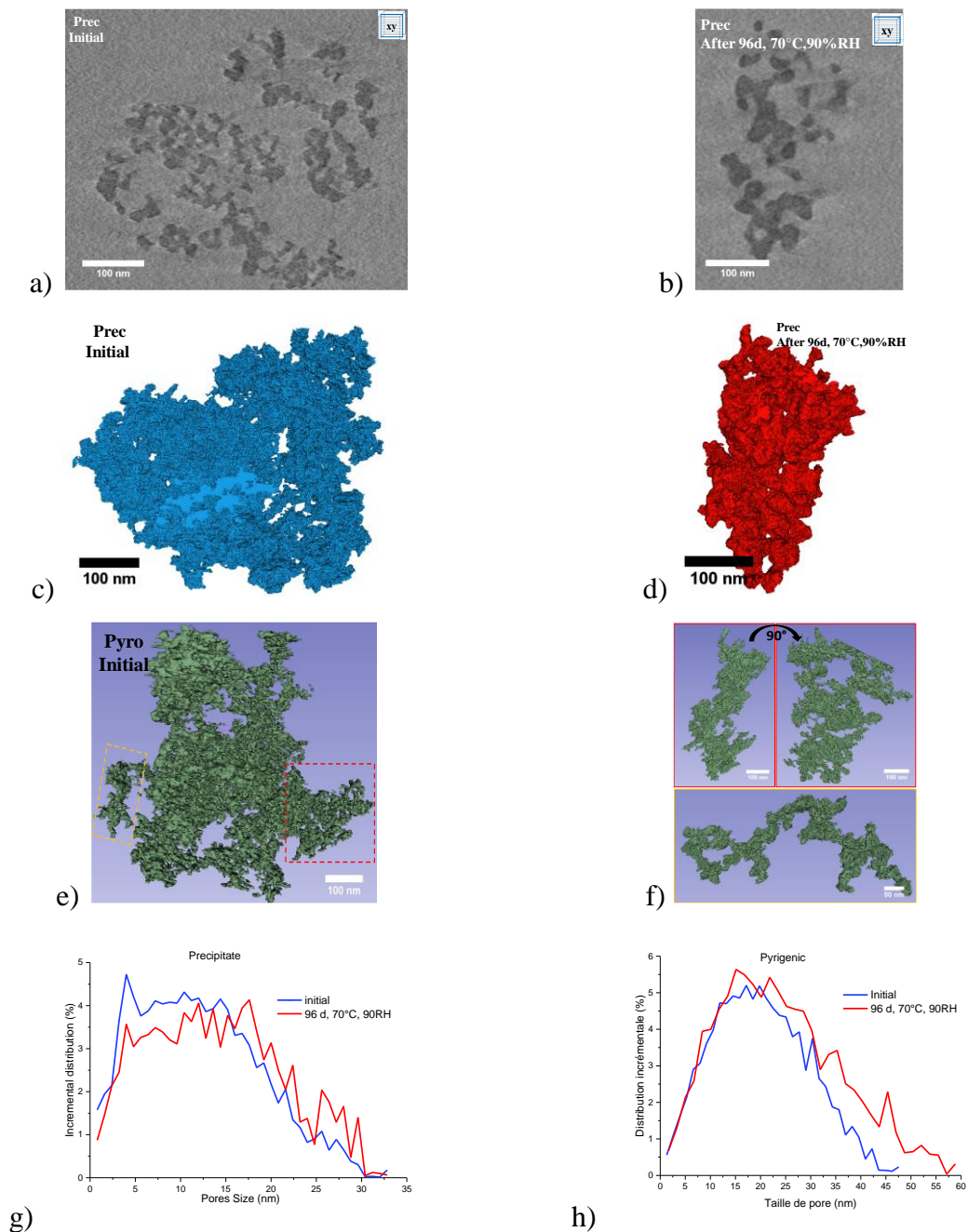


Figure 12: a) and b) Cross-sections through the reconstructed volumes in the XY plane of a precipitated silica analyzed by optimized SBSET in initial conditions and after been aged during 96 days at 70°C and 90% RH. c) and d) 3D models of the initial sample (in blue) and of the aged sample (in red). e) 3D model of an initial sample made via the pyrogenic method. f) Zoom of the image in (e) marked with the red and yellow rectangles showing the porous structure of silica aerogel (image modified from <sup>52</sup>). g) and h) Pore size distributions of two families of samples showing the pore size increase during aging.

7 different samples were studied during Bruno's PhD thesis. The imaging was performed in high vacuum, using a Jeol 2010F. The tilt series for electron tomography were recorded using a FEI Titan environmental transmission electron microscope (ETEM) equipped with a spherical

aberration correction of the objective lens and a Gatan OneView camera. The tilt series were acquired using the SBSET method.

Figure 12 shows initial and aged silica samples prepared by the precipitation and pyrogenic methods. The most challenging part in the 3D study was the high sensitivity of the samples to the electron beam. In this work, we were nevertheless able to visualize the assembly of the silica grains at different length-scales. It was shown in the previous study (section 2.2.1) that the size of the silica grains depended on the preparation method and they are forming a highly porous nano-object by self-assembling into “small silica chains”. Those chains form some “pillars” that do form a porous structure with a large pore distribution (e) and f))<sup>52</sup>. During aging, the silica grains coalesce, and the initial contact points between them grow. The contact points turn into “necks” and finally, larger silica grains are formed by coalescence. The small pores disappear, and the pore size distribution is shifted towards bigger sizes (Figure 12 g) and h)). The advantage of using fast image recording is the low electron dose received by the sample. For the precipitated sample, the electron flux was reduced down to 830 e<sup>-</sup>/nm<sup>2</sup>s and 1,120 e<sup>-</sup>/nm<sup>2</sup>s for the initial and the aged samples, respectively. This corresponds to total electron doses received by the samples during the tilt series recording of 99,600 e<sup>-</sup>/nm<sup>2</sup> and 13,5000 e<sup>-</sup>/nm<sup>2</sup> for the initial and the aged samples, respectively. For the pyrogenic samples, the electron flux was set to 600 e<sup>-</sup>/nm<sup>2</sup>s and 7300 e<sup>-</sup>/nm<sup>2</sup>s for the initial and the aged samples, respectively. This led to total electron doses of 74,000e<sup>-</sup>/nm<sup>2</sup> and 90,000 e<sup>-</sup>/nm<sup>2</sup> for the initial and the aged samples, respectively.

To be certain that the electron dose did not affect the experiment, the sample resistance was checked before each experiment. In general, we found that the maximum electron dose that can be accepted by our silica samples was around 110,000 ±15,000 e<sup>-</sup>/nm<sup>2</sup>. However, the electron dose accepted by the aerogels was much lower. Here, I must add that aerogels were very difficult to image by electron microscopy due to their fragile structure. However, using an electron flux lower than 600 e<sup>-</sup>/nm<sup>2</sup>s, it was possible to analyze them in 3D. All the results are available and well explained in [Bruno Chal's thesis](#).

### 2.2.3 LDH dispersed in latex nanocomposite

Another study of a beam-sensitive material that I would like to show, performed in high vacuum using the ETEM, concerns a soft latex reinforced with nano-platelets. The latex corresponded to a methyl methacrylate (MMA) butyl acrylate (BA) co-polymer and the filler was Mg<sub>3</sub>AlCO<sub>3</sub> layered double hydroxide nanoplatelets (LDH). This study was performed in the framework of

Siddhartha Koneti's PhD thesis, in cooperation with Dr. Florent Dalmas. The study represented one of the feasibility tests of the fast-tilted images recording for electron tomography.

The samples were prepared by cryoultramicrotomy. The irradiation test for this experiment was performed with an electron flux of  $2,020 \text{ e}^-/\text{nm}^2\text{s}$ , revealing that the maximum electron dose that the sample could withstand was around  $800,000 \pm 50,000 \text{ e}^-/\text{nm}^2$ . A SBSET tilt series was recorded from  $-70^\circ$  to  $+70^\circ$  with an angular step of  $1^\circ$ , a relaxation time of 1 s at every degree of rotation and an exposure time of 0.2 s for each projection. The rotation speed of the goniometer was  $5^\circ/\text{s}$ , which gives a tilting time of 0.2 s between two successive tilt angles. A tilt series of 141  $4\text{k} \times 4\text{k}$  images (each pixel representing 0.13 nm in the X direction) was thus recorded within 200 s. Under the selected conditions, the material received a total dose of  $800,000 \text{ e}^-/\text{nm}^2$ , at the limit of the previously determined acceptable electron dose. Figure 13 a) shows images extracted from the reconstructed volume. Figure 13 b) displays an oriented cross-section perpendicular to the LDH platelets. The distance between two adjacent platelets could be measured close to the theoretical value of  $0.77 \text{ nm}$ <sup>35,53</sup>.

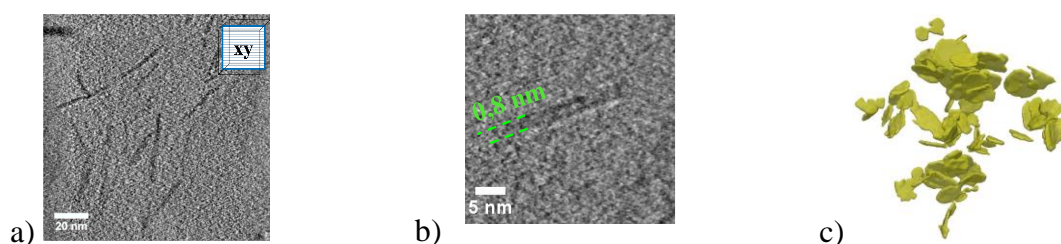


Figure 13: Soft latex matrix reinforced with  $\text{Mg}_3\text{AlCO}_3$  nanoplatelets (LDH). a) XY plane within the volume. b) Oriented cross-section showing the distance between the LDH nanoplatelets. c) 3D model of the LDH distribution within the polymer matrix. Image modified from<sup>35</sup>.

### 3 *Operando* electron tomography

The fast recording of tilted images opens the way to the 3D study of beam-sensitive materials with no special prior preparation of the sample. Moreover, fast imaging recording enables the 3D study of samples in controlled conditions, such as temperature and gas pressure. Under *operando* conditions, the sample transformations can be followed in 3D by capturing quasi static intermediary images of the transformation process. Therefore, the fast images recording for electron tomography is a step forward in the study of samples in conditions mimicking their real work environment.

#### 3.1 Materials in controlled environment in 3D

During the last few years, environmental electron microscopy has known an intense development, with both closed environmental cells and dedicated environmental microscopes (ETEM). Specifically designed *in situ* experiments corroborated with *ex situ* ones help to better understand how materials behave in different conditions or how some catalytic activities occur in real conditions. However, at this point it is important to mention that in an electron microscope, only some of the real conditions can be simulated. The microscope has its own environment, and the electrons used to form the images will always influence the designed experiment. The way the results are obtained using environmental electron microscopy should never be taken for granted and it should always be corroborated with experiments performed outside the microscope. The electrons influence over an experiment should indeed always be quantified. In the previous section, it was mentioned that a high electron dose can destroy a sample during analysis. In the same manner, during *operando* experiments, the electrons can induce phenomena that are not linked to the chemical interactions under study. It is therefore wise to work with a very low beam intensity in order to have a minimal influence over the experiment. During the last 9 years, I have the opportunity to gain some experience in *operando* electron microscopy by working on a TITAN FEI ETEM<sup>54</sup> on which it is possible to insert variable gases up to 25 mbar but also to tilt the sample at high angles. Using such microscope, it was possible to develop the recording of fast tilted images to follow the evolution of nanomaterials in 3D. Also, it allowed the correlation between *operando* experiments and 3D analysis.

In the next sections I will expose some studies made in *operando* conditions using the ETEM installed at CLYM.

### 3.1.1 Soot combustion supported by YSZ in 3D *operando*

It is known that diesel engines are producing, among other exhaust products, carbon nanoparticles as soot. Such particles by polluting the atmosphere, can cause dangerous diseases when inhaled. To avoid the elimination of carbon soot in the atmosphere, Diesel Particulate Filters (DPFs) have been installed on the exhaust system of cars. However, more developments are needed in order to be certain that the soot is not released into the atmosphere, and one solution is the soot combustion inside the DPF.

This study was performed during the PhD thesis of Siddadha Koneti in cooperation with the group of Dr. Philippe Venoux from IRCE Lyon (CNRS, Université Lyon 1). The goal was to

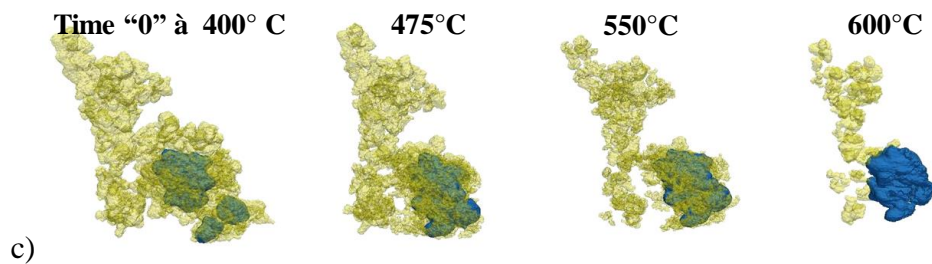
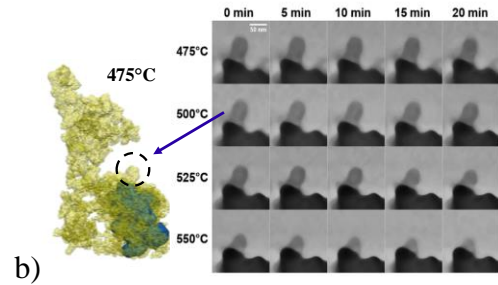
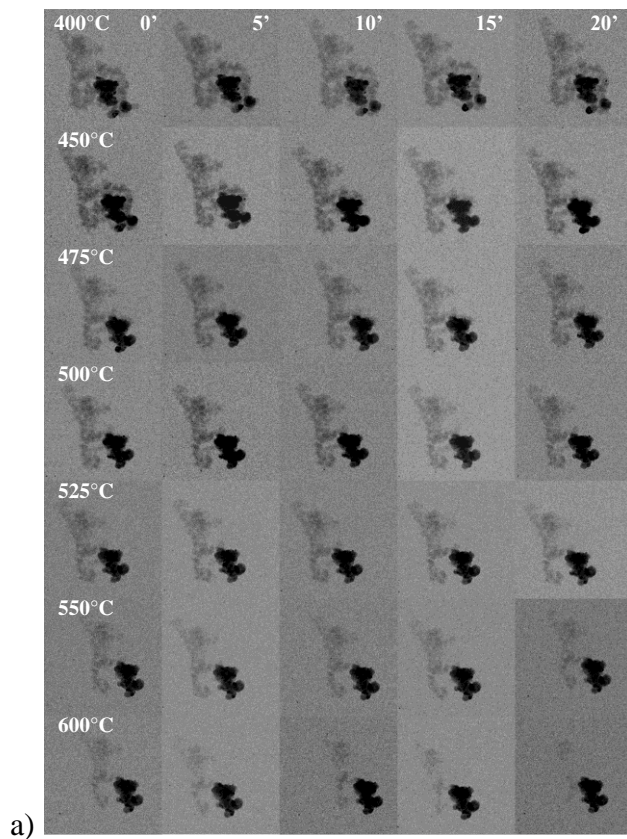


Figure 14: 3D *operando* study of the soot combustion while supported by  $\text{YZrO}_2$ . a)  $0^\circ$  projections from 35 tilt series. b) Cross-sections extracted from some of the volumes, showing the selected part of the soot in good contact with the  $\text{YZrO}_2$  which volume changes were followed. c) 3D models at time 0 at  $400^\circ\text{C}$ ,  $475^\circ\text{C}$ ,  $550^\circ\text{C}$  and  $600^\circ\text{C}$  showing the soot in yellow and the support in blue. The region of interest, of which volume change was followed (see b)) is better observable in the models. d) Arrhenius plot showing a linear relation between the burning speed of the soot in contact with the support and the inverse of the temperature.

quantify the combustion process of soot and to estimate its activation energy when the soot is in contact with a catalyst such as  $\text{YZrO}_2$ , knowing that without any catalyst the burning temperature is around  $680^\circ\text{C}$  and in the presence of  $\text{YZrO}_2$ , it is around  $520^\circ\text{C}$ . The sample was set on a heating chip compatible with a [DensSolutions Wildfire holder](https://denssolutions.com/products/wildfire/)<sup>viii</sup>. The sample was heated under 1.7 mbar of  $\text{O}_2$ . The irradiation test was performed at  $300^\circ\text{C}$  for 5 minutes during which the sample received an electron dose of  $1.68 \cdot 10^6 \text{ e}^- / \text{nm}^2$  at an electron flux of  $5,600 \text{ e}^- / \text{nm}^2 \cdot \text{s}$ . During that time, no visible damage was observed. The tilt series were recorded using SBSET (130 s), and a tilt series was recorded every 5 min. In total, 35 tilt series were recorded in less than 3h. Figure 14 a) shows the  $0^\circ$  projections extracted from the 35 tilt series recorded at  $400^\circ\text{C}$ ,  $425^\circ\text{C}$ ,  $450^\circ\text{C}$ ,  $475^\circ\text{C}$ ,  $525^\circ\text{C}$ ,  $550^\circ\text{C}$  and  $600^\circ\text{C}$  under 1.7 mbar of  $\text{O}_2$ .

To quantify the burning speed, the soot in contact with the support was followed with time (region of interest indicated in Figure 14 b)). By quantifying its volume change, it was possible to draw an Arrhenius plot. The activation energy of the soot combustion in contact with  $\text{YZrO}_2$  was found to be around 128 kJ/mol, close to the values proposed in the literature<sup>55,56</sup>.

To prove that the soot in contact with the catalysis is consumed faster, the volume change of contact-free soot was followed at different temperatures with time (Figure 15). Of course, due to the soot unresolved porosity, its real volume cannot be quantified accurately because it can be consumed in every direction. However, the soot volume change was normalized on the cross-sections in nm/s and compared with that of the soot in contact with  $\text{YZrO}_2$ . The plot shown in Figure 15 c) clearly shows that the soot in contact with  $\text{YZrO}_2$  is consumed faster than the soot that is not in contact with the catalyst. Such findings are only available by having access to the 3D information during an *operando* experiment. Of course, it may be argued that electron tomography is not necessary and it is sufficient to search a sample where the soot is visibly in contact with the catalyst and follow its combustion in 2D. Indeed, it could be much easier and eventually faster (data analysis needed 6 months). However, it must be reminded that in TEM the focus is made in the full depth of the thin sample. Under these conditions, a sample of thickness equal to several hundreds of nanometers and having very complicated morphology will be complicated to analyze. Therefore, performing an *operando* experiment following only 2D projections of a 3D complicated structure will always have a shadow of doubt and the good contact between the soot and the catalyst can be confirmed only by tilting the sample and analyzing its reconstructed volume.

---

<sup>viii</sup> <https://denssolutions.com/products/wildfire/>



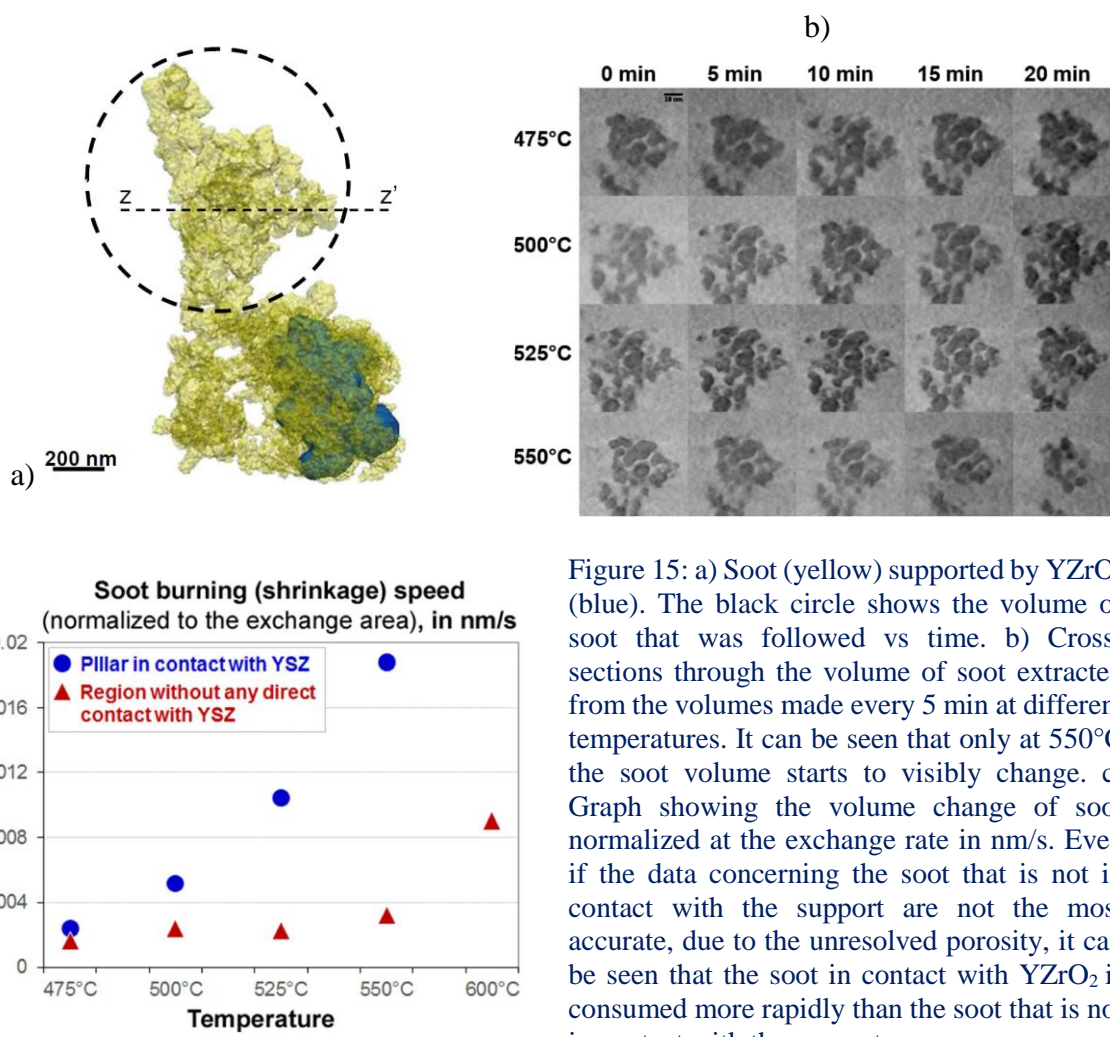


Figure 15: a) Soot (yellow) supported by  $\text{YZrO}_2$  (blue). The black circle shows the volume of soot that was followed vs time. b) Cross-sections through the volume of soot extracted from the volumes made every 5 min at different temperatures. It can be seen that only at  $550^\circ\text{C}$  the soot volume starts to visibly change. c) Graph showing the volume change of soot normalized at the exchange rate in nm/s. Even if the data concerning the soot that is not in contact with the support are not the most accurate, due to the unresolved porosity, it can be seen that the soot in contact with  $\text{YZrO}_2$  is consumed more rapidly than the soot that is not in contact with the support.

The data acquired during the *operando* experiments were processed using the SIRT-FISTA-TV reconstruction algorithm (see the development in section 2.1.3).

Figure 16 a) shows the  $0^\circ$  tilt projection used for the volume reconstruction. In Figure 16 b) and c), two cross-sections parallel to the XY plane are compared. They were extracted from the volumes calculated with SIRT and SIRT-FISTA-TV, respectively. It can be seen that the image obtained with SIRT-FISTA-TV is less noisy. Only three grey levels are present. They correspond to the support (dark grey), the soot (medium grey) and the vacuum (light grey). The small black dots that are Au nanoparticles used for image alignment. Here it must be pointed out that in Figure 16 a) (where is displayed one of the projections), the Ag nanoparticles are not sharp. In fact, due to the fast rotation (around  $28^\circ/\text{s}$ ) even the sharpest projections are affected by noise and by translational and rotational blur. However, even using such **real and non-perfect data**, the components, which are light (soot) and heavy (support) are well distinguished<sup>46</sup>.

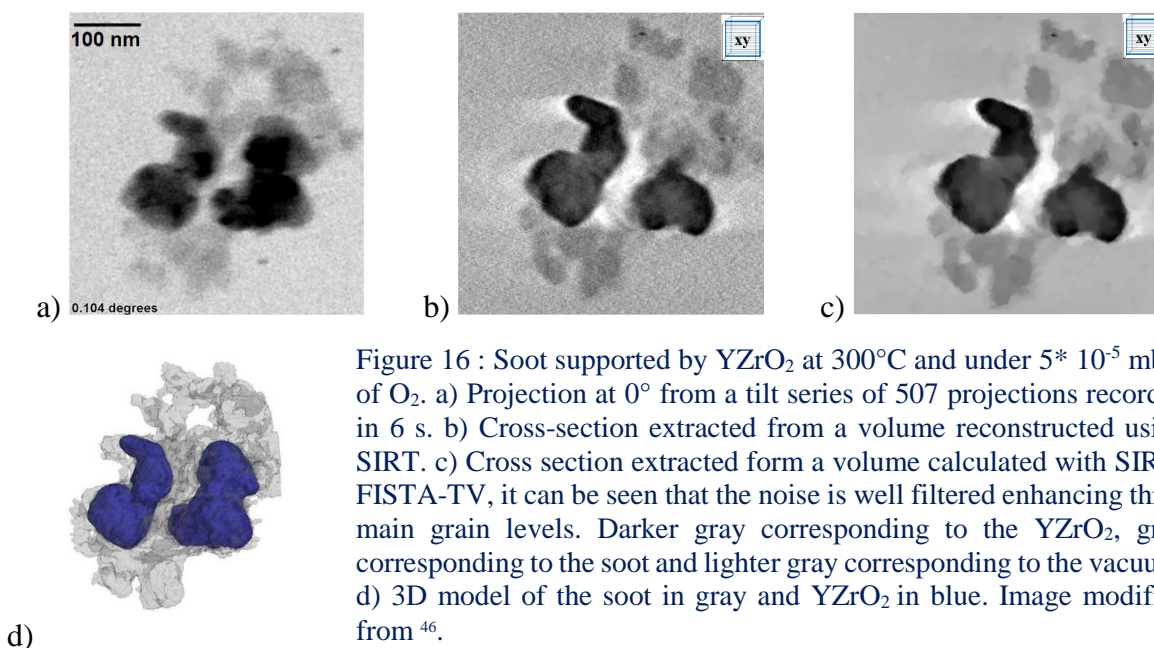


Figure 16 : Soot supported by YZrO<sub>2</sub> at 300°C and under  $5 \cdot 10^{-5}$  mbar of O<sub>2</sub>. a) Projection at 0° from a tilt series of 507 projections recorded in 6 s. b) Cross-section extracted from a volume reconstructed using SIRT. c) Cross section extracted from a volume calculated with SIRT-FISTA-TV, it can be seen that the noise is well filtered enhancing three main grain levels. Darker gray corresponding to the YZrO<sub>2</sub>, gray corresponding to the soot and lighter gray corresponding to the vacuum. d) 3D model of the soot in gray and YZrO<sub>2</sub> in blue. Image modified from <sup>46</sup>.

### 3.1.2 3D calcination of Ag nanoparticles enclosed in hollow silicalite – 1

In section 2.1.2, Figure 7, the fast imaging recording while continuously rotating the sample was exemplified using a sample of Ag enclosed in silicalite-1 cages. Such type of sample is used in selective catalysis. While Ag is trapped inside silicalite-1, it interacts only with the molecules that have a size small enough to penetrate the silica pores. Therefore, to reach its desired activity, all the Ag nanoparticles must be contained inside the silica<sup>36,37</sup>. This project was made in cooperation with the group of David Farrusseng from IRCE Lyon (CNRS, Université Lyon 1).

First, the samples were studied in vacuum using both STEM and BF modes at high resolution (Figure 17 a), b), c)). The CRRET method was also used to record tilted images for 3D analysis (Figure 17 d),e),f)). Those experiments were performed using an UltraScan 2K from Gatan, with a goniometer rotation speed of about 0.5 °/s. At the beginning, the blur values indicated in the Table 1 were only a theoretical point of view regarding the feasibility of the continuous rotation and recording of the tilt series. But, this experiment showed that the CRRET method could be applied on a larger scale despite the limited recording speed of the camera. In this case, the image was captured using the free software [Camstudio V.2.0](https://camstudio.org/)<sup>ix</sup>. At this point, it is important mentioning that the recorded tilt series contain several thousands of images due to continuous rotating and recording of the images at a high rate. Among the recorded images, several ones

<sup>ix</sup> <https://camstudio.org/>

are blurred due to mechanical vibrations of the goniometer or due to the user who corrects live the position and the focus of the object. However, inside the stack, some images are sharp and can be used for an alignment and the volume reconstruction of the sample. In this example, 328 images were manually selected out of 1584. After volume reconstruction and data segmentation, 56 Ag nanoparticles were detected, with an average size of 6.1 nm with a standard deviation of 2.5 nm. It was found that 2 of them are outside the silicalite-1 cage (3.5%).

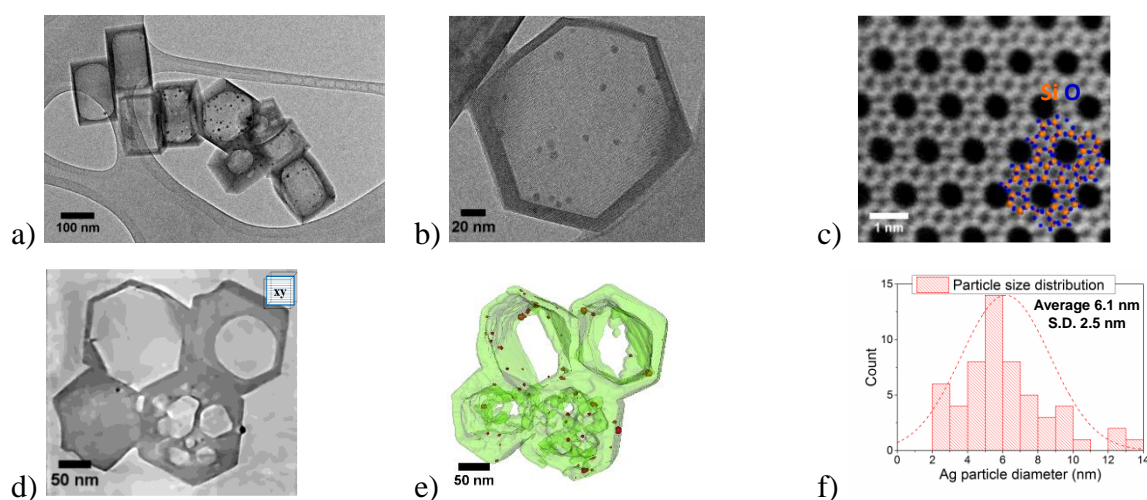


Figure 17 : Ag nanoparticles enclosed in silicalite-1 a) et b) BF images showing the morphologies of the silica boxes. c) HR-STEM image showing the crystallographic structure of silicalite-1. The Si atoms are in orange and the O atoms in blue (credits to Dr. Mimoun Auine, IRCE Lyon). d) Cross-section through the volume reconstructed using a tilt series recorded using the CRRET method within 226 s. e) 3D model of the silica in green, with the Ag nanoparticles in red. In this model the top and bottom walls are not modeled due to their 3 nm thickness that is in the limit of the spatial resolution. f) Ag particles size distribution having an average size of 6.1 nm and a standard deviation of 2.5 nm. Image modified from <sup>57</sup>.

The sample shown in Figure 17 should have a good catalytic activity, because the majority of the nanoparticles are inside the cage. However, the sample after the calcination does not have the expected behavior. The catalytic activity is characteristic of a catalyst for which the Ag nanoparticles are outside the box. To understand what happens during the calcination process 3D *operando* experiments were carried out.

The CRRET image recording method was employed in ETEM under 1.8 mbar of O<sub>2</sub> in order to understand the changes undergone by the Ag nanoparticles encaged in hollow silica during the calcination process. The same sample was studied at 20°C under vacuum and at 280°C and 450°C under 1.8 mbar of O<sub>2</sub> (Figure 18).

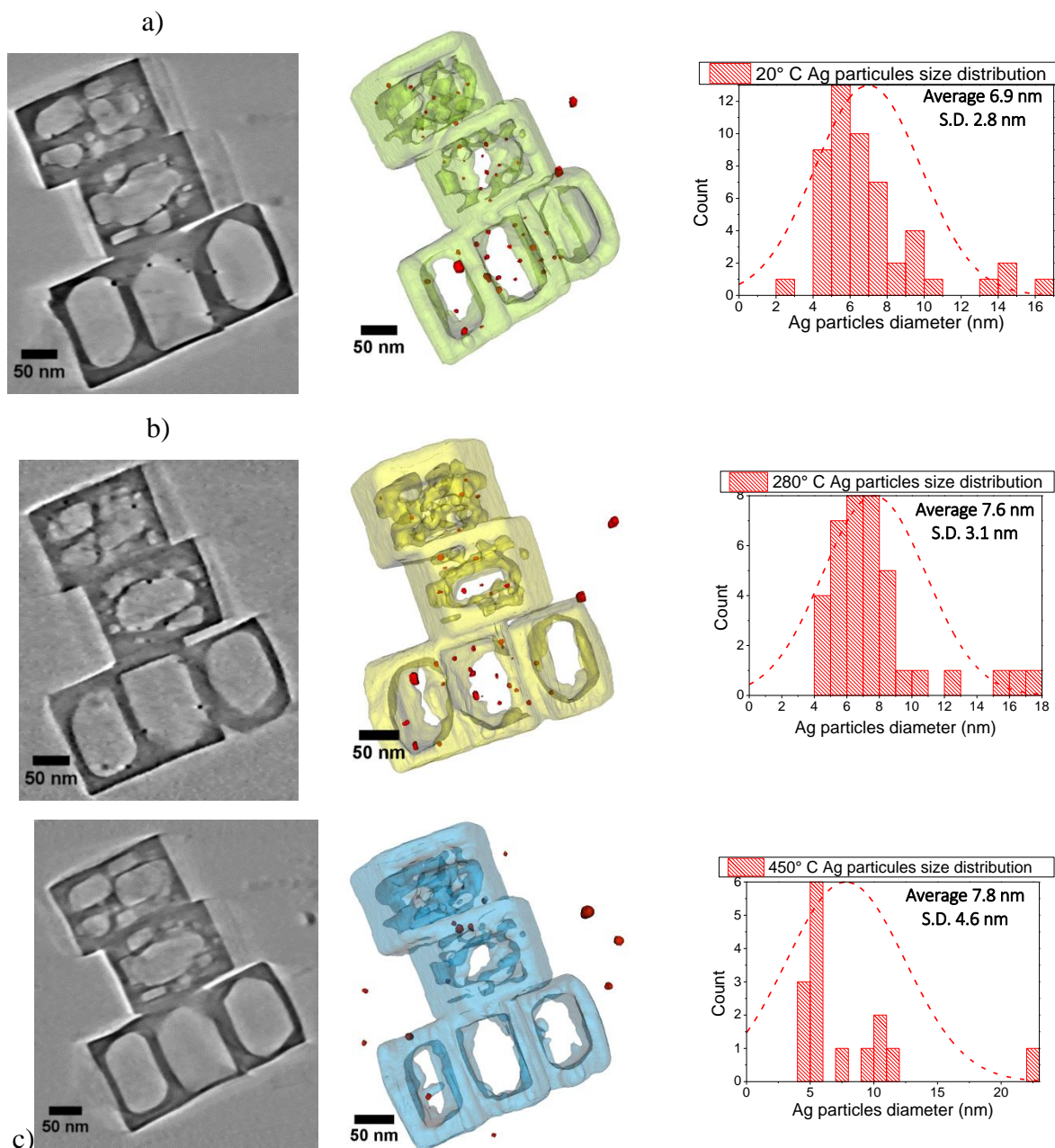


Figure 18 : Electron tomography performed during an *operando* calcination study of the same population of silicalite-1 hollow zeolites containing Ag NPs at a) 20°C under high vacuum, b) 280°C and c) 450°C under a 1.8 mbar of O<sub>2</sub>. The left side shows cross-sections extracted from the XY plane of the reconstructed volumes. The central column displays the reconstructed models of the hollow silicalite-1 crystals with the zeolite in green, yellow and blue at 20°C, 280°C and 450°C, respectively, and Ag NPs in red. The column on the right displays the corresponding Ag particle size distributions. Average sizes are 6.9 nm, 7.6 nm and 7.8 nm at 20°C, 280°C and 450°C, respectively, with respective standard deviations of 2.8 nm, 3.1 nm and 4.6 nm. Image modified from <sup>57</sup>.

At 20° C, only 6% of the Ag nanoparticles were detected outside the boxes (3 nanoparticles out of 51). Their average size was about 6.9 nm. At 280°C, the average size increased to 7.6 nm. Due to coalescence and Ostwald ripening, their number decreased down to 38 Ag nanoparticles, however the total volume of Ag was preserved. At 450°C, the silicalite-1 pores opened due to

the temperature and the Ag nanoparticles started interacting with O<sub>2</sub> to form AgO<sub>x</sub>. At 450°C, AgO<sub>x</sub> is not stable and decomposes into Ag metal but outside the silica cage. The loss of selectivity of the catalyst after the calcination process could be explained only after such 3D *operando* experiment showing that the sample synthesis procedure should be reconsidered. Once the Ag nanoparticles were outside the cage (Figure 19), O<sub>2</sub> was dissociated by Ag and interacted with the carbon membrane, making the Ag particles move and eat the membrane.

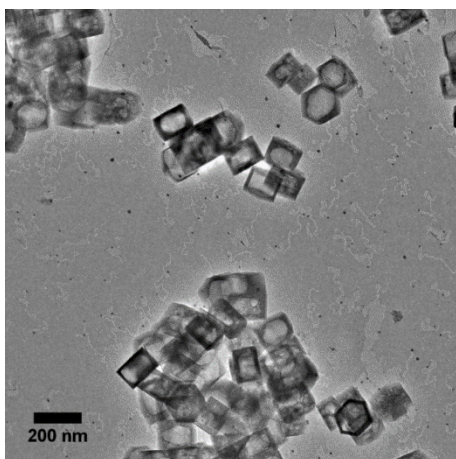


Figure 19: Ag nanoparticles and silicalite-1 cages after been heated at 450° under 0.1 mbar O<sub>2</sub>. The Ag nanoparticles leave marks in the carbon membrane after O<sub>2</sub> is dissociated over their surface and interacts with the carbon membrane. Credits to Dr. Thierry Épicier and Dr. Francisco J. Cadete Santos Aires. Image modified from <sup>57</sup>.

From a technical point of view, for the *operando* calcination study, the sample was heated using the Gatan furnace heating holder that has a limited tilt range due to its important size. Therefore, the sample was tilted only between -25° and +42° during 120 seconds. 458, 416 and 460 images were recorded with a camera exposure time of 0.14 s. From those images, only 281, 210 and 219 images were respectively retained for the volume reconstruction. At this point it must be mentioned that, by continuously recording images even in a short angular interval and at a relatively low rate, the tilt series can contain a high number of images. By using high rate cameras, the tilt series can be formed by several thousands of images and can represent several gigabits of data. Such files are difficult to manipulate using regular computers.

This study showed that even if the tilting capacity of the sample holder was limited, it was possible to segment and to quantify in 3D the reconstructed volumes. The phenomenon occurring during the calcination process were visualized and could explain the deactivation of the catalyst during its synthesis<sup>57</sup>.

### 3.1.3 3D sintering resistant Pd @SiO<sub>2</sub> core-shell nanoparticles

In the description of the fast tilt series recording method using continuous rotation and recording (CRR) (section 2.1.2), it was mentioned that the recording of a full tilt series from 72° to -71°

could be performed in several seconds. In this section, I would like to highlight the fact that it is possible to record a tilt series in a few seconds. This is exemplified with an *operando* experiment consisting in the calcination and the reduction of Pd particles in the core of a silica shell. Such system, where the catalyst is enclosed in its support, is designed to prevent the sintering of the Pd particles when used in catalytic activities at high temperature. The project was made in cooperation with Dr. Anne-Sophie Gay from IFPEN. The acquisition of the tilt series was made using a DensSolution sample holder that can heat the sample while being tilted at high angles thanks to its microelectromechanical systems (MEMS). I will show tilt series recorded in 6 s, 8 s and 7 seconds.

The maximum cumulative electron dose that could be received by the sample was measured equal to  $4 \cdot 10^6 \text{ e}^-/\text{nm}^2$ . The electron flux was set to  $9.3 \cdot 10^4 \text{ e}^-/\text{nm}^2\text{s}$ , permitting an acceptable dose, despite a rather low signal-to-noise ratio recorded in the projections. 7 tilt series could be recorded on the same area heated from  $20^\circ\text{C}$  to  $400^\circ\text{C}$  and  $500^\circ\text{C}$  under 4 mbar of  $\text{H}_2$ , for a total cumulative electron dose of  $1.5 \cdot 10^6 \text{ e}^-/\text{nm}^2$ . At the first sight, the electron flux seems relatively high. However, it must be mentioned that a compromise between the speed of the tilt, the recording rate of the camera and the electron flux must be found in order to record a satisfying signal-to-noise ratio in the tilt series. Of course, low electron fluxes can be used while the rotation speed of the sample as well as the recording rate of the camera are low, but while the rotation speed and the recording rate are high, *i.e.* for very short exposure times of the camera, it will be recommended to use a slightly higher electron flux during the experiment in order to have some signal recorded in the tilt series.

For the experiment, the images were recorded using the OneView camera from Gatan set at a rate of 100 frames/s. The sample was rotated at a speed of about  $26^\circ/\text{s}$ . Every recorded tilt series had around 550  $2\text{k} \times 2\text{k}$  images with a pixel size, along the X direction, of about 0.52 nm. The estimated rotation blur, according to Table 1, was around  $0.26^\circ/\text{frame}$ .

For the volume reconstruction, only 1 out of 4 images were considered. Then after alignment, the volume was reconstructed using SIRT-FISTA-TV<sup>46</sup> (principles explained in the section 2.1.3). The data analysis revealed that at high temperatures, the Pd particles loose faceting and become more spherical with time. They also start to merge. However, we must consider that silica prevents the Pd particles from merging through both coalescence and Ostwald ripening<sup>35</sup> (Figure 20).

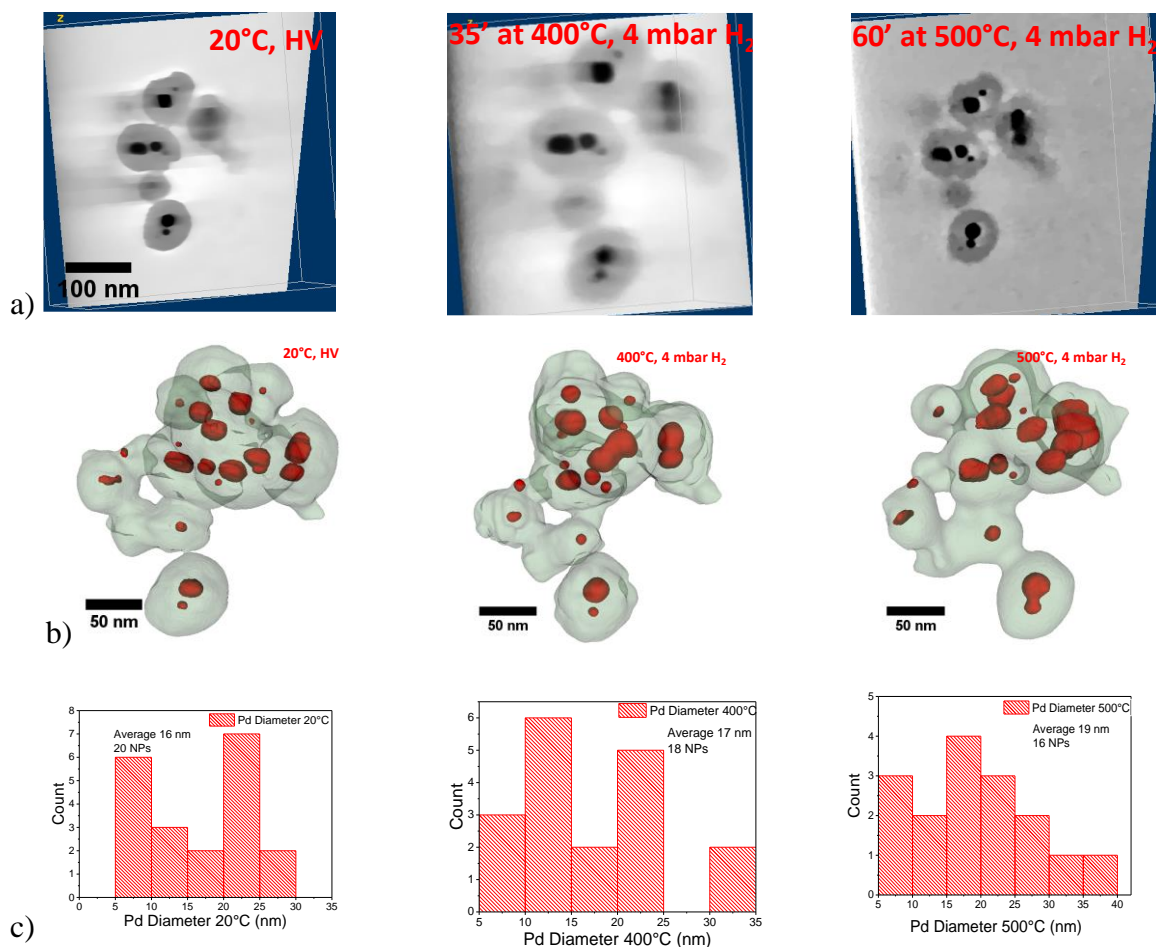


Figure 20: Pd core nanoparticles enclosed in a silica shell followed in *operando* mode at 20°C in high vacuum, 400°C and 500°C under 4 mbar of H<sub>2</sub>. The tilt series were recorded in 6 s, 8 s and 7s, respectively. a) Oriented cross-sections with the same orientation of the particles, in order to show the morphologic changes of the Pd nanoparticles. b) 3D models where Pd nanoparticles are in red and the silica is in green. It can be seen that the Pd nanoparticles are becoming more spherical while the temperature is increased. c) Particles size distribution. The average particle size increases with time due to coalescence. However, the silica shell prevents a fast growth of the particles. Image modified from <sup>35</sup>.

### 3.2 *Operando* electron microscopy combined with *post-mortem* electron tomography

The title of the section was chosen because sometimes being fast is not sufficient. At the beginning of the section 3, it was told that *operando* should be always compared with experiments performed in classical way, by using techniques that are accepted by the scientific community. That way, I think that it is safer to combine live *operando* experiments with *post-mortem* analysis<sup>58</sup>. Such approach should first confirm that the environmental conditions under which the *operando* experiments are performed into the environmental electron microscope is

in good agreement with the designed purpose, and, secondly and most importantly, the observed phenomena can explain the behavior of the sample in that given environment.

In this section I will summarize some *in situ* experiments that are combined with the electron tomography analyses performed *post mortem*.

### 3.2.1 2D *in situ* growth of metal nanoparticles on the surface of a perovskite

Different methods<sup>59</sup> are used to deposit the active phase of a catalyst on its support, such as silica, alumina, titania, ceria etc. However, despite the synthesis and activation process, the supported particles are ending coalescing or covered in reactive exhaust such as carbon that lead to the deactivation of the catalyst. To prevent the particle movement, a solution is to anchor them to the support. To do that, the metallic ions can be dispersed within the crystal lattice of an oxide support and form particle through a redox-exolution<sup>60,61</sup>. The example given here deals with the *in situ* growth of metallic nanoparticles. This study was carried out in cooperation with Dr. Dragos Neagu from University of Strathclyde and Dr. Mihalis Tsampas from Duch Institute of Fundamental Energy Research, and was supported by METSA.

Ni nanoparticles were formed by heating a perovskite support at 600 °C and 900 °C under vacuum and under 20 mbar of H<sub>2</sub>. First, the Ni ions were dispersed in two different perovskites: La<sub>0.43</sub>Ca<sub>0.37</sub>Ni<sub>0.06</sub>Ti<sub>0.94</sub>O<sub>3</sub> and La<sub>0.8</sub>Ce<sub>0.1</sub>Ni<sub>0.4</sub>Ti<sub>0.6</sub>O<sub>3</sub>. The La<sub>0.43</sub>Ca<sub>0.37</sub>Ni<sub>0.06</sub>Ti<sub>0.94</sub>O<sub>3</sub> sample, with a low concentration of Ni, was diluted in alcohol and then deposited on a MEMS chip compatible with the DensSolutions sample holder. Figure 21 a) shows the growth of Ni nanoparticles with time, while the sample was heated at 900°C under 20 mbars of H<sub>2</sub>.

The Ni particles growth was observed and quantified for various times. It was shown that the rate of the particles growth is limited by the concentration of exsolvable Ni ions and by the perovskite strain around the particle. During the experiment, the particles were not moving even at 900°C, indicating that the particles were strongly attached to the support.

The second studied sample was La<sub>0.8</sub>Ce<sub>0.1</sub>Ni<sub>0.4</sub>Ti<sub>0.6</sub>O<sub>3</sub>, characterized by a higher concentration of Ni. In the previous experiment, the sample was as a powder, therefore locating and following the particles with time at high temperature and at high resolution was a hard task because the grains could rotate or move. In this second experiment, the sample was made of a thin foil prepared by Focused Ion Beam (FIB). The regions of interest A1 and A2 are shown in Figure 21 b). The sample was heated at 650°C under 20 mbar of H<sub>2</sub>. By having a stable sample, it was



possible to follow the particle growth at different stages. This allowed us to model the nucleation of particles on the perovskite surface.

At high gas pressure of H<sub>2</sub>, the atomic resolution is difficult to achieve. Therefore, the La<sub>0.43</sub>Ca<sub>0.37</sub>Ni<sub>0.06</sub>Ti<sub>0.94</sub>O<sub>3</sub> sample was also heated at 900°C under high vacuum. Figure 21 c) and d) show the Ni particle growth from the nucleation of the particle until its final size reached after 7 minutes. Performing the experiment at atomic resolution enabled the observation of the epitaxial growth that enhances the particles stability on the surface. It was also possible this way to propose a model based on Ni<sup>+</sup> diffusion through the perovskite matrix.

This work highlights the fact that the environmental electron microscopy at atomic resolution can provide a full insight on nucleation and growth of exsolved particles<sup>62</sup>. Such information that is difficult to obtain using other techniques. The findings allowed us to model the atomic path of the Ni ions through the perovskite matrix towards its surface.

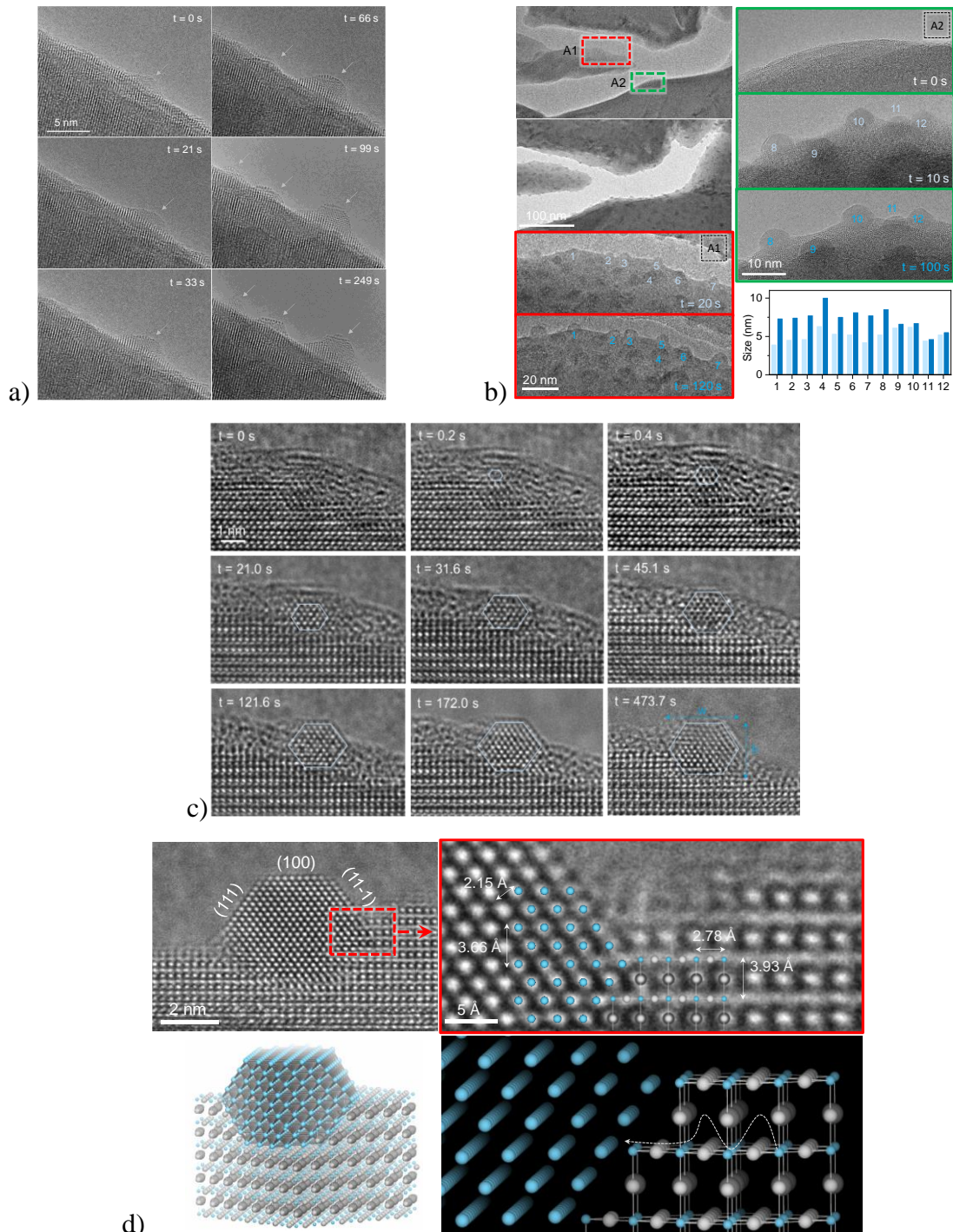


Figure 21: Metal nanoparticles growth on a perovskite support. a) Nanoparticle growth on  $\text{La}_{0.43}\text{Ca}_{0.37}\text{Ni}_{0.06}\text{Ti}_{0.94}\text{O}_3$  followed with time at  $900^\circ\text{C}$  under 20 mbar of  $\text{H}_2$ . b) Sample of  $\text{La}_{0.8}\text{Ce}_{0.1}\text{Ni}_{0.4}\text{Ti}_{0.6}\text{O}_3$  prepared as a thin lamella by Focused Ion Beam (FIB), heated under 20 mbar of  $\text{H}_2$  at  $650^\circ\text{C}$ . The red and green rectangles indicate the regions where the growth of the particles was followed. The histogram shows the size of highlighted particles. Those followed during the early stage are shown in light blue whereas those at a later growth stage are shown in blue. c) Direct *in situ* observation of the Ni particles exsolution at the surface of  $\text{La}_{0.8}\text{Ce}_{0.1}\text{Ni}_{0.4}\text{Ti}_{0.6}\text{O}_3$  at  $900^\circ\text{C}$  under vacuum. d) Ni nanoparticle grown on  $\text{La}_{0.43}\text{Ca}_{0.37}\text{Ni}_{0.06}\text{Ti}_{0.94}\text{O}_3$  under vacuum at  $900^\circ\text{C}$ . The interface between the Ni with the perovskite can be observed. The 3D model explains the crystallographic position with a highlight on the  $\text{Ni}^+$  diffusion within the perovskite matrix represented by the dashed sinusoidal arrow. Credits to Dr. Dragoş Neagu. Image modified from <sup>62</sup>.

### 3.2.2 Genesis of Pd nanoparticles supported by $\delta$ and $\alpha$ - $\text{Al}_2\text{O}_3$

Siddadha Koneti's PhD thesis was not only dedicated to the development and application of fast image recording for electron tomography. In cooperation with Amandine Cabiac, Dr. Priscilla Avenier and Dr. Anne-Sophie Gay from IFPEN Siddardha also studied the genesis of Pd nanoparticles supported on  $\alpha$ - and  $\delta$ - $\text{Al}_2\text{O}_3$ . In this document I will not give all the experimental details of the study that are well explained in [Siddardha's thesis](#), I will only highlight some conclusions of our work. The goal of this fundamental study was to better understand the genesis of one of the most used catalyst in industrial applications.

The synthesis of colloidal Pd nanoparticles, with sizes less than 5 nm, supported on  $\text{Al}_2\text{O}_3$  mainly consists in 4 steps. The first one is the impregnation of the support with Pd colloids. Then, the samples are dried in air at atmospheric pressure at 125°C for 2h. The third step is the calcination in air at 425°C for 2h. During those last two steps, the size of the Pd particles is increased. The last step is a reduction process under  $\text{H}_2$  at 150°C, during which metal Pd particles are obtained (Figure 22).

A small amount of sample was collected at each synthesis step and the samples were analyzed *post mortem* in a so-called "classical way". At every stage, the Pd particle sizes were assessed. Of course, as expected, the average size of the particles increased from the impregnated state to the calcined state from 2.3 nm (IMPR), 2.7 nm (DRIE) and 3.5 nm (CALC) respectively, with standard deviations of 0.45 nm, 0.55 nm and 0.74 nm respectively. STEM electron tomography was performed on the calcined state and it was confirmed that the Pd particles are homogeneously distributed over the sample. Their mean size was measured as 3.5 nm (Figure 23). Those findings were completed with high resolution images that showed that the supported particles are  $\text{PdO}_x$  different species.

To better understand and reveal the Pd particles evolution, the calcination and the reduction steps were performed *in situ*. The impregnated sample was dried at 120°C, calcined at 450°C under air or  $\text{O}_2$  at different pressures and then reduced at 150°C under 11 mbar of  $\text{H}_2$ . During the *in situ* analysis, the same region was followed with time in order to quantify the process that occurs during the particles growth, *i.e.* Ostwald ripening and coalescence. When supported by  $\delta$ - $\text{Al}_2\text{O}_3$ , Ostwald ripening was dominant between under 10 mbar of  $\text{O}_2$  150°C and 450°C. However, some coalescence phenomena also occurred despite the fact that  $\delta$ - $\text{Al}_2\text{O}_3$  provided many anchoring sites to the particles<sup>63</sup>.

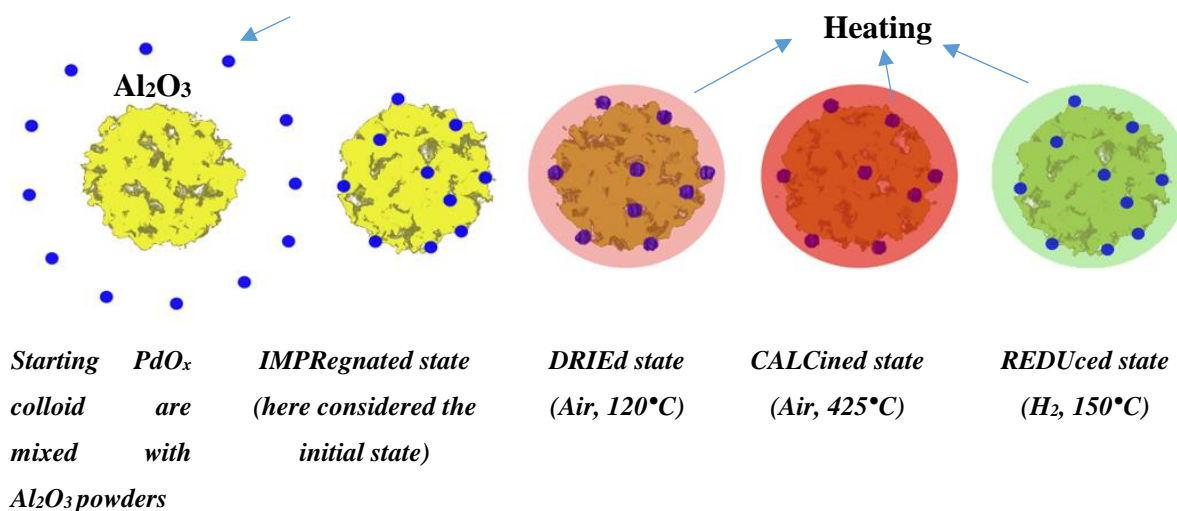


Figure 22: Schematical representation of the steps needed to synthesize Pd colloidal nanoparticles grafted on  $\alpha$ - and  $\delta$ -Al<sub>2</sub>O<sub>3</sub>. The process has 4 steps (shown from left to right): IMPregnated, DRIded, CALCined and REDUced states. Image modified from <sup>64</sup>. Credits to Dr. Siddardha Koneti.

Concerning the crystallography during the calcination process, different PdO<sub>x</sub> compounds were found as expected, but in some cases metallic Pd was also found. However, finding metallic Pd cannot be considered as conclusive because the electron beam can be a potential reducing agent that can easily reduce the small sized PdO<sub>x</sub> particles that can be relatively instable<sup>65</sup> at low partial pressures of O<sub>2</sub>. As done for the *post mortem* study, the Pd particle sizes were quantified during the *in situ* calcination process. Figure 24 a) compares the Pd particle sizes measured during the *in situ* experiments with those obtained *post-mortem*. A good agreement is found when the imaging was performed in STEM mode. Figure 24 b) shows only the measurements made during the *in situ* experiments. The average of the measurements made in the STEM mode are compared with those performed in the TEM mode (the thick red line represents the measurement uncertainty). From the figure, it can be concluded that the TEM imaging mode can influence the particle growth, attributed to a negative influence of the electron beam.

During the *in situ* experiment, the same region of the sample was observed. Therefore, by analyzing the time-lapsed displacements of the Pd particles, we measured the average speed of the particles over the support. In this document, I will expose only some results of the studies performed on Pd /  $\delta$ - Al<sub>2</sub>O<sub>3</sub>. I exclude the 3D analysis performed *in situ* where the movement of the particles were followed in 3D.

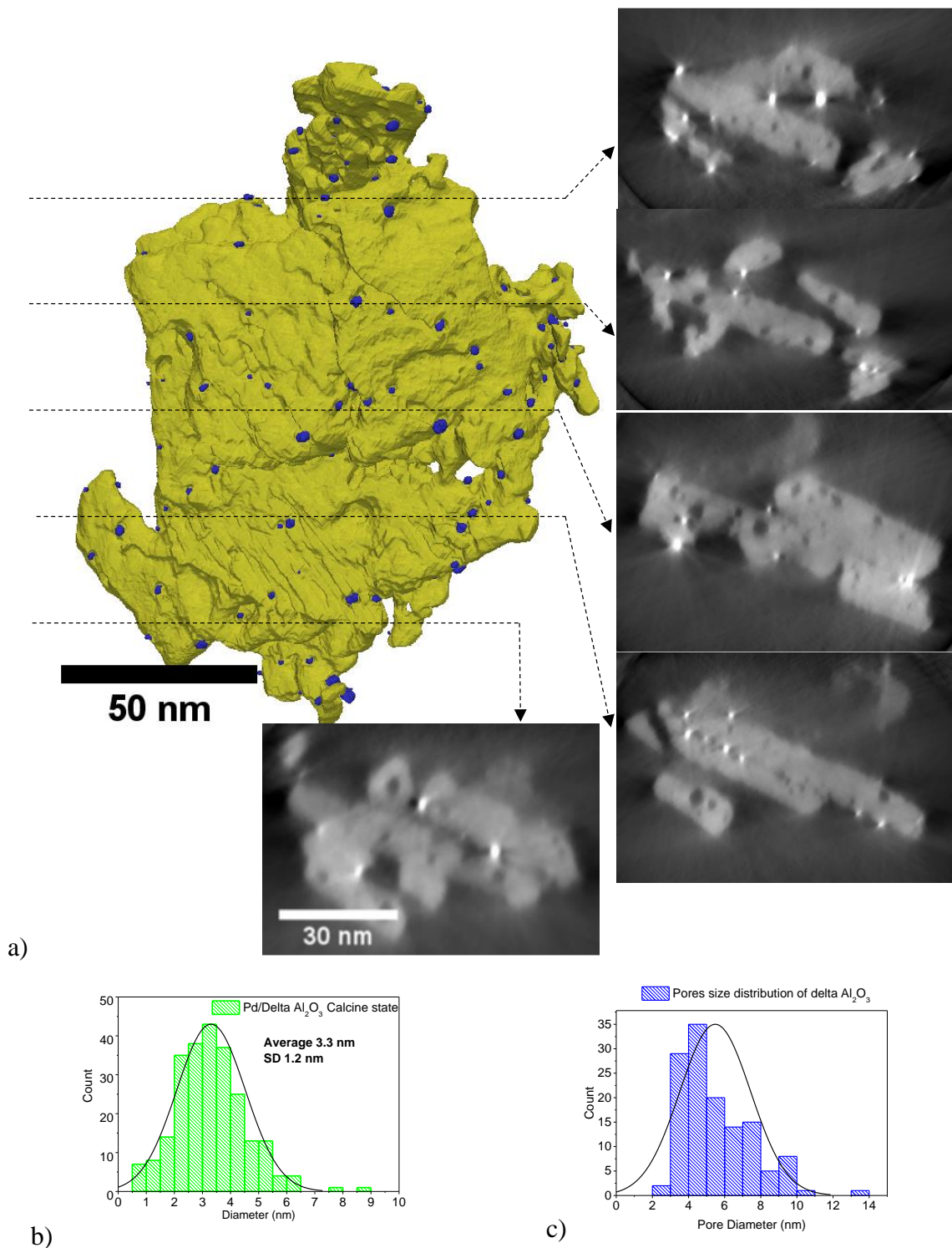


Figure 23: Colloidal Pd nanoparticles supported by  $\delta$ - $\text{Al}_2\text{O}_3$  after calcination at 425°C in air. a) STEM electron tomography reveals a homogenous distribution of Pd particles (in blue) over the support (in yellow). The cross-sections in XZ plane are extracted at the place marked by the dashed arrows. b) Pd particles size distribution. c) Pore size distribution of  $\text{Al}_2\text{O}_3$ .

Similar experiments were performed on Pd supported by  $\alpha$ - $\text{Al}_2\text{O}_3$ . All details can be found in Siddarda Koneti's thesis and in reference <sup>64</sup>.

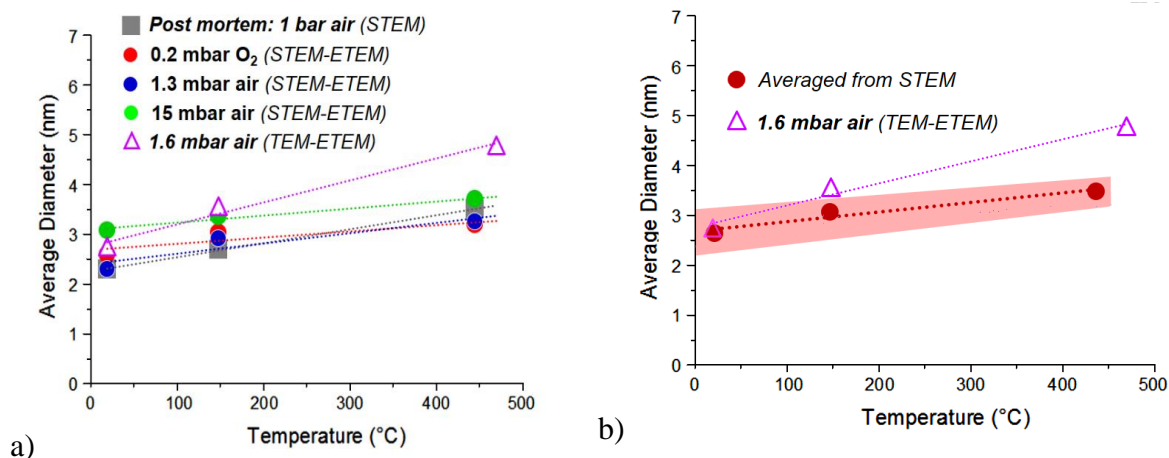


Figure 24: a) Pd particle size distribution under different gas pressures, measured *in situ* and compared with the particle size distribution measured *post mortem*. b) Average particle size measured using STEM imaging compared with measured obtained *in situ* using TEM imaging. The particle growth observed in TEM is attributed to a beam effect. The thick red line indicate the uncertainty on the measurements.

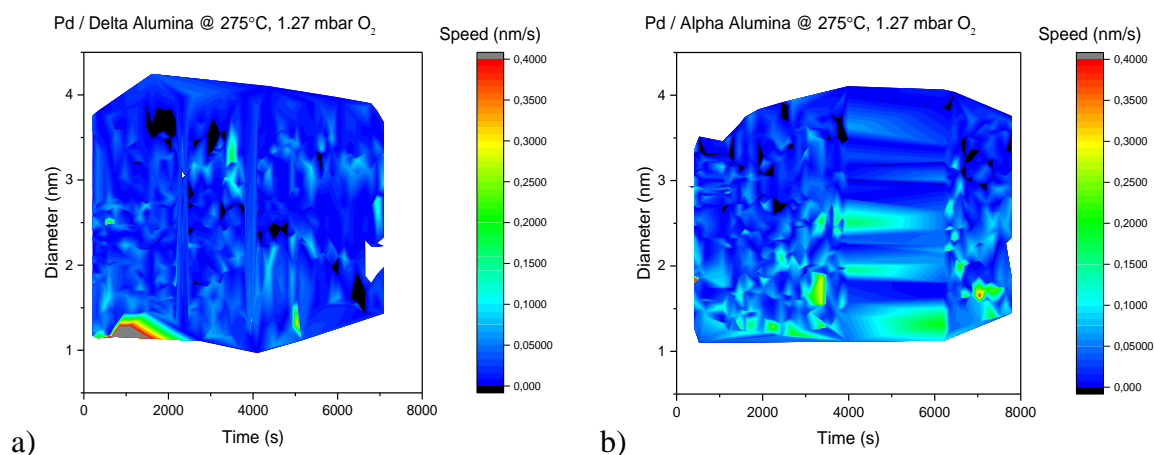


Figure 25: Colored maps showing the instantaneous speed of Pd nanoparticles as a function of their size on (a)  $\delta$ - $\text{Al}_2\text{O}_3$  and (b)  $\alpha$ - $\text{Al}_2\text{O}_3$ . The temperature look-up-table highlights the overall mobility of NPs on the  $\delta$  and  $\alpha$ -support. The small particles have a higher speed than the bigger ones and  $\alpha$ - $\text{Al}_2\text{O}_3$  allows a higher mobility of the particles on its surface than  $\delta$ - $\text{Al}_2\text{O}_3$ .

Figure 25 shows colored map representing the mobility of the Pd particles supported by  $\delta$ - $\text{Al}_2\text{O}_3$  compared with  $\alpha$ - $\text{Al}_2\text{O}_3$ . As expected, the Pd particles become less mobile when their size increases. Also, by comparing both supports,  $\delta$ - $\text{Al}_2\text{O}_3$  provides a higher specific surface area. Therefore, more anchorage sites can be found on its surface. This makes Pd nanoparticles less mobile than when they are supported by  $\alpha$ - $\text{Al}_2\text{O}_3$  that has many “flat surfaces”.

In this study, we combined “classical” *post-mortem* analyses with *in situ operando* experiments in 2D and 3D. The effect of the imaging mode was considered. It was found to influence the *in*

*situ* experiments in a way that is not always compatible with the real evolution of the studied sample in its “natural” environment.

### 3.2.3 Migration and growth of Ag nanoparticles supported by ZSM-5

The strategy described in the previous section was employed for the study of Ag nanoparticles supported by Zeolite Socony Mobil 5 (ZSM-5). *Post mortem* experiments were combined with *operando* electron microscopy to study the migration and the growth of Ag nanoparticles supported by ZSM-5. Such materials are used as an absorbent of pollutants such as xenon, as its concentration in the atmosphere is monitored in the framework of the Treaty on the Non-Proliferation of Nuclear Weapons. The study was made in cooperation with Dr. Arnaud Monpezat during his thesis directed by Dr. David Farrusseng from IRCE-Lyon in cooperation with Dr. Sylvain Topin from CEA. The goal was to better understand the deactivation mechanism of Ag supported by ZSM-5 while absorbing xenon in the presence of chloride compounds. I will not enter into the chemistry that involves that deactivation. The chemical processes are explained in reference <sup>66</sup>.

In this study, fast SBSET image recording was used in the BF-TEM mode. A fresh sample was analyzed *post-mortem* under vacuum at room temperature. A sample was degraded *ex situ* to visualize in 3D the initial and the final states of the sample, *i.e.* the Ag nanoparticle sizes and distribution. It is known that the zeolites are extremely beam-sensitive, and the electron dose estimation showed that we had to limit the experiments at  $3 \cdot 10^5 \pm 5 \cdot 10^4 \text{ e}^-/\text{nm}^2$  using the ETEM at 300 keV and the Gatan OneView camera. For the fresh zeolite sample, the tilt series was recorded from  $+74^\circ$  to  $-74^\circ$  in less than 2 min using an electron flux of  $200 \text{ e}^-/\text{nm}^2\text{s}$ , leading to a total electron dose of  $23,900 \text{ e}^-/\text{nm}^2$ . 75 4k x 4k tilt images were recorded, with one pixel representing 0.54 nm along the X axis. 69 images were chosen for volume reconstruction. For the degraded zeolite sample, a tilt series of 74 4k x 4k images was recorded in less than 2 min with an amplitude of  $146^\circ$  (from  $74^\circ$  to  $-72^\circ$ ) (a pixel represented 0.33 nm in X direction) at an electron flux of  $300 \text{ e}^-/\text{nm}^2\text{s}$ . For this tilt series, the total electron dose was of  $35,400 \text{ e}^-/\text{nm}^2$ .

Figure 26 shows cross-sections in the XY plane, and the 3D models with Ag in gray and the ZSM-5 in brown. For both samples, the particles sizes and the distances between the first order neighbors were measured. The Ag particles were initially homogeneously distributed on the surface of the support.

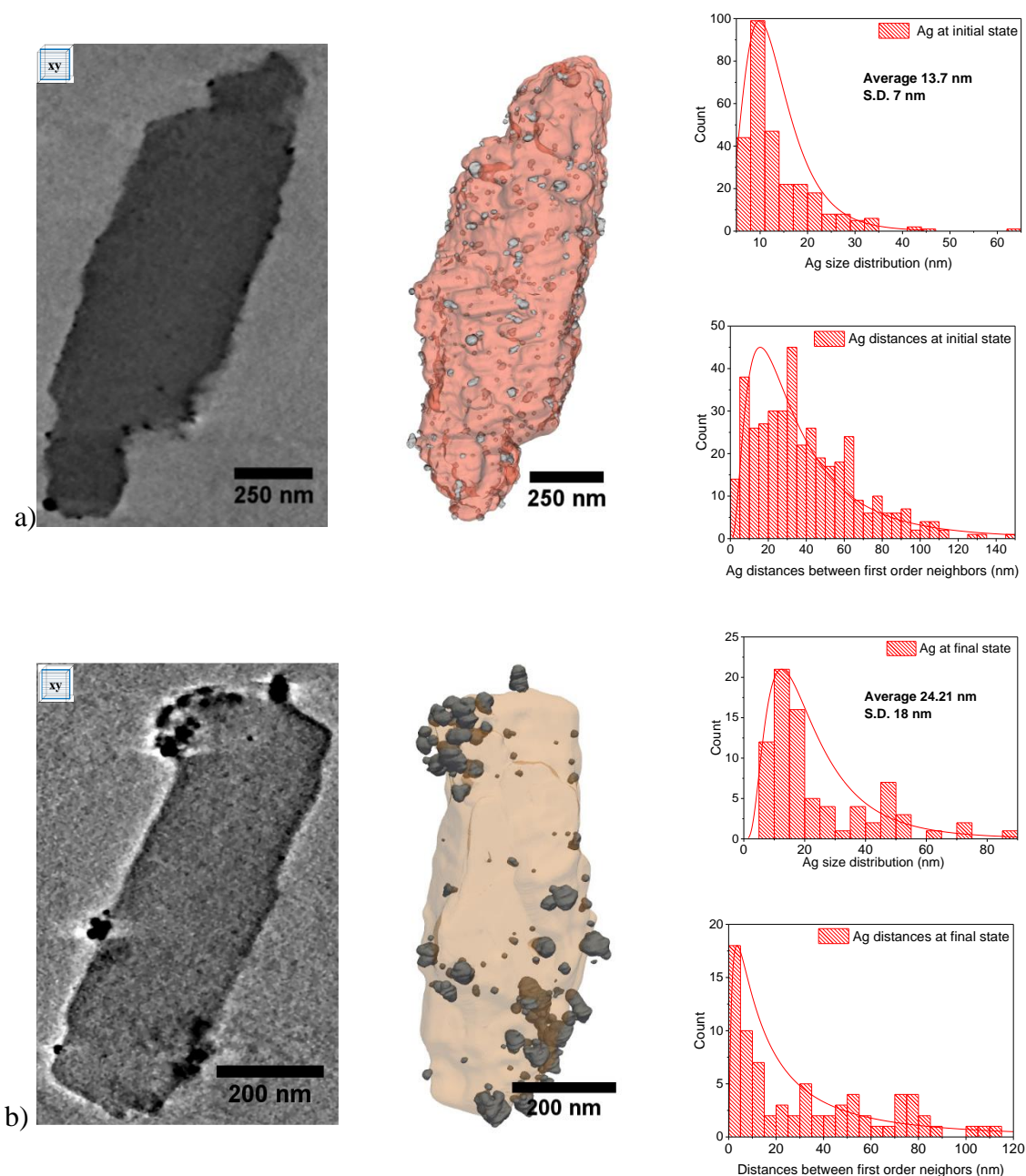


Figure 26: fast SBSET image recording at a very low dose on Ag nanoparticles supported by ZSM-5, analyzed *post-mortem*. a) Initial sample showing a uniform distribution of Ag particles on the surface of the zeolite. The Ag particles have an average size of 13 nm. b) Sample at the final state after having been exposed to chloride compounds. The Ag particles form big agglomerates of average size 24 nm. For both samples, the particles size distribution was measured as well as the distances between the first neighbors. Image modified from <sup>67</sup>.

The spatial resolution allowed the distinction of some particles inside the zeolite. The degraded sample was submitted to 70 adsorption processes under gas mixture containing chloride compounds such as: trichloromonofluoromethane, trichloroethane, tetrachloromethane and tetrachloroethylene during 10 weeks at room temperature. The adsorption processes were followed by desorption processes at 350°C.



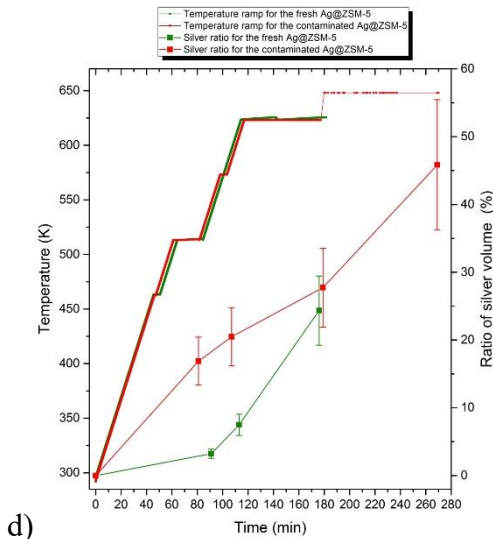
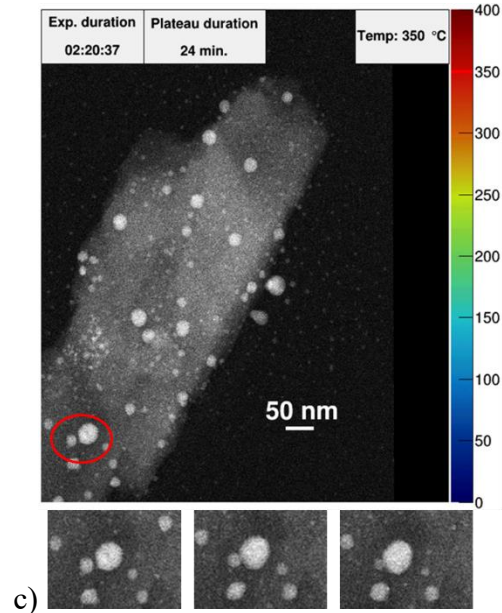
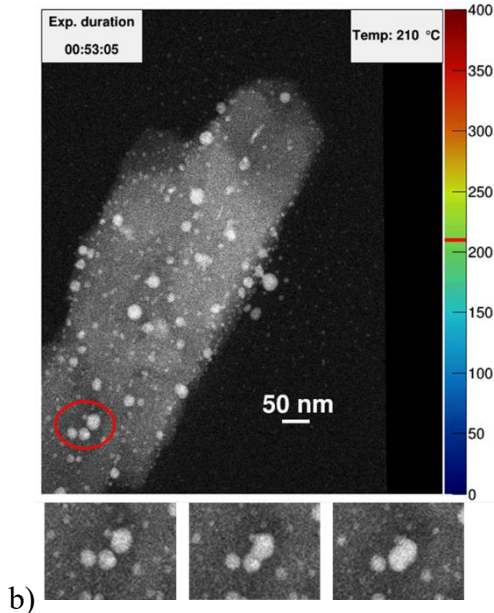
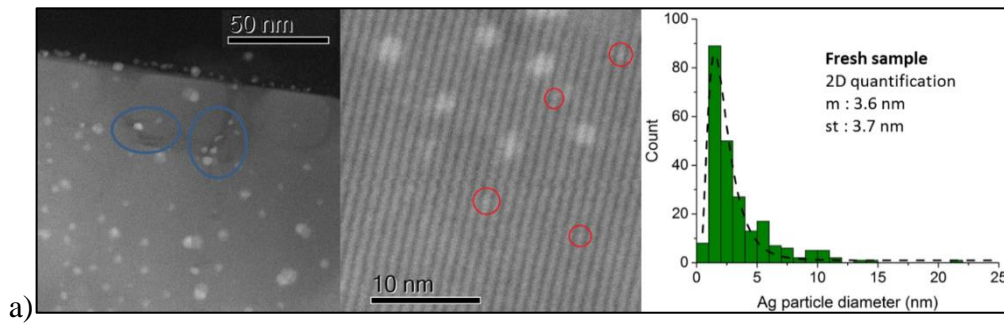


Figure 27: High resolution images of the fresh sample of Ag supported by ZSM-5. The particle size distribution of the Ag particles reveals an average size of 3.6 nm. The STEM images reveal that several nanoparticles are fixed on the surface of the zeolite as well as inside the bigger defects of the support. In the pores of the zeolite, Ag particles exhibit subnanometer sizes. b) and c) show images at different times extracted from the *in situ* experiment made on the degraded sample under 1 mbar a N<sub>2</sub>. At the beginning of the experiment, coalescence occurs. Once the Ag particles are big enough, Oswald ripening becomes dominant. d) Shows the temperature ramp and the particles growth, for the fresh sample in green, and for the degraded sample in red. The Ag growth is represented by the ratio between the Ag volume at a given time and the initial visible Ag volume. The Ag particles in the contaminated sample grow faster than those on the fresh sample. Credits to Arnaud Monpezat. Image modified from <sup>67</sup>.

The Ag nanoparticles formed big agglomerates in the degraded samples. This explained the loss of the adsorbent properties<sup>66,68</sup>.

To understand the phenomenon that occurs during the growth of Ag particles, *operando* electron microscopy in STEM mode was employed. The particles growth was followed with time under gas and temperature. To mimic real conditions, the samples were heated under 1 mbar of N<sub>2</sub> in the ETEM from room temperature to 350°C with a temperature ramp of 4°C/min. To conclude on the influence of the chloride compounds on the Ag particles growth, two samples were studied. One sample was considered as “fresh”, as it had never been in contact with any contaminant. The second sample was submitted to an air flow containing chloride for 7 days at room temperature, similarly to the sample analyzed *post mortem*.

Figure 27 a) shows high resolution images of the fresh sample. The particles have a nanometric size. Ag particles with a sub-nanometric size are also formed in the pores of the zeolite.

The temperature ramps that were applied to the sample are shown in Figure 27 d). Time lapse sequences were made by recording an image every 30 seconds. Particle displacements and growth were analyzed by quantifying the number of events occurring versus time. Similar results were found for both fresh and contaminated samples, with respectively 16% and 15% events of coalescence. 84% and 85 % of the events were respectively represented by Ostwald ripening. As a matter of fact, while particles grew, Ostwald ripening started at around 100°C and became important at 200°C, while coalescence started around 200°C, becoming important around 250°C. However, as shown in Figure 27 b) and c), those phenomena occurred simultaneously. This is highlighted in the circled region: at the beginning, the Ag particles grow through coalescence, then Ostwald ripening is seen at visible scale. I prefer to say “visible scale” because Ostwald ripening can occur during coalescence at a scale that is not resolved.

This was not sufficient to assess if chloride compounds are playing a major role on Ag growth. Therefore, images at a lower spatial resolution were analyzed. That way, a wider field of view was covered and the volume growth rate of the Ag particles was quantified. Figure 27 d) shows the ratio between the Ag volume at a given time and the initial visible volume of Ag at the beginning of the experiment (that was considered as 0% growth). The Ag particles incorporated in the contaminated samples grew faster than the particles in the fresh sample, showing that the chlorides compounds had an important influence on the Ag nanoparticles growth.

In general, to prevent particle growth, catalysts are supported on a support having a specific surface area as high as possible to prevent particle agglomeration and to provide a higher contact surface between the catalysis and the reactants. In the high-resolution images, the particles were observed to be trapped in the defects of the support (Figure 27 a)). We could show, by measuring volume changes, that the volume grow rate of the Ag particles was sustained by Ag

coming from the small atomic agglomerates that were fixed inside the support. In order to be sure that the electron beam had a minimum influence on the experiment, the experiments were performed using a cumulative electron dose of  $119,500 \text{ e}^-/\text{nm}^2$ . The next step of the study could be the investigation of the depth from which Ag at atomic scale is coming, by performing high resolution imaging of ultra-microtomy slices of a sample at the final state.

In this study the electron tomography at low dose was combined with experiments in *operando* conditions in order to comprehend the mechanisms involved in the deactivation of the adsorption process of Ag nanoparticles supported by ZSM-5. It was found that their growth was mainly due to the Oswald ripening process, however coalescence could not be neglected<sup>67</sup>.

In this chapter I tried to highlight the fact that environmental electron microscopy in *operando* conditions combined with electron tomography in vacuum can be used to assess the phenomena occurring during the genesis or the use of a catalyst. I would also like to underline that no technique being perfect, combining different point of views may provide answers of prime importance concerning the activity of a catalysis. That can help the colleagues involved in their development to improve their functions and efficiency.

## 4 Multiscale electron tomography

For most of the articles I co-authored, one of the questions that often came from the reviewer was: “what about the statistics, how many tomograms were made?” This question is particularly relevant, because in general, only several thousands of  $\text{nm}^2$  of projected area through a non-very thin object were visualized in TEM. Nevertheless, statistics are very difficult to attempt in 3D due to the time-consuming process of data analysis, even if we are now able to record a tilt series in several seconds. Of course, during the experiment many 2D analyses are performed, using HR-TEM, EDS, diffraction, EELS, EFTEM. But, in materials science, catalysis, engineering, all scale lengths are important. Seeing wider or “making a step back” (O. Ersen) for “seeing all the pieces of the puzzle” (K.P. de Jong) is important. Therefore, I have started in the last years to focus my interest on multi-scale studies too. Some of them are exemplified in the next sections.

### 4.1 Environmental Scanning Electron Tomography in an ESEM

As shown until this point, my main research activities have been dedicated to the development and the application of environmental electron microscopy to the study of materials in controlled environmental conditions such as gas pressure and temperature. But, environmental electron

microscopy is possible not only in a TEM but also in an Environmental Scanning Electron Microscope (ESEM). ESEM is a tool that allows the insertion of different gases in its chamber at a maximum pressure of 25 mbars. At INSA-Lyon and most precisely in the MateIS laboratory, ESEM in gas or in liquid has already a long tradition<sup>69-72</sup>. The development of ET in ESEM seemed to be a natural step. A home-made stage allowing the rotation of thin samples was built and feasibility results were published in 2011, shortly before my arrival in the laboratory. I have been involved into this research axis since 2013.

#### 4.1.1 3D analysis of grafted CNT dispersion within polyurethane

Electroactive materials do show promising properties especially for actuation and energy harvesting. Materials such as polyurethane (PU) can change their shape and size while they are submitted to an external electric field, meaning that they can convert electrical energy in mechanical energy. In addition, by adding nanofibers such as carbon nanotubes (CNT) into the PU matrices, their electromechanical proprieties can be enhanced. However, CNTs are very difficult to disperse within the PU matrix, and, moreover, the interfacial adhesion strength between CNT and PU is poor. Therefore, a solution to enhance the dispersion of the CNT as well as their adhesion to the PU matrix is to graft polymer chains onto the CNT surface. This study was made in the frame of [Mohamed Jomaa's PhD](#)<sup>x</sup> directed by Prof. Karine Masenelli-Varlot and Dr Laurence Seveyrat and co-supervised by Prof. Jean-Yves Cavallé.

Environmental electron tomography performed in transmitted mode in an ESEM was used to quantify the CNT dispersion in composites containing CNT grafted or not with PU chains into the PU. Three different samples were studied: one as a reference containing 2% of ungrafted CNTs, one containing 2% and one 4% of grafted CNTs within the PU matrix. The samples were prepared for ET using cryo-ultramicrotomy. The tilt series were recorded using a FEI XL-30 FEG ESEM operating at 30 kV under 400 Pa (4 mbar) of water vapor pressure. The water vapor was used to drive away the electrostatic charges that were accumulating on the sample surface, making thus possible the study of non-conductive samples in good imaging conditions.

---

<sup>x</sup> Mohamed Hedi Jomaa, Elaboration, characterization and modeling of electroactive materials based on polyurethanes and grafted carbon nanotubes, L'Institut National des Sciences Appliquées de Lyon, 17/06/2015.

Figure 28 shows cross-sections extracted from the volume of the composites containing 2% CNTs as well as their 3D models. Grafted CNTs are in blue while ungrafted ones are in green.

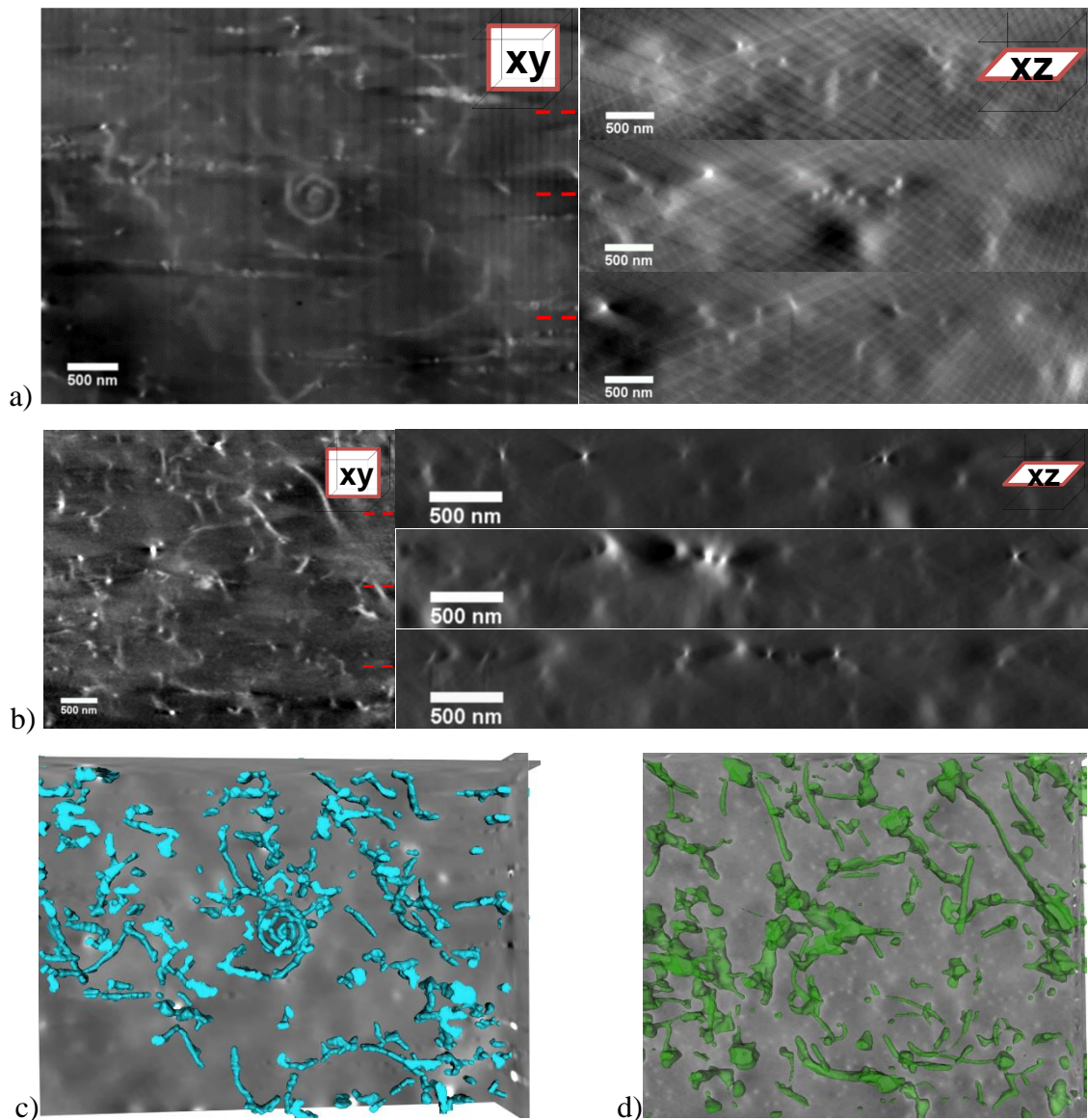


Figure 28: Environmental STEM ET in ESEM of 2% CNTs dispersed in PU. Orthogonal cross-sections through the volumes of the samples: a) with grafted CNTs, b) with ungrafted CNTs. The red dash lines show the intersection between the orthogonal slices. c) and d) 3D models of grafted CNTs in blue and ungrafted CNTs in green. Image from <sup>73</sup>.

The 3D dispersion state of the CNTs as well as their orientation within the PU volume thanks to a routine developed by Daya Sagar Dhungana during his master project under my supervision. CNTs were considered as polylines. Virtual markers were placed manually at the end points of a segment where a direction change was observed. In other words, the CNT were cut into straight segments following the CNT and a virtual marker was placed where the CNT were bent. The polar coordinates of each segment were considered:  $r$  represented the length of the linear segment. The polar angle  $\theta$  represented the orientation of the segment with respect to

the Z axis of the volume and the azimuthal angle  $\varphi$  represented the orientation of the segment in the XY plane of the volume reported to the X axis. Figure 29 shows the quantification method used as well as the orientation of the segments in the volume.

The samples were fabricated by film casting and actually the Z direction of the volume corresponds to the Md direction that represent the machine direction. Md is the direction of the blade that is used to make the PU thin film. When the orientation of the CNT is transposed from the volume coordinates into the coordinates of the film (Figure 29 d)), it was found that the CNT are oriented preferentially along Md, suggesting that the CNT are preferentially oriented by the blade used to make the thin film (mis-orientation of  $\pm 30^\circ$ ).

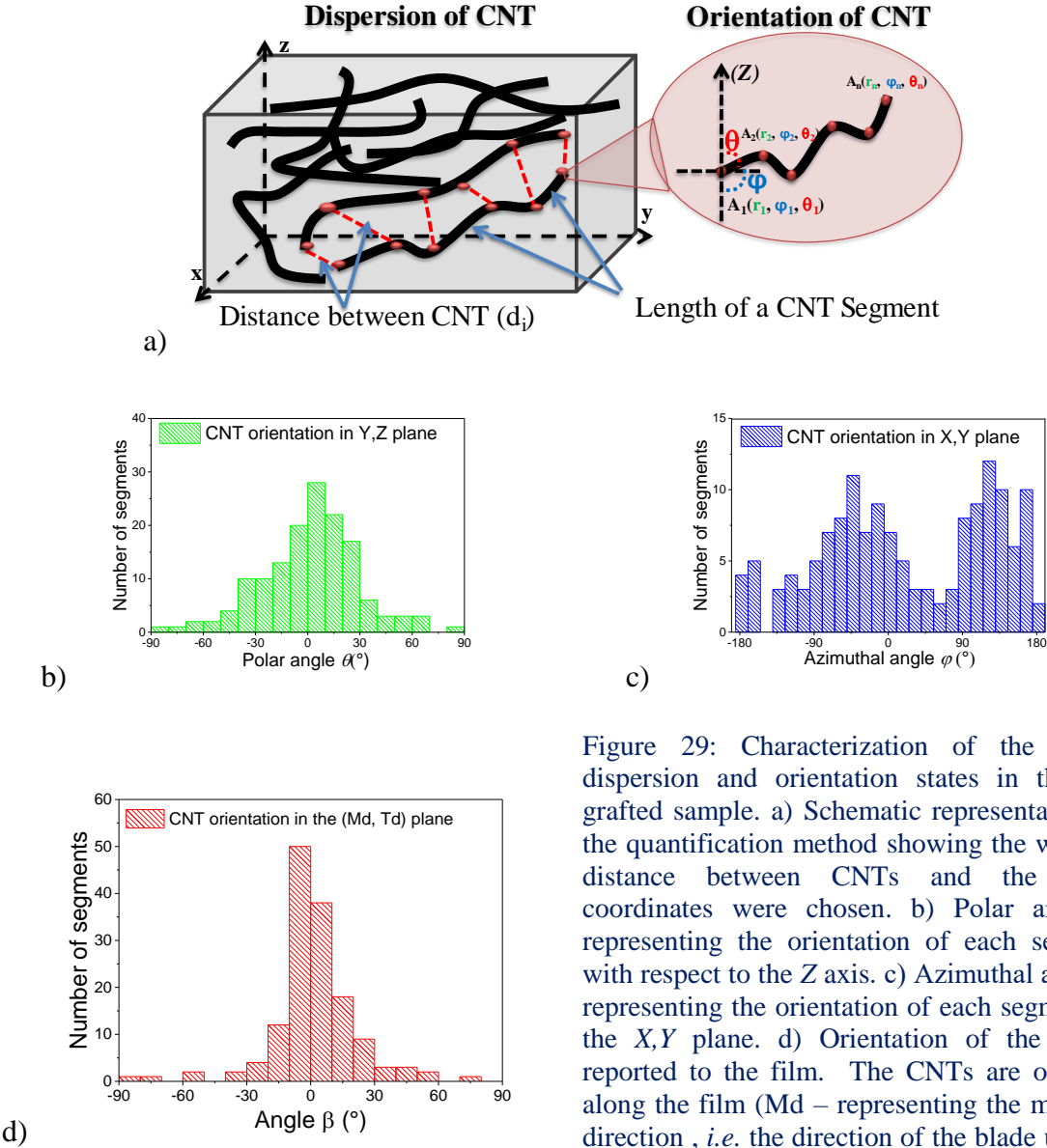


Figure 29: Characterization of the CNTs dispersion and orientation states in the 2% grafted sample. a) Schematic representation of the quantification method showing the way the distance between CNTs and the polar coordinates were chosen. b) Polar angle  $\theta$  representing the orientation of each segment with respect to the Z axis. c) Azimuthal angle  $\varphi$  representing the orientation of each segment in the X,Y plane. d) Orientation of the CNTs reported to the film. The CNTs are oriented along the film (Md – representing the machine direction , *i.e.* the direction of the blade used to make the film).

ET in ESEM provided 3D quantitative data that were used in the evaluation of the influence of the grafted layer and of the CNT concentration over the stiffening of the composite, employing an analytical mechanical model without any adjustable parameter. During the stiffening simulation, the CNTs were assimilated to non-extensive rods (straight segments defined in ET) linked with flexible bonds (virtual markers placed in ET). The mechanical properties of the films could be explained by the CNT distribution and orientation. It was also found that the reinforcing effect was lower than expected due to the CNT waviness at the studied concentrations<sup>73</sup>.

#### 4.1.2 Latex particles suspended in water

Liquid-phase electron microscopy, a modality dedicated to the study of materials suspended in liquid, has gained a lot interest in the last decades with the developments of liquid cells<sup>74,75</sup>. Even if their size do limit the tilt range (around  $\pm 45^\circ$ ), it has been used for the 3D analysis of materials<sup>76</sup> as well as biological systems<sup>77,78</sup>.

Environmental Scanning Electron Microscope (ESEM) is a machine that allows studies under different gases at different temperatures, but also of samples suspended in liquid, for example water, without enclosing the sample in an environmental cell. This is possible by keeping the temperature of the sample at around 2°C under a partial pressure of water vapor around 7 mbar. In such environmental conditions, by staying on the dew curve, the sample can be maintained wet<sup>69,79</sup>. Of course, by varying the vapor pressure or the temperature of the sample, ESEM also allows hydration/dehydration cycles of the samples. Such cycles are a specificity of the ESEM and are not possible in a close liquid cell.

I would like to exemplify the development of ET in ESEM with the study of latex nanoparticles suspended in water. The study was made in the framework of [Juan Xiao's PhD<sup>xi</sup>](#), directed by Prof. Karine Masenelli-Varlot and Dr. Geneviève Foray and supported by the China Scholarship Council. The goal was to demonstrate the feasibility of the ET in an E-StEM by keeping the particles in an aqueous suspension.

The latex was composed of SBA (styrene-butyl-acrylate) -PMMA (poly(methyl methacrylate)), a copolymer derived from styrene and metacrylic acid esters. It forms spheres of diameter around 200 nm in aqueous solution. When dried, an irreversible transformation occurs by

---

<sup>xi</sup> Juan Xiao, Development of electron tomography on liquid suspensions using Environmental Scanning Electron Microscopy, l'INSA Lyon Ecole Doctorale EDA034, Ecole Doctorale Matériaux de Lyon, 13/06/2017.

diffusion of the copolymer chains and thin uniform film is formed. Therefore, such material is ideal to prove that the sample was always preserved wet during the time of the experiment. The experiential set-up was developed at MateIS, and consists in a 360°- rotating stage, two translating piezoelectric systems able to place the sample at the eucentric position, a Peltier stage equipped with a thermocouple that is connected to the FEI thermoelectric stage controller, and a sample holder<sup>71</sup> on which a TEM microscopy grid is placed. To keep the sample wet, a droplet containing the suspension is placed on the grid and cooled down to the target temperature. 4 other droplets are placed on the holder near the sample but at uncooled places. During the purging process, these 4 droplets evaporate and prevent the evaporation of the sample.

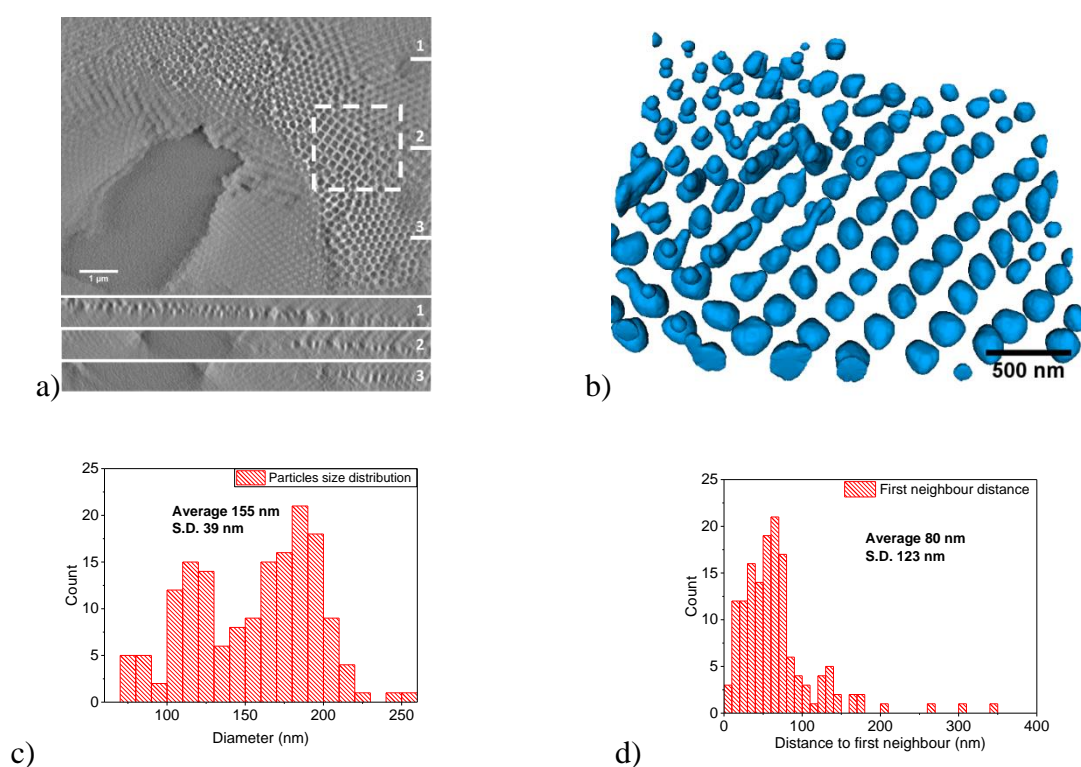


Figure 30: 3D self-ordering of SBA-PMMA latex particles suspended in liquid water. a) Orthogonal slices parallel to the XY (top) and XZ (bottom 1,2 and 3) planes extracted from the reconstructed volume of size  $X*Y*Z = 9488*7163*3000 \text{ nm}^3$ . The slices intersection is shown by the white line. b) 3D model of the region indicated by the white square in a) (model volume:  $X*Y*Z = 2220*2430*1560 \text{ nm}^3$ ); c) Particle size distribution measured from the 3D model. d) Distance to first-order neighbors. Image from<sup>80</sup>.



Figure 30 shows orthogonal slices from the volume of the latex particles suspended in water. The tilt series were deliberately recorded at a lower resolution, that was estimated by Fourier Shell Correlation (FSC) at 23 nm and by  $\sigma$ -criterion at 31 nm. It can be seen that the latex particles are assembled in small domains, also, it can be seen that in some areas two layers are formed. The dark region is a hole in the carbon layer supporting the latex. In the cross-sections, the latex particles appear darker than the surrounding water, in agreement with Monte Carlo simulations<sup>81</sup>. The 3D model was performed by cropping the volume marked with the white rectangle. The quantification made revealed that the average particles size distribution is around 155 nm, less than the measurement made on particles on 2D<sup>82</sup>. However, by analyzing the

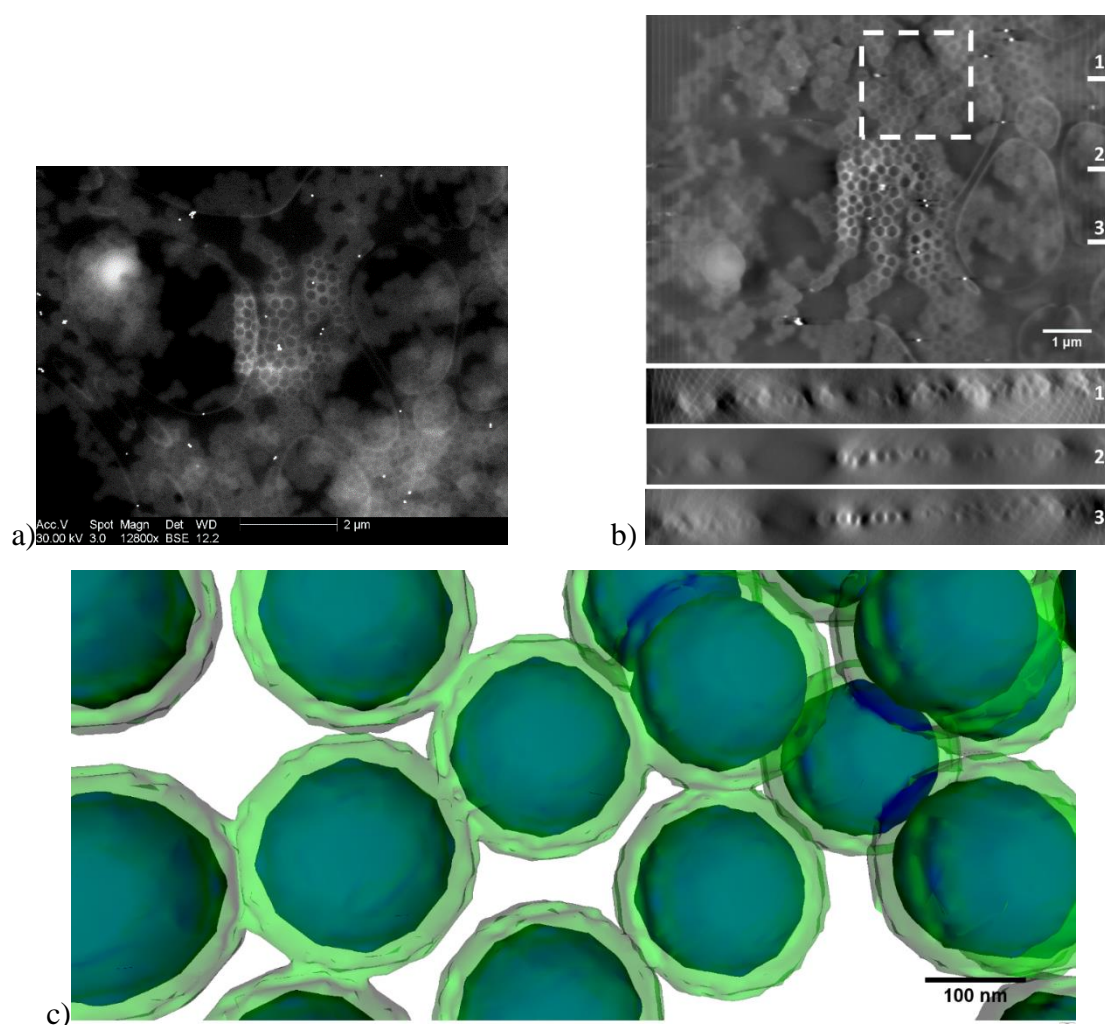


Figure 31: 3D ordering of SBA-PMMA latex particles in liquid water in presence of a surfactant. a) STEM in ESEM image acquired at  $0^\circ$ . The white dots are gold nanoparticles used as fiducial marks. As said in the text the latex particles are darker than the surrounding water. ; b) Orthogonal cross-sections extracted from the reconstructed volume ( $X*Y*Z = 9593*7133*3000 \text{ nm}^3$ ) where the white lines indicates the slices intersection; b) Ideal 3D model of the region indicated by white square in b) (volume:  $X*Y*Z = 2400*2325*1395 \text{ nm}^3$ ). The SBA-PMMA particles and the surfactant are represented in blue and green respectively. The surfactant shells intersect when the latex particles are close to each other. Image from<sup>80</sup>.

histogram in Figure 30 c) two peaks are visible. The first one corresponds to the latex particles forming the second layer of particles. Due the reconstruction artefacts and to the elongation factor, these particles could not be resolved properly. Indeed, from a technical point of view, the tilt series were recorded by tilting the sample between  $\pm 60^\circ$  with an increment of  $2^\circ$ , in order to avoid intense irradiation damage (in the latex and in water). Therefore, the volume was affected by an important missing wedge that do not allow the resolution of the spherical particles that are out of the X, Y plane. The second peak corresponds to the real size of the latex particles that were forming a single layer on the carbon membrane and that were properly resolved. For the same reason, the distribution of the distances to first neighbors contained several values that were overestimated (Figure 30 d)). The distances correspond to the distance from surface to surface and not from center to center so if the diameters of the particles in the second layer are underestimated, the distance to the first neighbors are overestimated.

In this study a second sample was investigated, but this time a surfactant was added at a concentration at which the surfactant entirely covers the latex beads. Figure 31 shows the projection at 0 tilt, where the surfactant appears as a bright circle around the particles. Cross-sections from the volume of the sample are also given. To build the 3D model, this time the particles were modeled with perfect spheres. The thickness of the surfactant was measured around 25 nm, in line with the 3D spatial resolution, estimated between 23 and 26 nm.

This study evidenced that ET is possible in liquid phase by preserving the native state of the sample in liquid and by working in transmission in an ESEM<sup>80</sup> with no closed environmental cell.

#### 4.1.3 Towards 3D analysis of whole biological cells in native state?

Akkiz Bekel is preparing her PhD under the direction of Prof. Karine Masenelli-Varlot and me, with the help of Dr. Claire Gaillard. The main goal is to develop a way enabling the study the cells interactions with their support in order to better understand the development of future personalized implants. She tries to establish a possible procedure to investigate whole biological cells in 3D using ESEM in conditions close to their native state.

Today the biological samples are mainly analyzed dehydrated or in cryogenic conditions, where small parts of a cell are frozen using liquid nitrogen and investigated at high resolution. However, we believe that technological developments may allow the analysis of biological materials in conditions close to the native state, *i.e.* hydrated.

Figure 32 shows the 3D model of a NIH-3T3 cell. The cells were cultivated on an Au microscopy grid covered with a carbon membrane, then fixed with glutaraldehyde (but not stained), and kept in buffer medium. The sample was then analyzed in 3D in liquid phase. The tilt series were recorded in BF and HAADF modes in StEM. Figure 32 shows the 3D model made from the BF volume, and orthogonal cross sections from both reconstructed volumes. The

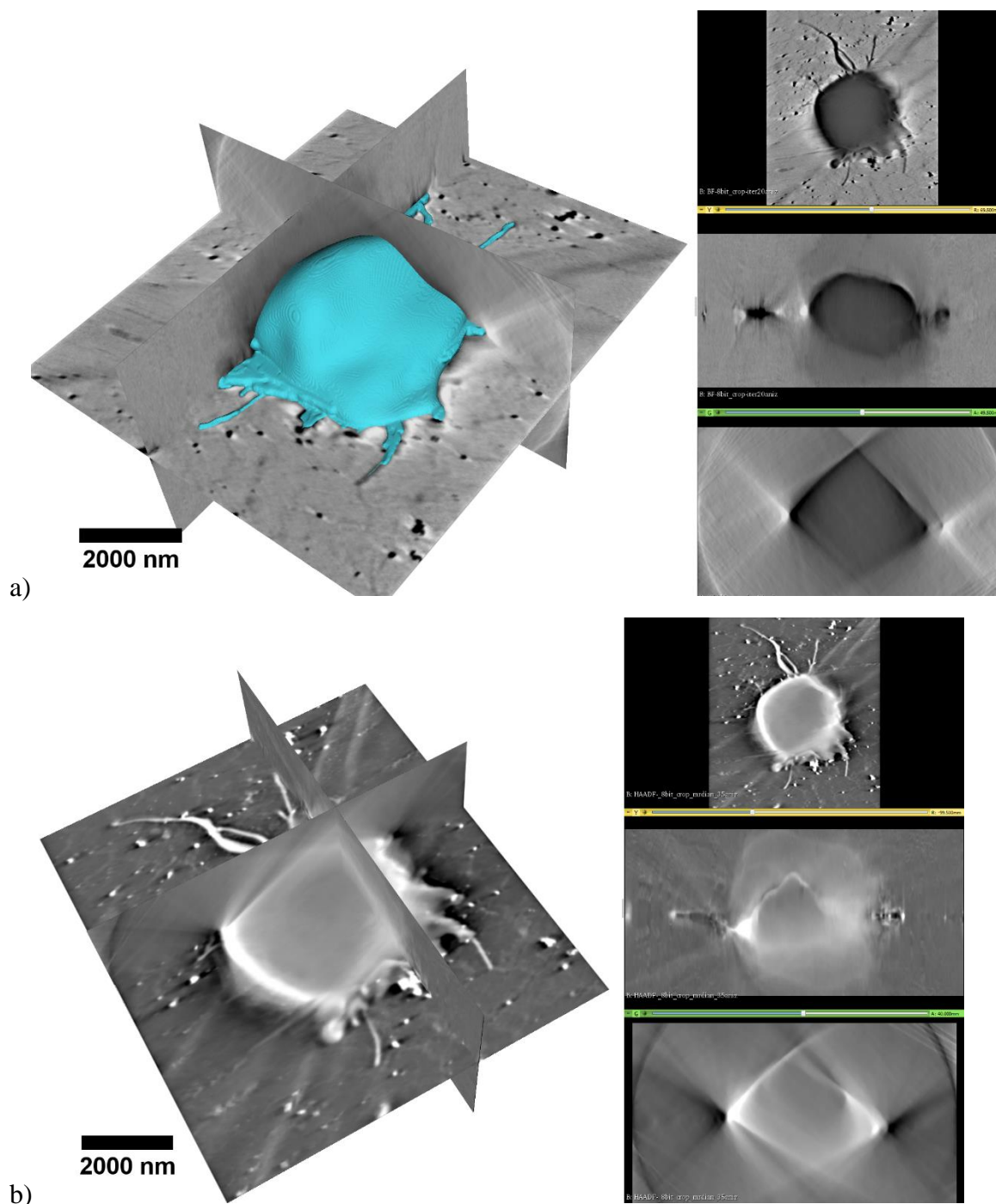


Figure 32: NIH-3T3 biological cell supported by a carbon membrane. The tilt series in BF (a) and HAADF (b) mode were recorded in liquid using ESEM. The model of the cell made from the BF volume is shown in a).

complementarity of the information but also the influence of the missing wedge are visible in the YZ plane (green sections at the bottom right) as they considerably deform the cell in the Z direction. Combined with the intense electron scattering due to the large thickness of the cell, such deformation made data segmentation a hard task. However, the results show that it is possible to analyze a whole hydrated cell in buffer medium with electron microscopy. This topic will be also discussed in the perspective section.

## 5 Perspectives

I had the chance to experiment different imaging techniques at multi scale in S/TEM, SEM and X-Ray tomography when considering the resolution scale<sup>83,84</sup> of the 3D imaging techniques, these techniques cover an important part of the spatial resolutions available today. I have also had the opportunity to study a large variety of samples, in bulk as well as surfaces, from catalyst nanoparticles at high temperature to hydrated biological samples at low temperature. The broad overview provided by the techniques and the samples give me the possibility to propose several perspectives.

### 5.1 Multi scale tomography

In the future I will like to go towards multiscale analysis in materials science, although of course, S/TEM 3D as well as environmental studies and technical developments in TEM and SEM will remain the main activities. In this part I will try to exemplify some of the projects on which I am currently working as well as those that I consider developing in the future.

#### 5.1.1 X-ray tomography applications in the study of some pathologies of the internal ear

The development of a straight gauge made by Pt nanoparticles supported by Al<sub>2</sub>O<sub>3</sub> was introduced in section 1.2.1<sup>31</sup>. The gauge was found to work properly around 1-2 Hz, that is also the response range of the “movement detectors”, the kinocilium that is found in a semicircular channel of the internal ear.

In cooperation with Dr. Etienne Puyoo and M.D. Eugen Ionescu from the Hospices Civils de Lyon, we are developing the project generically named “Non Invasive Simulation of the Inner ear Pathologies” (NISIP) that proposes the development of a physical model of the vestibular system of the internal ear. Such a model will allow the simulation of several pathological

conditions under which the transmission of acoustic energy ensured by the propagation of perilymphatic waves between the two physiological windows (the oval and the round ones) is deviated - or shunted - with variable adverse effects for optimal audio-vestibular function. This model will allow the non-invasive simulation of certain pathological situations, such as an "insulation defect" of the wall of the vestibule or an elasticity of the latter, in order to identify or confirm the different pathological mechanisms or to propose therapeutic solutions.

To date, the only mechanism concerning the "classic" form of vertigo induced by a dehiscence of the semicircular canal (SSCD) described by Minor<sup>85</sup> has been identified, while still keeping some ambiguities concerning the limits between the pathological forms and non-symptomatic forms.

#### *Why such a project?*

It is estimated that about 20% to 40% of the global population suffers from a type of vertigo, due to some defects of the inner ear. Some experiments conducted on animals or humans have explained some pathologies. This type of experiments being both non ethical and very expensive cannot explain all the pathologies of the inner ear<sup>86-89</sup>. The audiology and otoneurological explorations service of the Hospices Civils de Lyon has recently proposed new methods of treating patients suffering from vertigo that have been highly appreciated by the international medical community<sup>90,91</sup>. However, treatment methods, before being applied to patients, need a non-invasive theoretical and experimental confirmation.

The inner ear has mainly two main functions: hearing and balance. Dizziness is the result of a defect in one or more walls of the semicircular canals, for example dehiscence or elasticity of the walls, which can cause undesirable energetic transfers of the acoustic waves causing over excitation of the bulb that plays the role of pressure detector of the human gyroscope.

We would like to develop a simple simulation device of certain internal ear diseases related to vertigo. The goal is to manufacture using 3D printing or molding starting from the 3D information of a patient obtained by computing tomography an object at a certain scale, scale 1 is for now limited<sup>92</sup>, on which the above-mentioned gauge will be inserted and different pathologies caused by physical defects will be studied.

My contribution to this project will be done in cooperation with Dr. Jérôme Adrien and Dr. Eric Maire to develop a system that will enable the X-Ray *in situ* study of the straight gauge deformation while different sounds or forces will be applied. Such experiments will not only characterize the morphology of the manufactured 3D object but will also give insight of the

way a sonic wave of a certain frequency and intensity will propagate through the semicircular channel suffering of certain defaults i.e. dehiscence or elasticity of the wall. The findings will be corroborated with electrical measurements and with clinical investigations. The goal is not to propose an implant to the patients but provide a tool that will help the medical doctors to propose successful treatments with minimum invasions and harm to the patient, such as was done by installing a stent in one of the veins crossing over the one of the semicircular channels<sup>91</sup>. A second goal of the project is to develop a pedagogical tool dedicated to medical schools in order to help the teaching of vertigo.

#### 5.1.2 E-SEM applied to the study of the interactions between a cell and a biomaterial

I briefly mentioned the thesis of Akkiz Bekel in section 4.1.3, where I focused on the feasibility of electron tomography in liquid phase to study a full-size cell attached to a support. However, a second goal of the thesis is to assess the complementarity between E-SEM and confocal microscopy in the study of the interface between a cell and a biomaterial. Confocal microscopy is the recognized technique in the study of biological samples, however, we think that the E-SEM analysis performed on samples suspended in liquid can provide complementary information regarding the anchorage sites of a cell to its support. This can be done by the fact that the water vapors are facilitating the images recording by driving away the charges that are accumulating on a nonconductive surface. The analysis of the biological samples and its original approach in the MateIS lab required a lot of time in the preparation of the analysis protocols but the work is in progress and the results obtained by electron tomography are very encouraging. Indeed, it must be pointed out that, as seen in Figure 32, the experimental settings need to be modified because no information, until now, is visible inside the cell. To date, we have been focused on the electron dose that could be used to analyze the sample, as well as on noise quantification (more details are given in the last paragraph of this section). But more parameters such as the working distance and the beam convergence should be tested in order to provide information from the volume of a whole cell.

The work started in the frame of Akkiz's PhD will be continued by Louis-Marie Lebas, who started his PhD under the direction of Prof. Karine Masenelli-Varlot and myself. This work is performed in the frame of the project *Liquid3DSTEM*, which is a cooperation between MateIS and the Institute for New Materials, Saarbrücken. The project is led by Prof. Karine Masenelli-Varlot and Dr. Niels de Jonge, and is co-supported by the French Research National Agency

(ANR) and the Deutsche Forschungsgemeinschaft (DFG). The work of Louis-Marie will be focused on the development of liquid-phase 3D imaging of biological and beam-sensitive samples (latex and aerogels). Here, 3D is not related only to the electron tomography but also to the 3D surface reconstruction. Figure 33 shows the surface and the textural reconstructions of a MC-3T3 cell supported by a carbon membrane, obtained using the free, open-source software Meshroom developed by AliceVision<sup>xii</sup>. The idea is to combine the 3D reconstruction with the 3D surface reconstruction in order to provide as many details as possible on the position and morphology of a cell on its biomaterial. The goal is to provide a complementary investigation tool of the interface between a cell and biomaterial.

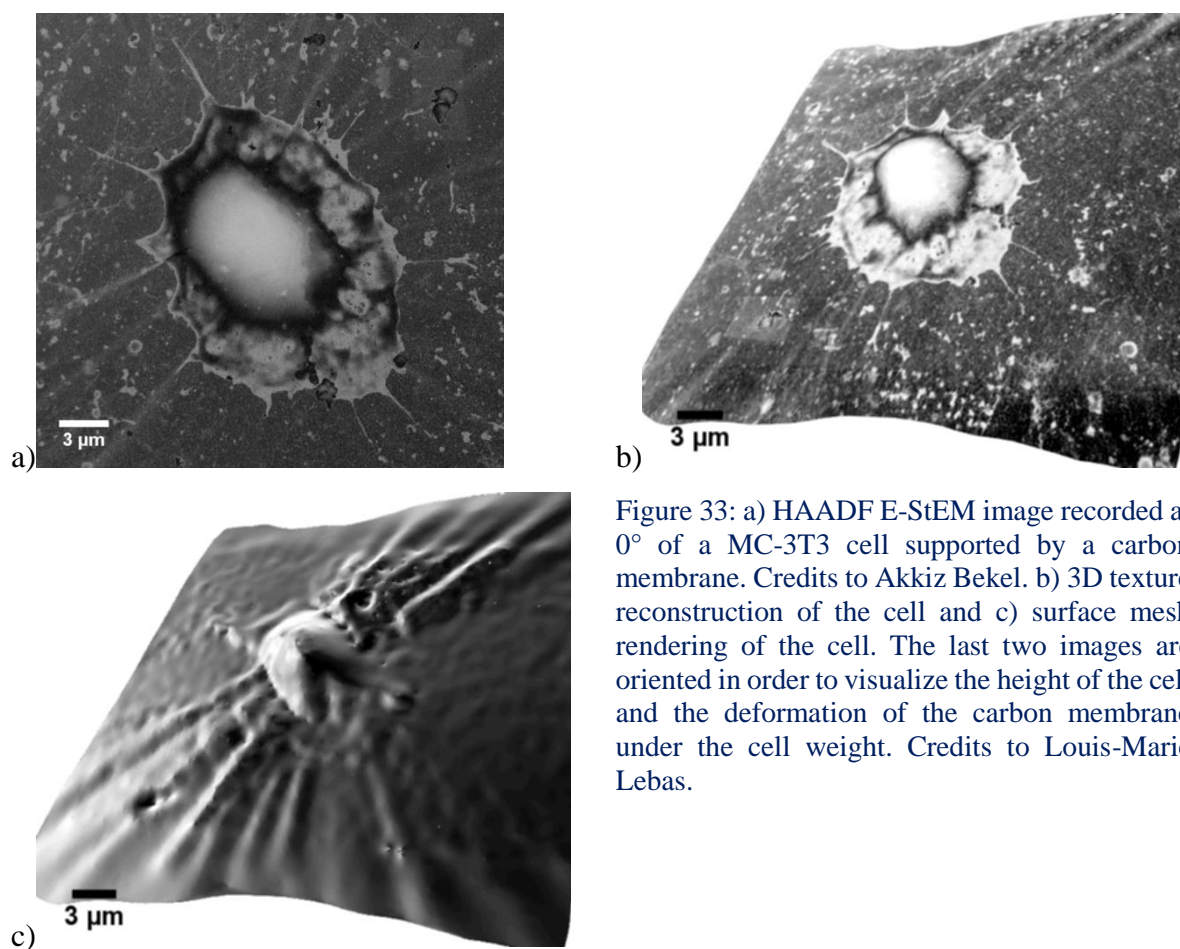


Figure 33: a) HAADF E-StEM image recorded at 0° of a MC-3T3 cell supported by a carbon membrane. Credits to Akkiz Bekel. b) 3D texture reconstruction of the cell and c) surface mesh rendering of the cell. The last two images are oriented in order to visualize the height of the cell and the deformation of the carbon membrane under the cell weight. Credits to Louis-Marie Lebas.

The experiments made using the tomography wet STEM device developed in our group<sup>71</sup> within the thesis of Akkiz proved that more developments are needed. Until now, only materials with a nanometer size have been analyzed. On the contrary, an adherent cell can spread over several μm<sup>2</sup> and be 1-3 μm thick. Therefore, the contrast can change while tilting the sample and

<sup>xii</sup> <https://alicevision.org/#meshroom>

preserving it in the field of view. This can be due to the fact that the thickness crossed by the electrons increases<sup>81</sup>. It can also be attributed to the fact that mechanical rotation of the holder is not perfect and the sample is not aligned anymore with the detector. Therefore, in the framework of Liquid3DSTEM project on which Louis-Marie Lebas is involved, a new 3D liquid stage will be developed. It will allow the movement of the detector in the plane XY, making possible the alignment of the sample with the center of the detector at any moment of the experiment.

Within the framework of Akkiz's PhD, several national cooperation have been initiated, and will be continued during Louis-Marie's PhD. One of them is with our colleagues from the University of Franche-Comté with Dr. Soukalo Dembélé and Prof. Nadine Piat. They have developed a routine that is able to assess the signal-to-noise ratio in a SEM image<sup>93</sup>. They have also developed a 3D surface reconstruction software called Pollen 3D<sup>94,95</sup>. The goal of this cooperation is to develop a routine able to be used in environmental electron microscopy. To be more precise, a whole cell is a relatively "thick" object, and the depth of field is not always sufficient to have all the morphological features in focus. Therefore, the signal-to-noise ratio is difficult to estimate in an image. Moreover, we want to submit the sample to the lowest possible electron dose. Therefore, the images are less contrasted and noisier. The goal of the cooperation is also to filter noise and enhance the signal in the image so that it can be used for 3D (surface) reconstructions of the sample. Concerning 3D surface reconstruction, my colleague Dr. Cyril Langlois developed a tilt - rotative stage for SEM, able to tilt and rotate the sample over 360° with the rotation axis parallel to the electron beam. Pollen 3D is able to reconstruct the surface of a sample using a tilted series, however by using a tilted and rotated image series, the surface of more morphological complex samples should be reconstructed with a higher accuracy. Why rotating the sample is important? Similarly to transmitted electron tomography, when the sample is only tilted, the equivalent of a missing wedge is visible in the surface reconstruction along the tilt axis. Therefore, by using a tilted and rotated image series, the missing wedge should be reduced and the 3D surface reconstruction should be better resolved. Those cooperations are ongoing and we hope to show some valuable results in short time.

## 5.2 Multi-scale environmental electron microscopy

In the perspective of multiscale investigations in environmental mode, I wish to combine the complementarity of the ETEM and ESEM in order to show, as much as possible, a statistical and quantifiable field of view of the samples, from atomic to micrometric resolutions. Here I will provide a few examples of such multi-scale studies.



### 5.2.1 Ni metal nanoparticle growth

In section 3.2.1, I exposed the *in situ* growth of Ni particles at the surface of a perovskite using ETEM. At MateIS, a heating electrochemical stage for E-SEM is currently under development. I want to contribute to the technological development that will enable metal particles exsolution experiments using environmental SEM along with E-TEM. The goal is to perform complementary scale experiments.

Dr. Dragos Neagu, from University of Strathclyde, showed that in some conditions of ionic concentrations, metal particles are precipitated in the volume of the perovskite. To understand the dynamics of the metal nanoparticle growth, electron tomography in both ETEM and ESEM in transmitted STEM mode will also be performed. Of course, the goal is to perform the 3D analysis in operando conditions depending on the control of the dynamics of the experiment. Currently, within the framework of the ongoing project EN-CAS, IMUST, headed by Dr. Philippe Vernoux and Dr. Philippe Steyer some of the experiments are ongoing.

### 5.2.2 Adjuvants in liquid phase

The 3D study of latex particles suspended in water was described in section 4.1.2. The study of materials suspended in liquid will still be part of my concerns. For example, I want to evaluate the pertinence of liquid-phase electron microscopy in the characterization of aluminum salts used as adjuvants for vaccines directly in their native state i.e. aqueous gel. Experiments in liquid phase are important to understand the morphological changes of the aluminum salt while dispersed in the blood stream. Moreover, by performing hydration-de-hydration cycles it will be possible to assess the morphological changes of the adjuvants during the storage of the vaccine. Does the aluminum salt change its shape after hydration if re-hydrated? Will it regain its initial morphology? TEM study have already been performed on such samples, but never in their native state: the samples were embedded in a resin and analyzed under high vacuum. Therefore, such approach could bring a new input on those materials that have such an important application. Of course, the studies should be performed in both ESEM and ETEM in liquid phase (the development of liquid-phase ETEM will be described in the next paragraph).

## 5.3 TEM applied to the study of materials under both HV and *operando* conditions

I preferred to close the perspectives section with TEM because its use was representing the largest part of the document, although I crossed a little through X-Ray tomography and E-SEM based studies. Here, TEM can be considered as a generic appellation of the imaging techniques that can be performed employing a TEM.

### 5.3.1 Environmental HRTEM of bimetallic particles AuAg and AgAl

In the near future I will involve myself in the characterization of bi-metallic particles with interest in optical applications. The experiments will be performed in joint experiments, under high vacuum as well as under environmental conditions. One of the electron microscopes available in the CLYM consortium is able to allow atomic chemical resolution in EDX-STEM. It will allow the study of the chemical distribution in bi-metallic nanoparticles such as Au-Ag or Ag-Al. It is worth mentioning that I got a certain experience in such plasmonic nano-objects within the framework of a bilateral cooperation with P. Vaz from Portugal (PESSOA Project) on PVD Ti-Ag films<sup>96</sup>. The goal is to assess and corroborate the optical response of the nanoparticles with their chemical distribution. It must be mentioned that Au and Ag are known to easily form alloys that are stable in air. On the contrary, due to the oxidative affinities of Al, Ag and Al form particles having an Ag core and an oxide Al shell. Therefore, a very demanding goal is to reduce the Al from the nanoparticles at nanometric size (3-10 nm) and see what the final morphological and chemical configuration of the nanoparticles are in controlled atmosphere<sup>97,98</sup>, *i.e.* alloy, janus or core-shell. In conclusion, in this project complementary experiments will be performed in HRTEM/HRSTEM under high vacuum and HRTEM/HRSTEM in environmental mode in order to corroborate the optical response of the nanoparticles with their chemical distribution. This work will be performed in the frame of the ANR project SchNAPS headed by Dr. Matthias Hillenkamp from ILM lab in cooperation between MateIS from Lyon University, LPS lab from Université Paris-Sud and CINaM lab from Université Aix Marseille. Figure 32

### 5.3.2 Environmental electron microscopy of functional materials

I will also continue to study different samples such as catalysts, supports of catalysts, polymers, etc. under high vacuum, as well as under *operando* conditions and ET in cooperation with my colleagues from MateIS, LMI, INL and IRCElyon and from other universities or institutions.

As it was shown in this document, my main activity was dedicated to the development of fast imaging recording for ET. I will continue on the implementation of *operando* ET studies of large number of samples. To date, the main study has concerned the genesis, the calcination or the oxidation process of a catalysis. But many more other studies could be performed using ET in ETEM.

For example, the aging of mesoporous silica for building insulation was described in section 2.2.2, but all studies were made *post mortem*. The study of the aging dynamics of silica can be performed in ETEM by creating the conditions similar to the ones used *ex situ*, *i.e.* with water vapor and temperature. For samples such as mesoporous silica, the electron beam can have an important effect on sample aging but by assessing the maximum electron dose that can be accepted, the undesirable effects of the electron beam can be limited. The evolution of the samples with time under controlled atmosphere to accelerate aging can be performed *in situ*. Such experiments can be performed at different magnifications by periodically recording an image then blanking the electron beam. In *ex situ* experiments, the samples were aged during several days at 70°C under 90% of relative humidity. In the ETEM it is possible to insert water vapor at a pressure of around 12 mbar, and by using a heating sample holder the sample can be submitted to similar conditions as in *ex situ*. A difficulty of such experiments is the fact that the sample must be preserved under environmental conditions for a long period of time, even several days, time that are blocking the ETEM for use. A solution could be the use of a close environmental cell that will allow preserving the sample at the same temperature and vapor pressure and let free the microscope for other users.

### 5.3.3 Liquid phase in ETEM

As I showed in ESEM, it is possible to study samples suspended in liquid water. Therefore, the development of a liquid sample holder compatible with the ETEM it is a natural step. It is possible to insert water vapor into the ETEM while cooling the sample around 5°C. Under these conditions, the sample could be immersed in liquid. Such development are scheduled in the WATEM project. It is a cooperation between MateIS, IRCELyon and MajuLab Singapore, coordinated by Dr. Thierry Épicier and supported by the French Research National Agency (ANR). The holder is currently under development. It will be based on a MEMS chip compatible with the DENSSoliton WildFire heating folder.

It is also possible to cool the sample down to a few degrees, by using a cryogenic sample holder. However, the sample holder is not optimized for this temperature range using liquid nitrogen.

By using only liquid nitrogen and preserving the sample at relatively high temperatures compared with  $-196\text{ }^{\circ}\text{C}$ , the heating stage of the holder induces an undesired drift and makes the data difficult to process. By using a mixture of alcohol and liquid nitrogen, it is possible to control the temperature between  $20^{\circ}\text{C}$  and  $-110^{\circ}\text{C}$ . However, it is hard to preserve a constant temperature. Nevertheless, the temperature variations are slow and it is possible to make heating-cooling cycles, compatible with drying-wetting processes. I must admit that the experiments are difficult and laborious. Therefore, going towards the MEMS technology could be a reliable solution.

## 5.4 Pushing the limits of electron microscopy

In this section I would like to share three ideas on which I will focus my thoughts during the next part of my career. Those ideas could seem more principled than realistic, but I think they are worth giving a thought in the next years.

### 5.4.1 AI in electron microscopy?

Today the development of Artificial Intelligence (AI) is a major topic in all scientific fields from social science and philosophy to applied and theoretical physics and engineering. AI is also increasingly applied in the fields of electron microscopy: for instance, some algorithms based on machine learning are already being used for data segmentation in tomography. However, I strongly believe that the implementation of an AI in the control system of an electron microscope could help a lot, for example for the microscope alignment or the alignment of the correctors. Some scripts already exist, that allow an automatic alignment of the correctors. However, there is still a lot of space for development and is more dependent by the microscope manufacturer than by a scientist. However, it can be mentioned that Lyon University through the [l'EUR Manutech Sleight](https://manutech-sleight.com/en/)<sup>xiii</sup> gathered partners that cooperate on this topic and some outcomes could be revealed really soon.

Other aspects on which an AI could help in electron microscopy is the management of data bases. For example, life indexing of diffraction patterns and HRTEM images could be helpful during *operando* experiments. An AI could propose solutions - with a certain accuracy and within a very short time - for the phases that could be present in a sample. Concerning electron tomography an AI could be helpful in the volume reconstruction. The object deformation due

---

<sup>xiii</sup> <https://manutech-sleight.com/en/>

to the missing wedge is dependent of the object size and shape of the object and in a volume are often several objects. An AI could identify the size and the shape and adjust the missing wedge elongation accordingly.

#### 5.4.2 Further in time: faster and faster image recording for ET

In the longer term, I would like to dedicate myself to the development of a fast tilting system that would reduce the recording image time for a tilt series in BF imaging mode under one second. Today, the tilt speed is limited by the tilting technique itself. Over the years, the goniometers that are supporting the sample holders have been developed to stand still in order to allow atomic resolution. They have never been designed to rotate and moreover to rotate fast. Therefore, the development of a new rotation system would open the way for a real 4D electron tomography<sup>99,100</sup>, where very short time-resolved experiments could be performed. Such a system could be inspired from other fields like fine mechanics or watchmaking, and would be key for new physico-chemical phenomena that were never explored live in electron microscopy.

I believe that two solutions could be considered:

- the first one could consist in the development of a new goniometer dedicated to the fast rotation of a high tilt holder. With the current technology, a goniometer is composed of more than 100 parts. By reducing the number of components and replacing the serrated wheels by belts, it might be possible to enhance the stability of the goniometer, *i.e.* reduce the vibrations during high speed tilt.
- the second solution could be the development of a high speed tilt sample holder based on the current technology, but with rotation of the sample inside de microscope. The technology could be inspired from watchmaking. The advantage of this type of holder is that it could heat or cool down the sample while enabling environmental experiments along with tomography.

#### 5.4.3 Even further in time: Adaptive environmental corrector for environmental electron microscopy

During the last few years, the development of the corrective devices in electron microscopy, such as spherical and chromatic correctors, has provided a large improvement of the spatial resolution that can be achieved in TEM<sup>101</sup>. Such devices are very helpful for experiments under environmental conditions, either under gas or in liquid. However, such aberration correctors have been designed for experiments under high vaccum. Indeed, they work properly for stable

objects and environments, which is ephemeral in environmental mode<sup>75</sup>. Therefore, to insure a continuous high spatial resolution in environmental mode, the development of a dedicated “environmental corrector” may be required. The design of such a device could be inspired from astronomy and more precisely from adaptive optics, used to enhance the resolution in images of far objects<sup>102–104</sup>. In environmental microscopy, to increase the spatial resolution in the experiments, the solution is not to hope that the imaging conditions will not change while the images are recorded but to adapt the electrons path in order to correct their path difference due to the environmental conditions. In adaptive optics, a LASER beam having a perfect circular shape is directed towards the desired destination. Then an image is recorded. The adaptive optics consists in an optical system having adjustable positions of small sized mirrors that are moved until the image of the LASER beam is recorded perfectly circular. In a similar way, in environmental electron microscopy a known sample could be used as a reference. Au nanoparticles in spherical or cubic shape with a known exposed family plane, oriented thin films, could play be used as references. By knowing the orientation of the reference, the environmental corrector could compensate the path difference of the electrons in order to gain spatial resolution. Then, the electronic setup could be applied to the analyzed sample. Of course, the design should consider all the stages of an electron microscope, from the electron gun to the projector lens, in order to insure an Adaptive Optics of the electron microscope in function of the environment made, liquid or gas, around the sample.

## 6 Ending word

In this document I tried to expose as briefly as possible some of the projects on which I have had the chance to be involved as a partner or that I have had the honor to coordinate. I wanted to show my contribution in the field of electron microscopy and more precisely in the field of electron tomography and environmental electron microscopy. The development of the fast image recording method for electron tomography in bright field mode enabled, firstly, the 3D analysis of beam-sensitive materials with no special sample preparation, and secondly the 3D analysis of the intermediary states of materials submitted to environmental conditions. However, I want to emphasize the fact, that for each sample, the acceptable electron beam dose should be estimated, so that no morphological changes are visible in the tilt series due to beam damage.

Under environmental conditions, the quasi-stable intermediary states of the sample can be followed in 3D. This is a big step forward compared with the investigations made before and after, or *post-mortem*. By performing *operando* experiments in 3D, it is possible to explain and understand some of the morphological and chemical changes that are occur in a given environment. In consequence, it is possible to modify and adapt the sample to its potential real application. I also want to insist that during environmental electron microscopy experiments in 2D or in 3D, the data obtained as well as the results should not be taken as granted. It is wise to assess as accurately as possible the influence of the microscope environment on the *in situ* experiment. In other words, it is important to understand that the environmental electron microscope is a tool that allows the simulation of some precise and limited environments, but is not the exact environment in which the sample is used in real applications.

I also wish to underline that my work is orientated towards multiscale investigations, from atomic to micrometer resolution. In the future, I would like to combine the potentials of TEM, with those of the SEM and X-Ray tomography. The goal would be to provide the widest possible field of view of all the morphological and chemical features that could influence the properties of the sample both under high vacuum and in gas- or liquid-phase modes.

# Abbreviations

## A

- ADEME
  - French Environmental Transition Agency, 32
- ALD
  - Atomic Layer Deposition, 14
- ART
  - Algebraic Reconstruction Technique, 28

## B

- BA
  - butyl acrylate, 34
- BF
  - bright-field, 12

## C

- CNT
  - carbon nanotubes, 58
- Consortium Lyon Saint-Etienne de Microscopie, 4
- CRRET
  - continuous rotation and recording, 23
- CV
  - cyclic voltammetry, 17

## D

- DPF
  - Diesel Particulate Filters, 36

## E

- EFTEM
  - Energy Filtered Transmission Electron Microscopy, 12
- EISA
  - Evaporation Induced Self Assembly, 17
- ESEM
  - Environmental Scanning Electron Microscope, 58
- ET
  - Electron Tomography, 12
- ETEM
  - Environmental Transmission Electron Microscope, 36

## F

- FIB
  - Focused Ion Beam, 13
- FSC
  - Fourier Shell Correlation, 63
- FTIR
  - Fourier Transform Infrared, 32
- FTO
  - Flourine –doped Thin Oxide, 17

## H

- HAADF
  - High Angle Annular Dark Field, 12

## I

- IFSM
  - Award of the International Federation of Societies for Microscopy, 5

## L

- LDH
  - Mg<sub>3</sub>AlCO<sub>3</sub> layered double hydroxide, 34

## M

- Mateis
  - Matériaux Ingénierie et Science, 4
- MEMS
  - microelectromechanical systems, 44
- MMA
  - methyl methacrylate, 34

## O

- OSART
  - Ordered Subsets Algebraic Reconstruction Technique, 28



## **P**

PU

polyurethane, 58

## **S**

SBSET

optimized step by step, 26

SET

Single Electron Transistors, 14

SIRT – FISTA – TV

Simultaneous Iterative Reconstruction Technique –  
Fast Iterative Shrinkage Thresholding Algorithm –  
Total Variation, 28

SSCD

semicircular canal, 67

STEM

Scanning Transmission Electron Microscopy, 12

## **T**

TEM

transmission electron microscope, 12

## **W**

WBP

weighted back projection, 24

## **Z**

ZSM-5

Zeolite Socony Mobil 5, 53

## Bibliography

- (1) Roiban, L.; Sorbier, L.; Pichon, C.; Bayle-Guillemaud, P.; Werckmann, J.; Drillon, M.; Ersen, O. Three-Dimensional Chemistry of Multiphase Nanomaterials by Energy-Filtered Transmission Electron Microscopy Tomography. *Microscopy and Microanalysis* **2012**, *18* (05), 1118–1128. <https://doi.org/10.1017/S143192761200116X>.
- (2) Roiban, L.; Ersen, O.; Hirlimann, C.; Drillon, M.; Chaumonnot, A.; Lemaitre, L.; Gay, A.-S.; Sorbier, L. Three-Dimensional Analytical Surface Quantification of Heterogeneous Silica-Alumina Catalyst Supports. *ChemCatChem* **2017**, *9* (8), 3503–3512. <https://doi.org/10.1002/cctc.201600543>.
- (3) Roiban, L.; Sorbier, L.; Hirlimann, C.; Ersen, O. 3 D Chemical Distribution of Titania-Alumina Catalyst Supports Prepared by the Swing-PH Method. *ChemCatChem* **2016**, *8* (9), 1651–1657. <https://doi.org/10.1002/cctc.201600033>.
- (4) Couzon, N.; Bois, L.; Fella, C.; Loestean, C.; Chassagneux, F.; Chiriach, R.; Toche, F.; Khrouz, L.; Brioude, A.; Ersen, O.; Roiban, L. Manganese Oxidation States Repartition in a Channel-like Mesoporous Zirconium Oxide. *J Porous Mater* **2020**, *27* (6), 1823–1835. <https://doi.org/10.1007/s10934-020-00962-5>.
- (5) Roiban, L.; Sorbier, L.; Hirlimann, C.; Ersen, O. Obtaining 3D Chemical Maps by Energy Filtered Transmission Electron Microscopy Tomography. *JoVE (Journal of Visualized Experiments)* **2018**, No. 136, e56671. <https://doi.org/10.3791/56671>.
- (6) Radon, J. Über Die Bestimmung von Funktionen Durch Ihre Integralwerte Langs Gewisser Mannigfaltigkeiten. *Journal of Mathematical Physics* **1917**, *69*, 262–277.
- (7) Radermacher, M. Radon Transform Techniques for Alignment and Three-Dimensional Reconstruction from Random Projections. *Scanning Microscopy* **1997**, *11*, 171–177.
- (8) Radermacher, M. Weighted Back-Projection Methods. In *Electron Tomography*; Frank, J., Ed.; Springer New York, 2007; pp 245–273. [https://doi.org/10.1007/978-0-387-69008-7\\_9](https://doi.org/10.1007/978-0-387-69008-7_9).
- (9) Bracewell, R. N. Strip Integration in Radio Astronomy. *Aust. J. Phys.* **1956**, *9* (2), 198–217. <https://doi.org/10.1071/ph560198>.
- (10) Rosier, D. J. D.; Klug, A. Reconstruction of Three Dimensional Structures from Electron Micrographs. *Nature* **1968**, *217* (5124), 130–134. <https://doi.org/10.1038/217130a0>.
- (11) Frank, J. *Electron Tomography - Methods for Three-Dimensional Visualization of Structures in the Cell*; Springer-Verlag New York, 2006.
- (12) Koster, A. J.; Ziese, U.; Verkleij, A. J.; Janssen, A. H.; de Jong, K. P. Three-Dimensional Transmission Electron Microscopy: A Novel Imaging and Characterization Technique with Nanometer Scale Resolution for Materials Science. *The Journal of Physical Chemistry B* **2000**, *104* (40), 9368–9370. <https://doi.org/10.1021/jp0015628>.
- (13) Midgley, P. A.; Dunin-Borkowski, R. E. Electron Tomography and Holography in Materials Science. *Nature Materials* **2009**, *8* (4), 271–280. <https://doi.org/10.1038/nmat2406>.
- (14) Midgley, P. A.; Saghi, Z. Electron Tomography in Solid State and Materials Science – An Introduction. *Current Opinion in Solid State and Materials Science* **2013**, *17* (3), 89–92. <https://doi.org/10.1016/j.cossms.2013.07.006>.
- (15) Zečević, J.; de Jong, K. P.; de Jongh, P. E. Progress in Electron Tomography to Assess the 3D Nanostructure of Catalysts. *Current Opinion in Solid State and Materials Science* **2013**, *17* (3), 115–125. <https://doi.org/10.1016/j.cossms.2013.04.002>.

- (16) Hungría, A. B.; Calvino, J. J.; Hernández-Garrido, J. C. HAADF-STEM Electron Tomography in Catalysis Research. *Top Catal* **2019**, *62* (12), 808–821. <https://doi.org/10.1007/s11244-019-01200-2>.
- (17) Lepinay, K.; Lorut, F.; Pantel, R.; Epicier, T. Chemical 3D Tomography of 28nm High K Metal Gate Transistor: STEM XEDS Experimental Method and Results. *Micron* **2013**, *47*, 43–49. <https://doi.org/10.1016/j.micron.2013.01.004>.
- (18) Bals, S.; Casavola, M.; van Huis, M. A.; Van Aert, S.; Batenburg, K. J.; Van Tendeloo, G.; Vanmaekelbergh, D. Three-Dimensional Atomic Imaging of Colloidal Core–Shell Nanocrystals. *Nano Lett.* **2011**, *11* (8), 3420–3424. <https://doi.org/10.1021/nl201826e>.
- (19) Miao, J.; Ercius, P.; Billinge, S. J. L. Atomic Electron Tomography: 3D Structures without Crystals. *Science* **2016**, *353* (6306), aaf2157–aaf2157. <https://doi.org/10.1126/science.aaf2157>.
- (20) Dyck, V. D.; Aert, S.; Croitoru, M. Atomic Resolution Electron Tomography: A Dream? *Int. J. Mat. Res.* *97* (7), 872–879.
- (21) Saghi, Z.; Divitini, G.; Winter, B.; Leary, R.; Spiecker, E.; Ducati, C.; Midgley, P. A. Compressed Sensing Electron Tomography of Needle-Shaped Biological Specimens – Potential for Improved Reconstruction Fidelity with Reduced Dose. *Ultramicroscopy* **2016**, *160*, 230–238. <https://doi.org/10.1016/j.ultramic.2015.10.021>.
- (22) Padgett, E.; Hovden, R.; DaSilva, J. C.; Levin, B. D. A.; Grazul, J. L.; Hanrath, T.; Muller, D. A. A Simple Preparation Method for Full-Range Electron Tomography of Nanoparticles and Fine Powders. *Microscopy and Microanalysis* **2017**, *23* (6), 1150–1158. <https://doi.org/10.1017/S1431927617012764>.
- (23) Georgescu, D.; Roiban, L.; Ersen, O.; Ihiwakrim, D.; Baia, L.; Simon, S. Insights on Ag Doped Porous TiO<sub>2</sub> Nanostructures: A Comprehensive Study of Their Structural and Morphological Characteristics. *RSC Advances* **2012**, *2* (12), 5358. <https://doi.org/10.1039/c2ra20568h>.
- (24) Shakeri, M.; Roiban, L.; Yazerski, V.; Prieto, G.; Klein Gebbink, R. J. M.; de Jongh, P. E.; de Jong, K. P. Engineering and Sizing Nanoreactors To Confine Metal Complexes for Enhanced Catalytic Performance. *ACS Catalysis* **2014**, *4* (10), 3791–3796. <https://doi.org/10.1021/cs500777q>.
- (25) Carencu, S.; Moldovan, S.; Roiban, L.; Florea, I.; Portehault, D.; Vallé, K.; Belleville, P.; Boissière, C.; Rozes, L.; Mézailles, N.; Drillon, M.; Sanchez, C.; Ersen, O. The Core Contribution of Transmission Electron Microscopy to Functional Nanomaterials Engineering. *Nanoscale* **2016**, *8* (3), 1260–1279. <https://doi.org/10.1039/C5NR05460E>.
- (26) Kremer, J. R.; Mastrorade, D. N.; McIntosh, J. R. Computer Visualization of Three-Dimensional Image Data Using IMOD. *Journal of structural biology* **1996**, *116* (1), 71–76.
- (27) Messaoudi, C.; Boudier, T.; Sorzano, C.; Marco, S. TomoJ: Tomography Software for Three-Dimensional Reconstruction in Transmission Electron Microscopy. *BMC Bioinformatics* **2007**, *8* (1), 288. <https://doi.org/10.1186/1471-2105-8-288>.
- (28) ImageJ <https://imagej.nih.gov/ij/> (accessed 2017 -07 -14).
- (29) Fedorov, A.; Beichel, R.; Kalpathy-Cramer, J.; Finet, J.; Fillion-Robin, J.-C.; Pujol, S.; Bauer, C.; Jennings, D.; Fennessy, F.; Sonka, M.; Buatti, J.; Aylward, S.; Miller, J. V.; Pieper, S.; Kikinis, R. 3D Slicer as an Image Computing Platform for the Quantitative Imaging Network. *Magnetic Resonance Imaging* **2012**, *30* (9), 1323–1341. <https://doi.org/10.1016/j.mri.2012.05.001>.
- (30) Thomas, D.; Puyoo, E.; Le Berre, M.; Militaru, L.; Koneti, S.; Malchère, A.; Epicier, T.; Roiban, L.; Albertini, D.; Sabac, A.; Calmon, F. Investigation of the In-Plane and out-of-Plane Electrical Properties of Metallic Nanoparticles in Dielectric Matrix Thin

- Films Elaborated by Atomic Layer Deposition. *Nanotechnology* **2017**, 28 (45), 455602. <https://doi.org/10.1088/1361-6528/aa8b5e>.
- (31) Puyoo, E.; Malhaire, C.; Thomas, D.; Rafaël, R.; R'Mili, M.; Malchère, A.; Roiban, L.; Koneti, S.; Bugnet, M.; Sabac, A.; Le Berre, M. Metallic Nanoparticle-Based Strain Sensors Elaborated by Atomic Layer Deposition. *Appl. Phys. Lett.* **2017**, 110 (12), 123103. <https://doi.org/10.1063/1.4978778>.
- (32) Couzon, N.; Maillard, M.; Bois, L.; Chassagneux, F.; Brioude, A. Electrochemical Observation of the Plasmonic Effect in Photochromic Ag Nanoparticle Filled Mesoporous TiO<sub>2</sub> Films. *J. Phys. Chem. C* **2017**, 121 (40), 22147–22155. <https://doi.org/10.1021/acs.jpcc.7b07155>.
- (33) Couzon, N.; Maillard, M.; Chassagneux, F.; Brioude, A.; Bois, L. Photoelectrochemical Behavior of Silver Nanoparticles inside Mesoporous Titania: Plasmon-Induced Charge Separation Effect. *Langmuir* **2019**, 35 (7), 2517–2526. <https://doi.org/10.1021/acs.langmuir.8b03617>.
- (34) Couzon, N.; Roiban, L.; Chassagneux, F.; Bois, L.; Brioude, A.; Maillard, M. Electroactive Area from Porous Oxide Films Loaded with Silver Nanoparticles: Electrochemical and Electron Tomography Observations. *ACS Applied Materials & Interfaces* **2019**, 11 (40), 37270–37278. <https://doi.org/10.1021/acsami.9b11581>.
- (35) Koneti, S.; Roiban, L.; Dalmas, F.; Langlois, C.; Gay, A.-S.; Cabiach, A.; Grenier, T.; Banjak, H.; Maxim, V.; Epicier, T. Fast Electron Tomography: Applications to Beam Sensitive Samples and in Situ TEM or Operando Environmental TEM Studies. *Materials Characterization* **2019**, 151, 480–495. <https://doi.org/10.1016/j.matchar.2019.02.009>.
- (36) Li, S.; Tuel, A.; Laprune, D.; Meunier, F.; Farrusseng, D. Transition-Metal Nanoparticles in Hollow Zeolite Single Crystals as Bifunctional and Size-Selective Hydrogenation Catalysts. *Chemistry of Materials* **2015**, 27 (1), 276–282. <https://doi.org/10.1021/cm503921f>.
- (37) Farrusseng, D.; Tuel, A. Perspectives on Zeolite-Encapsulated Metal Nanoparticles and Their Applications in Catalysis. *New J. Chem.* **2016**, 40 (5), 3933–3949. <https://doi.org/10.1039/C5NJ02608C>.
- (38) Vanrompay, H.; Skorikov, A.; Bladt, E.; Béché, A.; Freitag, B.; Verbeeck, J.; Bals, S. Fast versus Conventional HAADF-STEM Tomography of Nanoparticles: Advantages and Challenges. *Ultramicroscopy* **2021**, 221, 113191. <https://doi.org/10.1016/j.ultramic.2020.113191>.
- (39) Gordon, R.; Bender, R.; Herman, G. T. Algebraic Reconstruction Techniques (ART) for Three-Dimensional Electron Microscopy and X-Ray Photography. *Journal of Theoretical Biology* **1970**, 29 (3), 471–481. [https://doi.org/10.1016/0022-5193\(70\)90109-8](https://doi.org/10.1016/0022-5193(70)90109-8).
- (40) Petterson, E. F.; Goddard, T. D.; Huang, C. C.; Couch, G. S.; Greenblatt, D. M.; Meng, E. C.; Ferrin, T. E. UCSF Chimera—A Visualization System for Exploratory Research and Analysis. *J. Comput. Chem.* **2004**, 25 (13), 1605–1612. <https://doi.org/10.1002/jcc.20084>.
- (41) Saggi, Z.; Holland, D. J.; Leary, R.; Falqui, A.; Bertoni, G.; Sederman, A. J.; Gladden, L. F.; Midgley, P. A. Three-Dimensional Morphology of Iron Oxide Nanoparticles with Reactive Concave Surfaces. A Compressed Sensing-Electron Tomography (CS-ET) Approach. *Nano Lett.* **2011**, 11 (11), 4666–4673. <https://doi.org/10.1021/nl202253a>.
- (42) Sidky, E. Y.; Pan, X. Image Reconstruction in Circular Cone-Beam Computed Tomography by Constrained, Total-Variation Minimization. *Phys. Med. Biol.* **2008**, 53 (17), 4777. <https://doi.org/10.1088/0031-9155/53/17/021>.
- (43) Goris, B.; Roelandts, T.; Batenburg, K. J.; Heidari Mezerji, H.; Bals, S. Advanced Reconstruction Algorithms for Electron Tomography: From Comparison to

- Combination. *Ultramicroscopy* **2013**, *127*, 40–47. <https://doi.org/10.1016/j.ultramic.2012.07.003>.
- (44) Batenburg, K. J.; Sijbers, J. DART: A Practical Reconstruction Algorithm for Discrete Tomography. *IEEE Transactions on Image Processing* **2011**, *20* (9), 2542–2553. <https://doi.org/10.1109/TIP.2011.2131661>.
- (45) Gilbert, P. Iterative Methods for the Three-Dimensional Reconstruction of an Object from Projections. *Journal of theoretical biology* **1972**, *36* (1), 105–117.
- (46) Banjak, H.; Grenier, T.; Epicier, T.; Koneti, S.; Roiban, L.; Gay, A.-S.; Magnin, I.; Peyrin, F.; Maxim, V. Evaluation of Noise and Blur Effects with SIRT-FISTA-TV Reconstruction Algorithm: Application to Fast Environmental Transmission Electron Tomography. *Ultramicroscopy* **2018**, *189*, 109–123. <https://doi.org/10.1016/j.ultramic.2018.03.022>.
- (47) Banjak, H.; Costin, M.; Vienne, C.; Guillaumet, R.; Kaftandjian, V. Iterative CT Reconstruction on Limited Angle Trajectories Applied to Robotic Inspection. *AIP Conference Proceedings* **2017**, *1806* (1), 020009. <https://doi.org/10.1063/1.4974550>.
- (48) Roiban, L.; Foray, G.; Rong, Q.; Perret, A.; Ihiwakrim, D.; Masenelli-Varlot, K.; Maire, E.; Yrieix, B. Advanced Three Dimensional Characterization of Silica-Based Ultraporous Materials. *RSC Adv.* **2016**, *6* (13), 10625–10632. <https://doi.org/10.1039/C5RA26014K>.
- (49) Chal, B.; Foray, G.; Yrieix, B.; Masenelli-Varlot, K.; Roiban, L.; Chenal, J.-M. Durability of Silica Aerogels Dedicated to Superinsulation Measured under Hygrothermal Conditions. *Microporous and Mesoporous Materials* **2018**, *272*, 61–69. <https://doi.org/10.1016/j.micromeso.2018.05.047>.
- (50) Chal, B.; Yrieix, B.; Roiban, L.; Masenelli-Varlot, K.; Chenal, J.-M.; Foray, G. Nanostructured Silica Used in Super-Insulation Materials (SIM), Hygrothermal Ageing Followed by Sorption Characterizations. *Energy and Buildings* **2019**, *183*, 626–638. <https://doi.org/10.1016/j.enbuild.2018.11.044>.
- (51) Chal, B.; Foray, G.; Roiban, L.; Masenelli-Varlot, K.; Chenal, J.-M.; Yrieix, B. Vieillissement hygrothermique d'un aérogel de silice, évolution des propriétés mécaniques en lien avec les changements de structure et de chimie. **2018**, *36* (1), 4.
- (52) Benane, B.; Baeza, G. P.; Chal, B.; Roiban, L.; Meille, S.; Olagnon, C.; Yrieix, B.; Foray, G. Multiscale Structure of Super Insulation Nano-Fumed Silicas Studied by SAXS, Tomography and Porosimetry. *Acta Materialia* **2019**, *168*, 401–410. <https://doi.org/10.1016/j.actamat.2019.02.024>.
- (53) Das, A.; Costa, F. R.; Wagenknecht, U.; Heinrich, G. Nanocomposites Based on Chloroprene Rubber: Effect of Chemical Nature and Organic Modification of Nanoclay on the Vulcanizate Properties. *European Polymer Journal* **2008**, *44* (11), 3456–3465. <https://doi.org/10.1016/j.eurpolymj.2008.08.025>.
- (54) Jinschek, J. R. Advances in the Environmental Transmission Electron Microscope (ETEM) for Nanoscale in Situ Studies of Gas–Solid Interactions. *Chemical Communications* **2014**, *50* (21), 2696. <https://doi.org/10.1039/c3cc49092k>.
- (55) Fino, D.; Bensaid, S.; Piumetti, M.; Russo, N. A Review on the Catalytic Combustion of Soot in Diesel Particulate Filters for Automotive Applications: From Powder Catalysts to Structured Reactors. *Applied Catalysis A: General* **2016**, *509*, 75–96. <https://doi.org/10.1016/j.apcata.2015.10.016>.
- (56) Stanmore, B. R.; Brilhac, J. F.; Gilot, P. The Oxidation of Soot: A Review of Experiments, Mechanisms and Models. *Carbon* **2001**, *39* (15), 2247–2268. [https://doi.org/10.1016/S0008-6223\(01\)00109-9](https://doi.org/10.1016/S0008-6223(01)00109-9).
- (57) Roiban, L.; Li, S.; Aouine, M.; Tuel, A.; Farrusseng, D.; Epicier, T. Fast ‘Operando’ Electron Nanotomography. *Journal of Microscopy* **2018**, *269* (2), 117–126. <https://doi.org/10.1111/jmi.12557>.

- (58) Melinte, G.; Florea, I.; Moldovan, S.; Janowska, I.; Baaziz, W.; Arenal, R.; Wisnet, A.; Scheu, C.; Begin-Colin, S.; Begin, D.; Pham-Huu, C.; Ersen, O. A 3D Insight on the Catalytic Nanostructuring of Few-Layer Graphene. *Nature Communications* **2014**, *5*, 4109.
- (59) Munnik, P.; de Jongh, P. E.; de Jong, K. P. Recent Developments in the Synthesis of Supported Catalysts. *Chemical Reviews* **2015**, *115* (14), 6687–6718. <https://doi.org/10.1021/cr500486u>.
- (60) Neagu, D.; Tsekouras, G.; Miller, D. N.; Ménard, H.; Irvine, J. T. S. *In Situ* Growth of Nanoparticles through Control of Non-Stoichiometry. *Nature Chemistry* **2013**, *5* (11), 916–923. <https://doi.org/10.1038/nchem.1773>.
- (61) Neagu, D.; Oh, T.-S.; Miller, D. N.; Ménard, H.; Bukhari, S. M.; Gamble, S. R.; Gorte, R. J.; Vohs, J. M.; Irvine, J. T. S. Nano-Socketed Nickel Particles with Enhanced Coking Resistance Grown *in Situ* by Redox Exsolution. *Nature Communications* **2015**, *6*, 8120. <https://doi.org/10.1038/ncomms9120>.
- (62) Neagu, D.; Kyriakou, V.; Roiban, I.-L.; Aouine, M.; Tang, C.; Caravaca, A.; Kousi, K.; Schreur-Piet, I.; Metcalfe, I. S.; Vernoux, P.; van de Sanden, M. C. M.; Tsampas, M. N. In Situ Observation of Nanoparticle Exsolution from Perovskite Oxides: From Atomic Scale Mechanistic Insight to Nanostructure Tailoring. *ACS Nano* **2019**, *13* (11), 12996–13005. <https://doi.org/10.1021/acsnano.9b05652>.
- (63) Roiban, L.; Sorbier, L.; Pichon, C.; Pham-Huu, C.; Drillon, M.; Ersen, O. 3D-TEM Investigation of the Nanostructure of a  $\delta$ -Al<sub>2</sub>O<sub>3</sub> Catalyst Support Decorated with Pd Nanoparticles. *Nanoscale* **2012**, *4* (3), 946–954. <https://doi.org/10.1039/C2NR11235C>.
- (64) Epicier, T.; Koneti, S.; Avenier, P.; Cabiac, A.; Gay, A.-S.; Roiban, L. 2D & 3D *In Situ* Study of the Calcination of Pd Nanocatalysts Supported on Delta-Alumina in an Environmental Transmission Electron Microscope. *Catalysis Today* **2019**, *334*, 68–78. <https://doi.org/10.1016/j.cattod.2019.01.061>.
- (65) Crozier, P. A.; Sharma, R.; Datye, A. K. Oxidation and Reduction of Small Palladium Particles on Silica. *Microscopy and Microanalysis* **1998**, *4* (3), 278–285. <https://doi.org/10.1017/S143192769898028X>.
- (66) Monpezat, A.; Couchaux, G.; Thomas, V.; Artheix, A.; Deliere, L.; Gréau, C.; Topin, S.; Coasne, B.; Roiban, L.; Cardenas, L.; Farrusseng, D. Effect of Chlorine-Containing VOCs on Silver Migration and Sintering in ZSM-5 Used in a TSA Process. *Catalysts* **2019**, *9* (8), 686. <https://doi.org/10.3390/catal9080686>.
- (67) Monpezat, A.; Topin, S.; Thomas, V.; Pagis, C.; Aouine, M.; Burel, L.; Cardenas, L.; Tuel, A.; Malchère, A.; Epicier, T.; Farrusseng, D.; Roiban, L. Migration and Growth of Silver Nanoparticles in Zeolite Socony Mobil 5 (ZSM-5) Observed by Environmental Electron Microscopy: Implications for Heterogeneous Catalysis. *ACS Applied Nano Materials* **2019**, *2* (10), 6452–6461. <https://doi.org/10.1021/acsanm.9b01407>.
- (68) Monpezat, A.; Topin, S.; Deliere, L.; Farrusseng, D.; Coasne, B. Evaluation Methods of Adsorbents for Air Purification and Gas Separation at Low Concentration: Case Studies on Xenon and Krypton. *Ind. Eng. Chem. Res.* **2019**, *58* (11), 4560–4571. <https://doi.org/10.1021/acs.iecr.8b04866>.
- (69) Bogner, A.; Thollet, G.; Basset, D.; Jouneau, P.-H.; Gauthier, C. Wet STEM: A New Development in Environmental SEM for Imaging Nano-Objects Included in a Liquid Phase. *Ultramicroscopy* **2005**, *104* (3–4), 290–301. <https://doi.org/10.1016/j.ultramic.2005.05.005>.
- (70) Bogner, A.; Jouneau, P.-H.; Thollet, G.; Basset, D.; Gauthier, C. A History of Scanning Electron Microscopy Developments: Towards “Wet-STEM” Imaging. *Micron* **2007**, *38* (4), 390–401. <https://doi.org/10.1016/j.micron.2006.06.008>.

- (71) Masenelli-Varlot, K.; Malchère, A.; Ferreira, J.; Heidari Mezerji, H.; Bals, S.; Messaoudi, C.; Marco Garrido, S. Wet-STEM Tomography: Principles, Potentialities and Limitations. *Microscopy and Microanalysis* **2014**, *20* (02), 366–375. <https://doi.org/10.1017/S1431927614000105>.
- (72) Masenelli-Varlot, K.; Gauthier, C.; Chazeau, L.; Dalmas, F.; Epicier, T.; Cavaillé, J. y. Advanced Microscopy Techniques for a Better Understanding of the Polymer/Nanotube Composite Properties. In *Polymer Nanotube Nanocomposites*; Mittal, V., Ed.; John Wiley & Sons, Inc., 2014; pp 365–404. <https://doi.org/10.1002/9781118945964.ch10>.
- (73) Jomaa, M. H.; Roiban, L.; Dhungana, D. S.; Xiao, J.; Cavaillé, J. Y.; Seveyrat, L.; Lebrun, L.; Diguët, G.; Masenelli-Varlot, K. Quantitative Analysis of Grafted CNT Dispersion and of Their Stiffening of Polyurethane (PU). *Composites Science and Technology* **2019**, *171*, 103–110. <https://doi.org/10.1016/j.compscitech.2018.12.012>.
- (74) *Liquid Cell Electron Microscopy*; Ross, F. M., Ed.; Advances in Microscopy and Microanalysis; Cambridge University Press: Cambridge, 2016. <https://doi.org/10.1017/9781316337455>.
- (75) de Jonge, N.; Houben, L.; Dunin-Borkowski, R. E.; Ross, F. M. Resolution and Aberration Correction in Liquid Cell Transmission Electron Microscopy. *Nature Reviews Materials* **2019**, *4* (1), 61–78. <https://doi.org/10.1038/s41578-018-0071-2>.
- (76) Park, J.; Elmlund, H.; Ercius, P.; Yuk, J. M.; Limmer, D. T.; Chen, Q.; Kim, K.; Han, S. H.; Weitz, D. A.; Zettl, A.; Alivisatos, T. P. 3D Structure of Individual Nanocrystals in Solution by Electron Microscopy. *Science* **2015**, *349* (6245), 290–295. <https://doi.org/10.1126/science.aab1343>.
- (77) Dearnaley, W. J.; Schleupner, B.; Varano, A. C.; Alden, N. A.; Gonzalez, F.; Casasanta, M. A.; Scharf, B. E.; Dukes, M. J.; Kelly, D. F. Liquid-Cell Electron Tomography of Biological Systems. *Nano Letters* **2019**, *19* (10), 6734–6741. <https://doi.org/10.1021/acs.nanolett.9b01309>.
- (78) Dearnaley, W. J.; Schleupner, B.; Alden, N. A.; Gonzalez, F.; Scharf, B.; Dukes, M. J.; Kelly, D. F. Liquid Cell Electron Tomography for Biomedical Applications. *Microscopy and Microanalysis* **2018**, *24* (S1), 268–269. <https://doi.org/10.1017/S1431927618001836>.
- (79) Peckys, D. B.; Baudoin, J.-P.; Eder, M.; Werner, U.; de Jonge, N. Epidermal Growth Factor Receptor Subunit Locations Determined in Hydrated Cells with Environmental Scanning Electron Microscopy. *Scientific Reports* **2013**, *3* (1), 2626. <https://doi.org/10.1038/srep02626>.
- (80) Xiao, J.; Roiban, L.; Foray, G.; Masenelli-Varlot, K. Electron Tomography on Latex Particles Suspended in Water Using Environmental Scanning Electron Microscopy. *Micron* **2019**, *117*, 60–67. <https://doi.org/10.1016/j.micron.2018.11.007>.
- (81) Xiao, J.; Foray, G.; Masenelli-Varlot, K. Analysis of Liquid Suspensions Using Scanning Electron Microscopy in Transmission: Estimation of the Water Film Thickness Using Monte–Carlo Simulations. *Journal of Microscopy* **2018**, *269* (2), 151–160. <https://doi.org/10.1111/jmi.12619>.
- (82) Perret, A.; Foray, G.; Masenelli-Varlot, K.; Maire, E.; Yrieix, B. Study of the Surfactant Role in Latex–Aerogel Systems by Scanning Transmission Electron Microscopy on Aqueous Suspensions. *Journal of Microscopy* **2018**, *269* (1), 3–13. <https://doi.org/10.1111/jmi.12603>.
- (83) Möbus, G.; Inkson, B. J. Nanoscale Tomography in Materials Science. *Materials Today* **2007**, *10* (12), 18–25. [https://doi.org/10.1016/S1369-7021\(07\)70304-8](https://doi.org/10.1016/S1369-7021(07)70304-8).
- (84) Möbus, G.; Doole, R. C.; Inkson, B. J. Spectroscopic Electron Tomography. *Ultramicroscopy* **2003**, *96* (3–4), 433–451. [https://doi.org/10.1016/S0304-3991\(03\)00106-2](https://doi.org/10.1016/S0304-3991(03)00106-2).

- (85) Minor, L. B.; Solomon, D.; Zinreich, J. S.; Zee, D. S. Sound- and/or Pressure-Induced Vertigo Due to Bone Dehiscence of the Superior Semicircular Canal. *Arch Otolaryngol Head Neck Surg* **1998**, *124* (3), 249–258. <https://doi.org/10.1001/archotol.124.3.249>.
- (86) Iversen, M. M.; Zhu, H.; Zhou, W.; Della Santina, C. C.; Carey, J. P.; Rabbitt, R. D. Sound Abnormally Stimulates the Vestibular System in Canal Dehiscence Syndrome by Generating Pathological Fluid-Mechanical Waves. *Scientific Reports* **2018**, *8* (1). <https://doi.org/10.1038/s41598-018-28592-7>.
- (87) Rabbitt, R. D.; Breneman, K. D.; King, C.; Yamauchi, A. M.; Boyle, R.; Highstein, S. M. Dynamic Displacement of Normal and Detached Semicircular Canal Cupula. *Journal of the Association for Research in Otolaryngology* **2009**, *10* (4), 497–509. <https://doi.org/10.1007/s10162-009-0174-y>.
- (88) Rabbitt, R. D.; Boyle, R.; Highstein, S. M. Influence of Surgical Plugging on Horizontal Semicircular Canal Mechanics and Afferent Response Dynamics. *Journal of Neurophysiology* **1999**, *82* (2), 1033–1053. <https://doi.org/10.1152/jn.1999.82.2.1033>.
- (89) Ho, M.-L.; Moonis, G.; Halpin, C. F.; Curtin, H. D. Spectrum of Third Window Abnormalities: Semicircular Canal Dehiscence and Beyond. *American Journal of Neuroradiology* **2017**, *38* (1), 2–9. <https://doi.org/10.3174/ajnr.A4922>.
- (90) Ionescu, E. C.; Al Tamami, N.; Neagu, A.; Ltaief-Boudrigoua, A.; Gallego, S.; Hermann, R.; Truy, E.; Thai-Van, H. Superior Semicircular Canal Ampullae Dehiscence As Part of the Spectrum of the Third Window Abnormalities: A Case Study. *Frontiers in Neurology* **2017**, *8*. <https://doi.org/10.3389/fneur.2017.00683>.
- (91) Ionescu, E. C.; Coudert, A.; Reynard, P.; Truy, E.; Thai-Van, H.; Ltaief-Boudrigoua, A.; Turjman, F. Stenting the Superior Petrosal Sinus in a Patient With Symptomatic Superior Semicircular Canal Dehiscence. *Front. Neurol.* **2018**, *9*. <https://doi.org/10.3389/fneur.2018.00689>.
- (92) Selva, P. Modélisation Du Système Vestibulaire et Modèles Non-Linéaires de Perception de l'orientation Spatiale. These de doctorat, Toulouse, ISAE, 2009.
- (93) Marturi, N.; Dembélé, S.; Piat, N. Scanning Electron Microscope Image Signal-to-noise Ratio Monitoring for Micro-nanomanipulation. *Scanning* **2014**, *36* (419–429). <https://doi.org/10.1002/sca.21137>.
- (94) Kudryavtsev, A. 3D Reconstruction in Scanning Electron Microscope : From Image Acquisition to Dense Point Cloud. These de doctorat, Bourgogne Franche-Comté, 2017.
- (95) Beb Caal, M. Reconstruction 3D Complète de Surfaces Avec Un Microscope Électronique à Balayage Pour Applications Métrologiques et Pédagogiques. These en préparation, Bourgogne Franche-Comté, 2020.
- (96) Koneti, S.; Borges, J.; Roiban, L.; Rodrigues, M. S.; Martin, N.; Epicier, T.; Vaz, F.; Steyer, P. Electron Tomography of Plasmonic Au Nanoparticles Dispersed in a TiO<sub>2</sub> Dielectric Matrix. *ACS Applied Materials & Interfaces* **2018**, *10* (49), 42882–42890. <https://doi.org/10.1021/acsami.8b16436>.
- (97) Ramade, J.; Cottancin, E.; Lebeault, M.-A.; Langlois, C.; Piccolo, L.; Broyer, M.; Hillenkamp, M.; Lermé, J.; Calvo, F.; Pellarin, M. Environmental Plasmonic Spectroscopy of Silver–Iron Nanoparticles: Chemical Ordering under Oxidizing and Reducing Conditions. *J. Phys. Chem. C* **2019**, *123* (25), 15693–15706. <https://doi.org/10.1021/acs.jpcc.9b02422>.
- (98) Ramade, J.; Langlois, C.; Pellarin, M.; Piccolo, L.; Lebeault, M.-A.; Epicier, T.; Aouine, M.; Cottancin, E. Tracking the Restructuring of Oxidized Silver–Indium Nanoparticles under a Reducing Atmosphere by Environmental HRTEM. *Nanoscale* **2017**, *9* (36), 13563–13574. <https://doi.org/10.1039/C7NR02986A>.
- (99) Zewail, A. H. Four-Dimensional Electron Microscopy. *Science* **2010**, *328* (5975), 187–193. <https://doi.org/10.1126/science.1166135>.



- (100) Zewail, A. H.; Thomas, J. M. *4D Electron Microscopy: Imaging in Space and Time*; Imperial College Press: London, 2010.
- (101) Hetherington, C. Aberration Correction for TEM. *Materials Today* **2004**, 7 (12), 50–55. [https://doi.org/10.1016/S1369-7021\(04\)00571-1](https://doi.org/10.1016/S1369-7021(04)00571-1).
- (102) Babcock, H. W. THE POSSIBILITY OF COMPENSATING ASTRONOMICAL SEEING. *PASP* **1953**, 65 (386), 229. <https://doi.org/10.1086/126606>.
- (103) Merkle, F.; Rousset, G.; Kern, P. Y.; Gaffard, J.-P. First Diffraction-Limited Astronomical Images with Adaptive Optics. In *Advanced Technology Optical Telescopes IV*; International Society for Optics and Photonics, 1990; Vol. 1236, pp 193–202. <https://doi.org/10.1117/12.19189>.
- (104) Wizinowich, P. Adaptive Optics in Astronomy. *Contemporary Physics* **2015**, 56 (4), 432–450. <https://doi.org/10.1080/00107514.2015.1041765>.